A STUDY OF THE TRANSPORT PROPERTIES OF ELECTROLYTES FOR LI-ION BATTERIES

by

Eric Logan

Submitted in partial fulfilment of the requirements
for the degree of Master of Science

at

Dalhousie University
Halifax, Nova Scotia
June 2018

TABLE OF CONTENTS

LIST OF TABLES

LIST OF FIGURES

ABSTRACT

Measuring the transport properties of electrolyte solutions can be an effective way to screen for candidate electrolytes for use in a given Li-ion battery application. In this thesis, ionic conductivity and viscosity are measured for a wide range of electrolytes falling under two main classes: carbonate-based electrolytes with added low-viscosity co-solvents to increase ionic conductivity for high charge rate applications, and carbonate electrolytes that do not contain ethylene carbonate (EC), which has been found to negatively affect cell lifetime at high voltage. Of the different co-solvents studied, the ester, methyl acetate (MA) gave one of the largest increases in conductivity in these electrolytes. The impact of MA on electrolyte conductivity and viscosity was studied as a function of salt concentration, solvent composition, and temperature. Removing EC from the electrolyte caused a decrease in the solution viscosity, but also a decrease in the maximum conductivity. This phenomenon was investigated further using Walden-type analyses, concluding that significant ion association occurs in solutions with low EC content. Charge-discharge data for full Li-ion cells confirm that electrolytes containing MA improve the charge rate capability of cells, and removing EC improves long-term cycling at elevated voltage. The data collected in this thesis was compared to a theoretical model of electrolyte properties, the Advanced Electrolyte Model (AEM), which was able to correctly predict the viscosity and conductivity of the different electrolytes studied in this thesis in its current form.

LIST OF ABBREVIATIONS USED

AEM	Advanced Electrolyte Model
AG	artificial graphite
AN	acetonitrile
BB	butyl butyrate
BP	boiling point
CCCV	constant current, constant voltage
CIP	contact ion pair
DEC	diethyl carbonate
DMC	dimethyl carbonate
DME	dimethoxyethane
DSC	differential scanning calorimetry
DTA	differential thermal analysis
DTD	1,3,2-dioxathiolane-2,2-dioxide
EA	ethyl acetate
EB	ethyl butyrate
EC	ethylene carbonate
EDLC	electric double layer capacitor
EF	ethyl formate
EMC	ethyl methyl carbonate
EP	ethyl propionate
EV	electric vehicle
FEC	fluoroethylene carbonate
Glyme	dimethoxyethane
HS	hard sphere
iBA	isobutyl acetate
iBF	isobutyl formate
iBN	isobutyronitrile
IP	ion pair
IL	ionic liquid
LCO	$LiCoO_2$
LEDC	Li ethylene dicarbonate
LFP	$LiFePO_4$
LiBETI	Li bis(perfluoroethanesulfonyl)imide
LiDFOB	Li difluoro(oxalato)borate
LiFSI	Li bis(fluorosulfonyl) imide
LiTFSI	Li bis(trifluoromethylsulfone)imide
LMO	$LiMn_2O_4$
LTO	$Li_{4/3}Ti_{5/3}O_4$
MA	methyl acetate
MB	methyl butyrate
MF	methyl formate
MP	methyl proprionate/melting point
MSA	mean spherical approximation
NCA	$Li[Ni_{1-x-y}Co_xAl_y]O_2$

NMC	$Li[Ni_{1-x-y}Mn_xCo_y]O_2$
NPNRAMSA	non-primitive, non-restricted associative form of the mean spherical approximation
PB	propyl butyrate
PC	propylene carbonate
PE	polyethylene
PF	propyl formate
PN	propionitrile
PP	polypropylene
PVDF	polyvinylidene fluoride
SEI	solid electrolyte interphase
SI	single ion
SSIP	solvent separated ion pair
SShIP	solvent-shared ion pair
TI	triple ion
TMP	trimethyl phosphate
UHPC	ultra-high precision charger
VC	vinylene carbonate
κ	ionic conductivity
μ	ion mobility
n	number density
z	ion charge number
e	elementary charge
v	drift velocity
E	electric field strength
F_d	drag force
η	dynamic viscosity
r	Stokes radius / radial distance
r_+	cation Stokes radius
r_-	anion Stokes radius
r_c	critical distance (Bjerrum treatment)
D	diffusion coefficient
k_B	Boltzmann's constant
T	temperature
F	Faraday's constant
c	molar concentration of ions
ϕ	fluidity
$c_\pm$	molar concentration of positive or negative ions
c_0	molar concentration of salt
Λ	molar conductivity
R	combined Stokes radii
f	salt dissociation factor, various contributions to AEM transport properties
t	transference number, time
Λ^0	limiting molar conductivity
A	free parameter in Kohlrausch relation

η^0	dynamic viscosity of pure solvent (infinite dilution)
ψ	electric potential
ρ	charge density, mass density
ϵ	dielectric constant
a	distance of closest approach
C^+	cation (arbitrary)
A^-	anion (arbitrary)
K_A	association constant
α	fraction of free ions in solution, calibration factor for viscosity
η^0_{mix}	viscosity of mixed solvent at infinite dilution
η^0_{ps}	pseudo-solvent viscosity (infinite dilution)
τ	solvent residence time
λ	molar conductivity of a single ion species
σ	ion diameter
K	constant, equal to $Fe/3\pi$
y	Solvent mole fraction

ACKNOWLEDGEMENTS

I would first like to thank Jeff Dahn for all the help and support he has given me over the last two years. His level of dedication is something to aspire to and his encouragement made this work much more enjoyable.

I would also like to thank Luc Beaulieu for initially getting me involved in this project and for designing/building the conductivity and viscosity setups that are used in this thesis. It was a pleasure to be able to work with Luc while he was visiting Dalhousie.

Thanks to Erin Tonita for helping to endure long days of conductivity measurements and countless hours in the glovebox.

Thanks to Laura for her constant support and for trusting in my abilities more than I do.

Thanks to everyone in the Dahn lab. Even though I haven't had the chance to work with everyone directly, the level of positivity and willingness to lend a helping hand in this lab is incredible. In particular, I'd like to thank Lin, Jim, and Michael for running some of the experiments found in this thesis.

CHAPTER 1   INTRODUCTION

1.1   MOTIVATION AND SCOPE

First commercialized in 1991 by Sony[1], lithium-ion batteries now dominate the battery market for consumer electronics (cell phones, laptops, cordless power tools, etc.)[2], and, increasingly, larger applications such as electric vehicles (EVs) and grid level energy storage (e.g. Tesla Powerwall). This is due to the high energy density, relatively high power density, and relatively low cost of Li-ion technology (per kWh) compared to other competing energy storage systems. To further the adoption of Li-ion batteries to the above mentioned large scale energy storage applications, improvements must be made to existing technology. The continual goal of battery researchers is the improvement of energy density as well as power density, without increasing the cost of the technology, compromising safety, or sacrificing cell lifetime.

There are several approaches that can be taken in the improvement of Li-ion batteries. Improvements can be made to existing positive and negative electrode materials to increase specific capacity, energy density, and cycle life. Further, novel electrode materials may prove to accelerate the capabilities of modern Li-ion cells. Significant work has gone into the study and development of electrode materials since the advent of Li-ion batteries in the early 1990s[3-5]. Another avenue that can be considered in the quest to improve Li-ion batteries is in the development of electrolyte solutions. The choice of electrolyte can have profound impacts on the cycle life and charge rate capability of a cell. Again, much work has gone into understanding how Li electrolytes work and their development for high performance batteries. The influential reviews of Li electrolytes by

Xu highlight the rich history of electrolyte development for Li-ion batteries[6,7]. However, the electrolytes that are used today in commercial cells strongly resemble those that were used in the early days. This signals a need for further development into novel, commercially viable electrolytes for Li-ion cells. The work contained in this thesis investigates the physical properties of several new electrolyte systems that are starting to gain attention.

Further, testing and optimization of electrolytes for Li-ion cells can be costly and time consuming. The development reliable modeling techniques to accurately predict the properties of electrolyte solutions can greatly reduce the cost and time required. However, some experimental validation is required for such models, especially for electrolyte systems that have not previously been studied. This thesis aims to validate one such model, the Advanced Electrolyte Model (AEM), developed by Gering[8-10] for certain electrolyte properties.

The remainder of this Chapter will give a brief overview of Li-ion battery technology. Chapter 2 will give a broad overview of electrolytes for use in Li-ion batteries. Some of the most popular solvents, salts, and additives used in Li-ion batteries will be discussed. Further, some of the concepts behind ionic transport in electrolyte solutions are introduced. Finally, a summary of the governing equations for the Advanced Electrolyte Model's calculations for ionic conductivity and viscosity is presented. Chapter 3 presents the experimental methods used in this thesis. A new method for the automated measurement of viscosity as a function of temperature is described, as well as a setup for temperature dependent conductivity measurements. The methodology for preparation and electrochemical testing of Li-ion cells is presented in this Chapter. For

measurements of phase diagrams of electrolyte systems, differential thermal analysis (DTA) has been adopted for use with full prismatic-style Li-ion cells, and the setup is described briefly. Chapter 4 shows results for the transport properties of carbonate-based electrolytes containing esters, showing that the addition of esters improves both the viscosity and conductivity of the electrolyte. The ester, methyl acetate (MA), is the focus of this Chapter. A Walden-like analysis is performed to assess the degree of ion dissociation for electrolytes containing MA. Cycling results are presented for cells with MA in the electrolyte, showing a marked improvement in rate capability compared to cells with traditional carbonate electrolytes. Chapter 5 presents the transport properties of electrolytes with low concentrations of ethylene carbonate (EC). Much like in Chapter 4, viscosity and conductivity results are presented, followed by a Walden analysis to obtain a qualitative understanding of the degree of ion association in this class of electrolytes. Also found in Chapter 5 is an investigation of the phase diagram of the ternary system EC:dimethyl carbonate (DMC):$LiPF_6$ using DTA. Finally, cycling results are presented for cells that do not contain EC in the electrolyte. Chapter 6 will conclude the thesis and present a discussion of possible future work.

Some portions of this thesis have appeared in peer-reviewed articles. The description of the viscosity setup in Chapter 3 can be found in L.Y. Beaulieu, E. R. Logan, K. L. Gering, and J. R. Dahn, Rev. Sci. Instrum. **88**, 095101 (2017). The results shown in Chapter 4 have been published in: E. R. Logan, E. M. Tonita, K. L. Gering, J. Li, X. Ma, L. Y. Beaulieu, and J. R. Dahn, J. Electrochem. Soc. **165**, A21 (2018). Results presented in Chapter 5 can be found in E. R. Logan, E. M. Tonita, K. L. Gering, L. Ma, M. K. G. Bauer, J. Li, L. Y. Beaulieu, and J. R. Dahn, J. Electrochem. Soc. **165**, A705

(2018). The authors and co-authors of these publications are thanked for their respective contributions to this work. The specific contributions of the author of this thesis are described at the beginning of each respective chapter.

1.2 LITHIUM ION BATTERIES

Figure 1.1 shows a basic schematic of a Li-ion cell during a charge cycle, highlighting the essential components of a cell. A basic Li-ion cell consists of positive and negative electrodes, a separator, an electrolyte, and metallic current collectors adhered to each of the electrodes. The positive and negative electrodes are where Li ions are stored in the cell's discharged and charged states, respectively. During charge, which is pictured in Figure 1.1, Li^+ leaves the positive electrode, is transported through the electrolyte, and is inserted into the negative electrode. Electrons in the external circuit also move towards the negative electrode while the cell is being charged. Current collectors act to provide a pathway of high electronic conductivity to the electrode materials for electrons traveling through the circuit. For typical Li-ion cells the positive electrodes use an Al current collector, while negative electrodes use current collectors made from Cu. It is essential that current collectors do not react with any other components of the cell. The separator is a microporous membrane that acts to electrically isolate the positive and negative electrodes during operation. The separator must also allow for the passage of ions so that Li^+ may travel between the electrodes during charge or discharge.
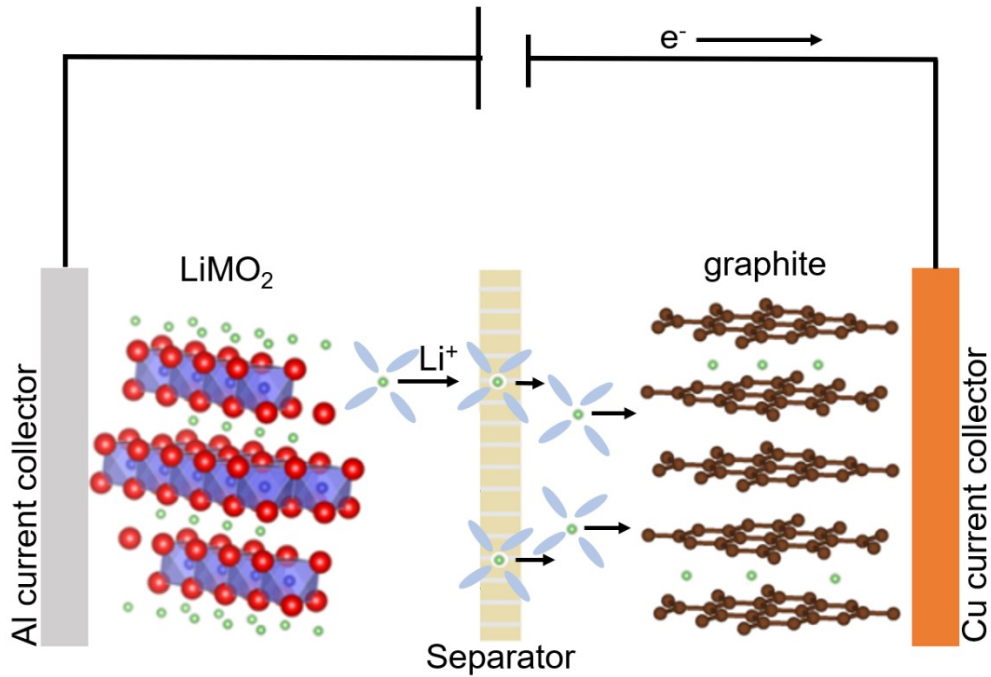
Figure 1.1: Schematic for a generic LiMO$_2$/graphite Li-ion cell during a charge cycle.

The electrolyte facilitates the transport of Li$^+$ through the cell and between the electrodes. In liquid electrolytes, migrating Li ions do not travel as bare ions. Instead, they interact strongly with surrounding solvent molecules and form a larger effective diameter known as a "solvation shell". This is reflected in Figure 1.1. Solvation of migrating ions will be considered in the discussion of transport in electrolyte solutions in Chapter 2. Typically, the electrolyte used for Li-ion cells consists of a blend of organic solvents and a Li salt as a solute. However, several different types of electrolytes exist in one stage of development or another. These include, but are not limited to: aqueous solutions, polymer electrolytes, and solid electrolytes. This thesis focuses exclusively on non-aqueous electrolyte solutions, however the reader should be aware that other classes of electrolytes exist. Several non-aqueous electrolyte systems that are used in Li-ion cells,

as well as models of transport in liquid electrolytes will be covered more thoroughly in Chapter 2.

1.2.1   Electrodes

An electrode in a Li-ion cell primarily contains active material (> 90% by weight), with small amounts of binder and a conductive additive[5]. The most common binder material for these electrodes is polyvinylidene fluoride (PVDF), and the conductive additive typically used is carbon black or graphite[5]. The active material is where Li ions are stored during operation of the cell. The materials used for active material in Li-ion cells are intercalation compounds. Intercalation compounds allow for species such as Li ions to be inserted (intercalated) into vacant sites in the material. Most intercalation compounds used for Li-ion batteries are layered materials, although spinel and olivine "tunneled" materials have been used in some cases. For the positive electrode, Li transition metal oxides of the form $LiMO_2$ are typically used, where M represents one or more transition metals. The metal oxide species form layers, with the Li species existing in sites between these layers. For the first Li-based secondary batteries, Li metal was used at the negative electrode. However, after various safety issued were discovered when using electroplated Li in a full cell (dendrite formation, thermal issues), this cell design was largely abandoned. Now, intercalation materials are also used for the negative electrode. The most popular material by far is graphite, but other materials may be used, including hard carbon-based electrodes or carbon-silicon composites.

The positive and negative electrodes combined with an electrolyte solution and a separator constitute a full Li-ion cell, such as the one shown in Figure 1.1. Assuming a generic $LiMO_2$ positive electrode where M can be a mixture of transition metals and a

graphite negative electrode, during charge Li^+ is removed from the positive electrode (de-intercalated) by the following reaction

$$LiMO_2 \rightarrow Li_{1-x}MO_2 + xLi^+ + xe^- \qquad (1.1)$$
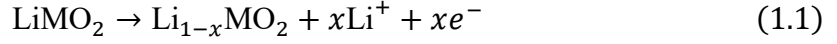
From here, solvated Li-ions in the electrolyte solution transport through the electrolyte towards the negative electrode. At the same time, the electrons produced in Equation 1.1 travel through the external circuit towards the negative electrode. Equation 1.1 is not a thermodynamically favorable reaction, so an external power source is required for this reaction to occur. Figure 1.2 shows the structure of a $Li[Ni_{1-x-y}Mn_xCo_y]O_2$ (NMC)-type material in its fully lithiated (pristine) form in the (110) direction. This view gives a good illustration of the "stacked" nature of these materials. Li is found in between layers of transition metal oxides. As the cell is charged, Li is removed randomly from the layers by Equation 1.1.
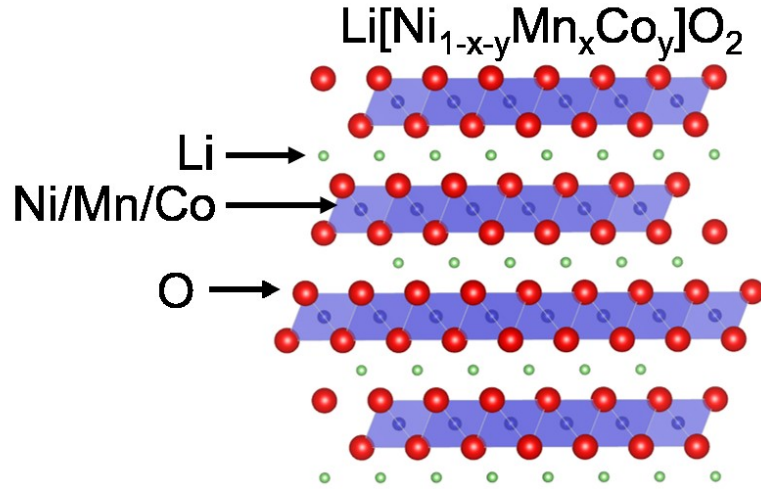
Figure 1.2: Crystal structure in the (110) direction for a generic $Li_x[Ni_{1-x-y}Mn_xCo_y]O2$ species in its fully lithiated form. The Li, O, and transition metal species are labeled.

At the negative electrode, using graphite as an example, the Li ions shed their solvation shell and are intercalated into the graphene layers during charge

$$C_6 + y\mathrm{Li}^+ + ye^- \rightarrow \mathrm{Li}_y C_6 \qquad (1.2)$$

Visualizations of the crystal structure of the graphite before and after lithiation is shown in Figure 1.3. Figure 1.3(a) shows pristine graphite with ABABAB stacking. This means that adjacent graphene layers are not lined up exactly. Figure 1.3(c), which shows the same graphite structure viewed down the c-axis, gives a good visualization of how adjacent layers are shifted. Fully lithiated graphite has one Li for every 6 carbon atoms (LiC$_6$) and is shown in Figure 1.3(b). In the fully lithiated form of graphite, the carbon layers now conform to AAA stacking, where each individual layer is lined up, as can be seen in panel (d) of Figure 1.3.
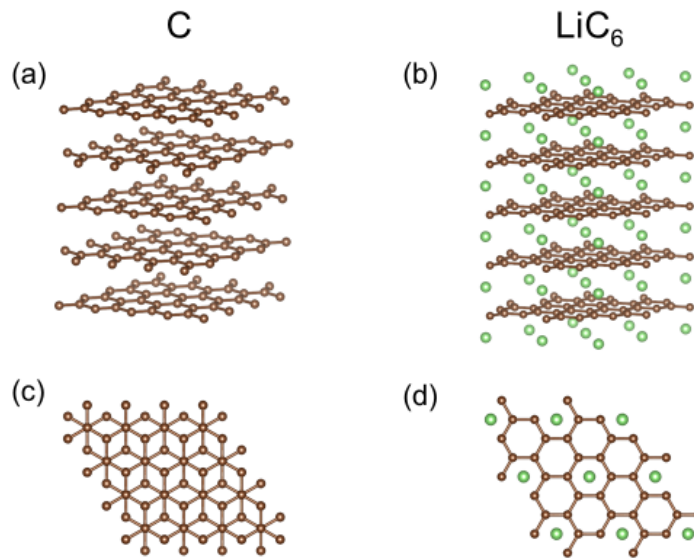
Figure 1.3: Crystal structures of (a) pristine graphite with ABABAB stacking, and (b) fully lithiated graphite (LiC$_6$). Structures (b) and (d) show top views (along the c-axis) of pristine graphite and lithiated graphite, respectively.

The half reactions of the positive and negative electrodes (Equations 1.1 and 1.2, respectively) are combined to find the full cell reaction during charge

$$\mathrm{LiMO}_2 + x/y\, C_6 \rightarrow x/y\, \mathrm{Li}_y C_6 + \mathrm{Li}_{1-x}\mathrm{MO}_2 \qquad (1.3)$$
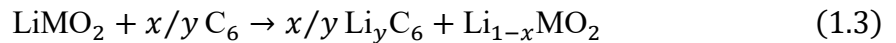
In theory, the stoichiometric coefficients x and y have the limits $0 \leq x, y \leq 1$, corresponding to complete lithiation and de-lithiation of the cathode material and the graphite, respectively. However, these extreme values are typically not reached in practice. LiCoO$_2$ (LCO) experiences detrimental structural changes beyond about 70% of its theoretical capacity[3,5], and NMC-type materials are kept below their theoretical capacity to prevent excessive electrolyte oxidation at high voltage. The graphite is taken to just below its theoretical capacity ($y \approx 0.96$) to avoid the onset of Li plating at the surface of the graphite. The lithiation/de-lithiation reaction should be reversible, so during discharge the reverse of Equation 1.3 occurs. Li is removed from the graphite and re-inserted into the layered metal oxide, while electrons travel through the external circuit from the negative electrode to the positive electrode and power an external load. This constitutes the basic operation of a Li-ion cell. This reaction should be able to run reversibly for many cycles for an effective cell. However, over time unwanted parasitic reactions between the charged electrode materials and the electrolyte will reduce the capacities x and y of the positive and negative electrodes, respectively, and lower the total amount of charge that can be delivered in a given cycle, and eventually lead to the failure of the cell.

Typical voltage vs capacity curves for typical Li-ion battery materials are shown in Figure 1.4. Figure 1.4(a) shows a single charge-discharge cycle for a Li[Ni$_{0.6}$Mn$_{0.2}$Co$_{0.2}$]O$_2$ (NMC622)/Li cell, and Figure 1.4(b) shows a charge-discharge cycle for a graphite/Li half-cell. The NMC sample reaches a voltage of about 4.6 V at a specific capacity of around 250 mAh/g. The graphite cell lowers in voltage as Li is inserted, approaching a value just above 0 V vs Li$^+$/Li at the top of charge. Notice distinct

plateaus in the graphite voltage profile; these plateaus are caused by Li ordering in between the graphene layers during insertion. Instead of being randomly distributed throughout the graphite during charge, the inserted Li instead forms distinct "stages", where Li layers form in an ordered pattern[11]. For example, stage-3 would mean there is a Li layer for every three graphene layers. At the highest state of charge (LiC_6), the lithiated graphite forms stage-1, which is one Li layer for every graphene layer. Stage-1 LiC_6 is what is pictured in Figures 1.3(b) and (d). The voltage of a full cell containing these electrodes would simply be the positive half-cell potential minus the negative half-cell potential at a given state of charge of the cell.
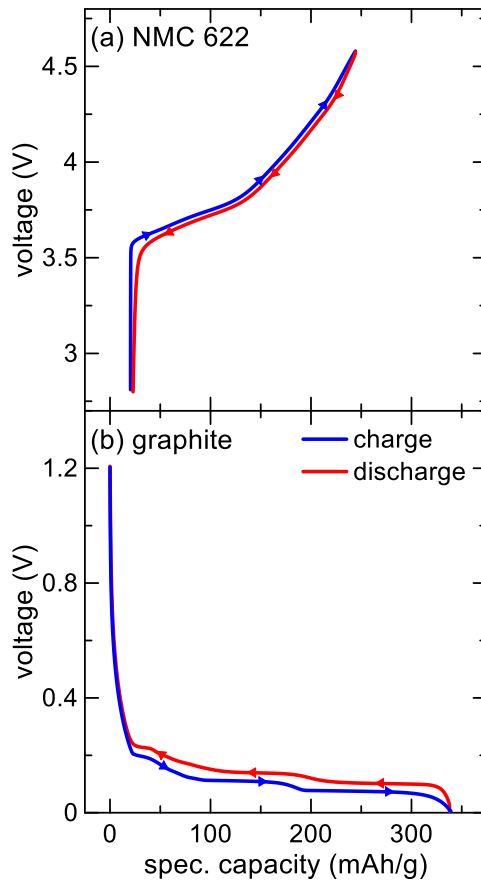
Figure 1.4: Voltage curves for (a) a $LiCoO_2$/Li half-cell, and (b) a graphite/Li half-cell, showing the voltage profiles vs Li^+/Li as a function of specific capacity for a single charge and discharge cycle. Both the LCO and graphite samples in (a) and (b) were charged and discharged at a rate of C/20.

1.2.2 Active Materials

As mentioned above, the most common active materials for Li-ion cells are layered Li metal oxides, $LiMO_2$. The positive electrode material used in the first commercial Li-ion cell produced by Sony, and still one of the most popular choices for commercial cells today is Li_xCoO_2, (LCO)[2]. Today, however, there are many more advanced positive electrode materials that follow the basic $LiMO_2$ structure. Many of these materials have been developed with cost in mind, aiming to replace the costly and rare cobalt[3,12]. Of note is $LiNi_{1-x-y}Mn_xCo_yO_2$, known as NMC. Electrodes utilizing this material use considerably less Co (typically, $y < 0.4$), and can reach capacities comparable to that of LCO. They can also reach voltages comparable to that of LCO, leading to similar energy densities between the materials. Another related material, $Li[Ni_{1-x-y}Co_xAl_y]O_2$ (NCA) has an even higher capacity than LCO, while using much less Co in the active material. These three electrode chemistries, LCO, NMC, and NCA make up much of the market for positive electrode materials for commercial Li-ion cells[2]. Some other, less utilized chemistries that deserve mention are $LiFePO_4$ (LFP), and $LiMn_2O_4$ (LMO). LFP has a lower average voltage than LCO-type materials, leading to a much lower energy density. However, this material is extremely thermally safe and inert to other cell components, so may have potential applications in certain niches. LMO is significantly less expensive than either LCO, NMC, or NCA, however this comes at the cost of a much lower specific capacity. Again, for specific applications where low cost and reliable safety are essential and extremely high energy density is not required, this chemistry may be preferred over the other, more expensive options. For all full cells tested in this thesis, NMC-type materials are used in the positive electrode.

As mentioned above, graphite is typically used in the negative electrode in Li-ion batteries. Like LCO and other layered Li-ion positive electrode materials, graphite also stores Li ions via intercalation. In graphite, Li is stored in between the graphene layers. Figure 1.3 shows views of (a) pristine graphite, and (b) fully lithiated graphite (LiC_6). The addition of lithium ions between the graphene layers leads to a corresponding expansion in the c-axis of the structure. This leads to a relatively small volume expansion of the electrode. Graphite electrodes have very high specific capacities compared to typical positive electrode materials, typically around 350 mAh/g[5]. Lithiated graphite also has a very low potential, close to 0 V vs Li^+/Li, as seen in Figure 1.4. This allows for full cells to have very high voltage, since the voltage of the full cell at a given state of charge is the potential of the positive electrode minus the voltage of the negative electrode. At low charge/discharge rate, and depending on the electrolyte used, the potential of the graphite electrode approaches, but does not pass below the Li plating potential.

Graphite is not the only non-metallic negative electrode used in Li-ion batteries. In the first commercialized cells made by Sony, hard carbon (coke) electrodes were used. These electrodes have good specific capacity but are not competitive with the high volumetric capacity of graphite-based electrodes. Hard carbon electrodes fell out of favour after the development of effective graphitic electrodes. Another negative electrode worthy of mention is lithium titanate, $Li_{4/3}Ti_{5/3}O_4$ (LTO). LTO has a much higher average voltage than graphite-based electrodes (~1.5 V), and as a result, has extremely low reactivity with electrolyte components. This means cells made with LTO negative electrodes have extremely high cycle lives, albeit with much lower energy densities than graphite-based cells. Si and Si-alloy electrodes have also been studied for use in Li-ion

batteries, primarily due to the extremely high volumetric and gravimetric capacity of Si compared to graphite[4]. Si negative electrode have considerable issues, though, including extremely high volume expansion on lithiation.

1.2.3   Separators

The separator is a key, and often underappreciated component of Li-ion cells. In a general sense, a separator is a porous material that blocks the passage of electrons directly between electrodes, which would short the cell. The separator must allow the flow of ionic current, however, as the transport of Li^+ is required for charge and discharge of the cell. Like the other components of a Li-ion cell, the separator must not react with any other cell components, including electrodes and electrolyte. Separators may also act as an added safety mechanism for Li-ion cells. Above a threshold temperature, the separator should "shutdown" the cell, and no longer allow current to flow, thus preventing a thermal runaway event[13]. Separators for Li-ion batteries are typically composed of either microporous polyethylene (PE) or polypropylene (PP), or a combination of the two.

1.2.4   Solid electrolyte interphase

While not strictly necessary for a Li-ion cell to cycle, the solid electrolyte interphase (SEI) is essential to the successful operation of a cell over many cycles. The SEI is a thin film that exists on the surface of the negative electrode (typically graphite) as well as the positive electrode, and physically separates the electrode particles from the electrolyte. The SEI layer is formed by initial oxidation/reduction of components of the electrolyte at the highly reactive positive (>4.0 V vs Li^+/Li) and negative (~0 V vs Li^+/Li) electrodes during the first charge of the cell. The formation of this layer acts to hinder further

parasitic reactions between the electrolyte and the electrodes, which in turn increases the lifetime of the cell. The SEI is electrically insulating, so the transfer of electrons between the electrode and electrolyte is extremely limited, but it also allows for the transport of Li^+ through the layer by solid state diffusion. The SEI in a Li-ion cell is one of the most controversial topics in the field. On one hand, it is generally understood that the SEI is essential for the operation of cells over many cycles. On the other hand, the mechanisms for formation and the composition of the SEI are not fully understood, and often not agreed on[7,14,15]. A brief overview of the SEI layer is given below, with care taken not to broach any especially controversial topics, as this discussion would be well beyond the scope of this thesis.

The majority of the SEI layer is formed during the first cycle of a cell, also called the "formation" cycle. At this point, the bare electrode is exposed to the electrolyte, allowing various reactions to occur as the cell is charged. After this initial cycle, various electrode/electrolyte reactions will still occur over the lifetime of the cell, but at considerably lower rate. During the formation of the SEI, some Li is consumed and incorporated into the layer, thus reducing the total amount of usable Li in the cell. As a result, the difference between the initial charge and discharge capacities (also known as the irreversible capacity) is about 7-10% for the formation cycle.

The question that remains is the exact composition and morphology of the SEI layer. While it is still a hotly debated topic, it is generally understood that cyclic carbonates such as ethylene carbonate (EC) and propylene carbonate (PC) are reduced on the surface of the graphite electrode on the first cycle, while linear carbonate solvents such as ethyl methyl carbonate (EMC) or dimethyl carbonate (DMC) do not contribute to

14

the SEI Layer. It has been shown that the primary reduction product of EC in a lithium electrolyte is Li ethylene dicarbonate (LEDC)[16]. Several reaction mechanisms for the reduction of EC and PC on graphite surfaces have been proposed[7].

In addition to these organic components contributing to the SEI, there are some inorganic components that are formed on the electrode surface during formation. One example is LiF, which is likely formed from the reduction of PF_6^- anions in electrolytes containing $LiPF_6$ as the conducting salt. Several electrolyte additives have been found that also reduce on the graphite surface to form protective films, such as vinylene carbonate (VC) and fluoroethylene carbonate (FEC). Perhaps not surprisingly, these compounds have very similar chemical structures to the cyclic carbonates EC and PC (see Chapter 2). From here, the exact structure and morphology of the SEI is still under debate. Nevertheless, the SEI, whatever its composition, remains one of the miracles of Li-ion technology, enabling both high voltage operation and long cycle life of cells.

CHAPTER 2   ELECTROLYTES IN LI-ION BATTERIES

The electrolyte in a Li-ion cell facilitates the transport of Li ions between the two electrodes, and through the separator during charge and discharge, making it an indispensable component of Li-ion batteries. Due to the aggressive electrochemical conditions during operation of a Li-ion cell, there are strict requirements for an effective Li electrolyte. First, all components of the electrolyte (solvents, salts, additives) must be reasonably electrochemically inert. They must be resistant to oxidation reactions at the positive electrode (~4.5 V vs Li$^+$/Li) and reduction reactions at the negative electrode (~0 V vs Li$^+$/Li). They must have low viscosities and high conductivities to allow for Li$^+$ transport at high charge and discharge currents. The solvents used in the electrolyte must have high enough dielectric constants to allow for dissolution of the Li salt in solution to provide mobile charge carriers. Further, the electrolyte solution must remain in the liquid phase over the operating temperature range of the battery. Finally, the electrolyte must be reasonably safe and inexpensive for it to be considered viable for commercial applications. This is a very demanding list of requirements, and already limits the set of possible components for a Li electrolyte. However, over the years several electrolyte systems have been developed that are competitive in most or all the above-mentioned categories.

What follows below is a discussion of the various components of Li-electrolytes that have been used in the past and present. This is by no means an exhaustive list, and many classes of electrolytes (aqueous, polymer, solids) have been omitted entirely. Excellent reviews of electrolytes for Li-ion batteries can be found in References 6 and 7. Following the discussion of the various components of Li electrolytes that are used in

practice, a broad introduction will be given on the theory of transport in electrolyte solutions. Several models will be presented, both theoretical and empirical in nature. Finally, the Advanced Electrolyte Model (AEM) will be introduced, which is an extension of well-known theories of electrolyte transport and features prominently in the following chapters of this thesis.

2.1 ELECTROLYTE COMPONENTS

2.1.1 Carbonate solvents

Most commercial Li electrolytes utilize non-aqueous organic solvents. Of these, most electrolytes use carbonate solvents. Carbonate solvents have reigned supreme over the years due to their good electrochemical stability, high dielectric constants (in some cases), low viscosities (in some cases), film forming properties (again, in some cases, see below), and large liquid ranges. The chemical structures of some common carbonate solvents are shown in Table 2.1, along with basic physical properties such as melting point (MP), boiling point (BP), viscosity, and dielectric constant at room temperature.

Immediately, it should be noticed from the chemical structures of the carbonates used in Li electrolytes that there are two main classes of carbonate solvents. First are the cyclic carbonates, including ethylene carbonate (EC), and propylene carbonate (PC). These solvents have a cyclic ring structure. The second group of carbonate solvents are linear, and include ethyl methyl carbonate (EMC), dimethyl carbonate (DMC), and diethyl carbonate (DEC). It can be seen from Table 5.1 that this difference in structure translates to a corresponding difference in physical properties. While the liquid range of these compounds are quite similar (apart from EC), the cyclic carbonates EC and PC

have extremely high viscosities and dielectric constants, and the linear carbonates all have very low viscosities and dielectric constants. It appears that these two properties are at odds with one another, as it is difficult to find a solvent with the desirable properties of high dielectric constant and low viscosity, the obvious exception to this rule being water. For the carbonates, this stark difference in physical properties can be related directly to their chemical structure. Xu states[6]:

> "The origin for the effect of molecular cyclicity on the dielectric constant has been attributed to the intramolecular strain of the cyclic structures that favors the conformation of better alignment of molecular dipoles, while the more flexible and open structure of linear carbonates results in the mutual cancellation of these dipoles".

Essentially, this suggests that the linear structure of carbonates such as EMC or DMC allows these molecules to orient themselves in a more random distribution, which in turn cancels out much of the dipole contributions of the individual molecules. The small net orientation of these solvents leads to the low dielectric constant.
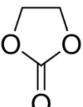
Name	MP (°C)	BP (°C)	Dielectric constant at 25°C	Viscosity at 25°C (cP)	Structure
Ethylene carbonate (EC)	36.4[17]	248[17]	89.78 (40°C)[17]	1.93 (40°C)[17]	
Propylene carbonate (PC)	-48.8[6]	242[6]	64.92[6]	2.53[6]	
Ethyl methyl carbonate (EMC)	-53[17]	110[17]	2.958[18]	0.65[18]	
Dimethyl carbonate (DMC)	4.6[18]	90[18]	3.1075[18]	0.59[18]	
Diethyl carbonate (DEC)	-74.3[6]	126[6]	2.805[6]	0.75[6]	

Table 2.1: Chemical structures, melting points, boiling points, dielectric constants and viscosities at room temperature for the most common carbonate solvents used for Li electrolytes.

PC was initially studied as a solvent for Li metal batteries. Its high dielectric constant allowed for dissolution of Li salts, and its low melting point made it a more desirable solvent over its relative EC, which is solid at room temperature. However, there are significant limitations for the use of PC in Li-ion batteries. The use of PC in Li-ion batteries with graphite negative electrodes was found to cause catastrophic capacity loss. This was later understood to be due to co-intercalation of PC in the graphite negative electrode, which caused exfoliation of the graphite layers, leading to capacity loss. Presently, PC is not favoured as an electrolyte solvent for Li-ion batteries, however there

has been some considerable effort to overcome the exfoliation issue to allow for the use of PC once again, and now several additives, salts and solvents exist that suppress PC co-intercalation to some extent[7].

After the limitations of PC were understood, attention was shifted to EC, which has a very similar structure. Unlike PC, EC does not co-intercalate into graphite anodes, so exfoliation and subsequent capacity loss is not observed. EC does, however, react with graphite at the electrode surface during operation of the cell. Far from being a harmful process, the reaction of EC at the electrode surface forms a passivating layer, now called a solid electrolyte interphase (SEI, see Chapter 1). This effectively limits further electrolyte/electrode reactions, allowing for a cell to be cycled many times without significant capacity loss. The small difference in chemical structure between EC and PC has caused significant differences in their performances in Li-ion batteries. Due to the film-forming properties of EC, it is generally considered an indispensable component of Li-ion battery electrolytes[19].

The problem with EC is that by itself, it is a solid at room temperature, and its viscosity is very high. While an EC-based electrolyte solution can be made at room temperature due to melting point depression on the addition of salt, the viscosity is still very high, leading to a uselessly low ionic conductivity. The remedy for this, originally found by Saito and Matsuda[20-22], is to mix high viscosity EC with one or more low viscosity solvents, obtaining an overall low viscosity mixture. Using this approach, one can produce an electrolyte that retains much of the high dielectric constant of EC, while reducing the total viscosity of the system. Typically, a combination of the linear carbonates EMC, DMC, and DEC are used as low-viscosity co-solvents.

In addition to reducing the viscosity of EC-containing electrolytes, linear carbonates have other desirable properties that lend well to their use in a Li-ion cell. As seen in Table 2.1, the liquid ranges of these solvents are much wider than either cyclic carbonate. Apart from DMC, all the linear carbonates freeze well below 0°C. As a result, mixing either EC or PC with any combination of linear carbonates will depress the liquidus transition of the hybrid system low enough that Li-ion batteries containing these electrolytes will still operate well in low-temperature conditions.

One peculiarity to note is in the abnormally high melting point of DMC (4.6°C compared to -53°C for EMC). This may cause issues for cell operation at low temperatures in cells that contain high concentrations of DMC. As an attempt to remedy this issue, electrolytes containing ternary or even quaternary solvent blends have been studied[23-27]. Adding a third or fourth solvent into the electrolyte has been shown to improve low-temperature cycling as well of the ionic conductivity of electrolytes.

Another benefit of these low-viscosity linear carbonates is in their impacts on the electrochemical stability of electrolytes in Li-ion cells at high voltage. In addition to the issues with graphite anodes in Li-ion batteries, PC will readily oxidize on the charged cathode at elevated voltages (> 4.0 V vs Li^+/Li). Mixtures of EC with linear carbonates, are very stable at high voltage in Li-ion cells. It should be noted that recently, however, studies of high-energy Li-ion cells found evidence of excessive EC reduction when cells are charged to very high voltage (≥ 4.5 V vs Li^+/Li)[28]. Therefore, there has been a push to find electrolytes with even higher anodic stability while maintaining the relatively high conductivity that is achieved with the addition of EC to the electrolyte.

There does not exist a single carbonate solvent that achieves all the properties required of a Li electrolyte outlined at the beginning of this chapter. However, it has been found over the years that mixing different carbonate solvents can minimize their less desirable properties while maintaining many of the good properties that are required for a Li electrolyte. As such, electrolytes containing EC mixed with linear carbonates have dominated the commercial landscape since the advent of Li-ion cells in the early 1990s. Most likely, carbonate-based electrolytes will continue to dominate for the foreseeable future, albeit with the addition of different additives and co-solvents, discussed below.

2.1.2 Esters

Due to their extremely low melting points, aliphatic esters were first investigated by Smart et al. for use in Li-ion batteries for space applications[27]. Before this, esters also found some attention for use in Li metal batteries[29]. Requiring stable operation of cells at much lower temperatures than anything found on Earth, the low melting points and low viscosities of linear carbonates were not enough for these applications. The basic physical properties as well as chemical structures of some ester solvents are given in Table 2.2. First notice the similarities in chemical structure between the esters and the linear carbonates shown in Table 2.1. The only difference in structure is that they are missing the second -O- bond that is found in the linear carbonates. Overall, they have lower viscosities, larger liquid ranges, and slightly higher dielectric constants. Obviously, these are all desirable properties: lower viscosity should promote higher conductivity in the electrolyte and improve low temperature and high rate cycling, the larger liquid range is ideal for extreme low temperature conditions, and the higher dielectric constant may promote the further dissociation of Li salt in the solution.

For these desirable properties, esters have received considerable research attention for Li-ion battery electrolytes since the original work of Smart et al. in 1999[27]. Smart et al. have found that the addition of esters as co-solvents can improve the conductivity of the electrolyte and the cycling performance of cells at low temperature ($< 0°C$). However, it was also found that the effectiveness of the ester co-solvent over many cycles depended on the molecular weight (MW) of the ester being added. Low MW (short chain) esters such as MA or EA apparently did not form favorable SEI layers and led to increased polarization and impedance at the electrodes[30]. High MW esters such as EB, while providing a smaller increase in conductivity than MA or EA, formed more desirable SEI layers than the small MW esters. Ester co-solvents have also been studied for use in electric double layer capacitors (EDLCs). Jänes and Lust used carbonate-based electrolytes with ester co-solvents to replace toxic acetonitrile (AN), while maintaining the high power density required in an EDLC[31,32].

Esters have also been shown to be viable as the primary solvent in a Li electrolyte. Petibon et al. showed that high voltage cells with good capacity retention can be constructed using MP or EA as the primary solvent in the electrolyte, provided that a minimum of 3% w/w of additives such as vinylene carbonate (VC) are added to the electrolyte to form a passivating SEI at the graphite negative electrode[33,34].
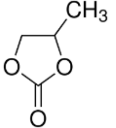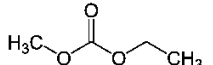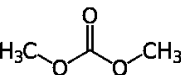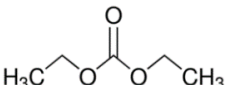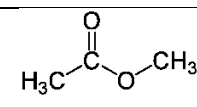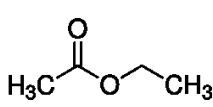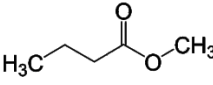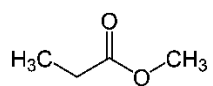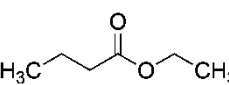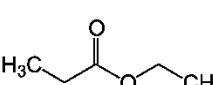
Name	MP (°C)	BP (°C)	dielectric constant at 25°C	Viscosity at 25°C (cP)	Structure
Methyl acetate (MA)	-98[18]	57[18]	6.68[18]	0.40[30]	
Ethyl acetate (EA)	-84[35]	77[35]	6.00[32]	0.46[30]	
Methyl butyrate (MB)	-85.8[35]	102.8[35]	5.48[35]	0.54[35]	
Methyl propionate (MP)	-87.5[35]	79.8[35]	6.20[35]	0.43[35]	
Ethyl butyrate (EB)	-93[30]	120[30]	5.18[36] (30°C)	0.639[36]	
Ethyl propionate (EP)	-73[30]	99[30]	5.76[36] (20°C)	0.711[30]	

Table 2.2: Physical properties and chemical structures for several selected ester solvents. All properties are given at 25°C unless otherwise noted.

The impact of addition of esters, and MA in particular to the charge rate capability of Li-ion cells has been studied further in recent years. Ma et al. considered the impact of the esters MA, MP, MB, and EA on the onset of Li plating at high charge rate in Li-ion cells, as well as long term capacity retention of cells containing these esters[37,38]. Glazier et al. found evidence of oxidation of MA at elevated voltage in cells with electrolytes containing this co-solvent, leading to slightly lower capacity retention over many cycles compared to MA-free cells[39]. Li et al. showed that using MA as a co-solvent in single crystal NMC 532/ graphite cells increased the rate capability of these cells,

while slightly lowering the long-term capacity retention due to oxidation of MA at the cathode[40].

2.1.3 Lithium salts

Lithium salts are added to the solvents described above to provide mobile Li ions to carry charge between the positive and negative electrodes during charge and discharge of a cell. A Li salt should be able to fully (or almost fully) dissociate in the solvent blend to which it is added. The anion of the salt, which is not directly involved with any electrochemical reactions during cell operation, should be stable against oxidation, and should not react with any other cell components, whether chemically or electrochemically. This includes solvent molecules, positive and negative electrodes, separators, current collectors, and cell packaging materials. Further, like the solvent molecules and electrode active materials, it is desirable for the Li salt to be non-toxic and inexpensive for manufacturing purposes. Finally, the Li salt must not decompose at elevated temperature. Again, this is a rather tall order given the aggressive conditions of a Li-ion cell during operation. As Xu notes, there are significantly fewer Li salt candidates than there are possible solvents[6]. One reason is that basic Li salts like Li halides are not feasible in non-aqueous solvents because the high charge density of halide anions makes dissociation of the salt extremely difficult. Instead, many of the Li salts that have been used in Li-ion battery electrolytes have similar chemical structures. Many of these salts have large anions to distribute the surface charge density, which aids dissociation. Table 2.3 shows some of the most well-studied Li salts, along with some of their basic physical properties.

The most widely used salt of the different candidates shown in Table 2.3 is $LiPF_6$. $LiPF_6$ does not perform the best in any of the categories mentioned above, but more importantly it does not perform poorly in any of these categories. It has good ionic mobility, dissociates easily, has excellent anodic stability, and is not overly toxic or reactive to the various cell components. Most of the other potential Li salts have at least one characteristic that prevents them from being used in commercial cells. $LiClO_4$ electrolytes have good conductivity and form SEI layers with low impedance. However, it is highly reactive at high temperature and current due to the +7 oxidation state of Cl[41]. $LiBF_4$ is less reactive than $LiClO_4$, but does not dissociate easily, leading to relatively low conductivity[42]. $LiAsF_6$ performs well in most regards, but the toxicity of As(III), which is formed in the reduction of AsF_6^-, has prevented it from being used commercially[6].

Name	Molecular Weight (g/mol)	MP (°C)
$LiPF_6$	151.9	200
$LiBF_4$	93.9	293
$LiAsF_6$	195.9	340
$LiClO_4$	106.4	236

Table 2.3: Basic physical properties of several well-known Li-salts. The data comes from Ref. 6.

Although $LiPF_6$ is the salt of choice for most commercial Li-ion cells, it still has some significant flaws. A thermodynamically favorable, albeit kinetically sluggish reaction at ambient temperatures causes $LiPF_6$ to decompose into solid LiF and PF_5. Small amounts of LiF may be incorporated into the SEI and is highly resistive, and PF_5 can further react with trace moisture to form HF. This issue can partially be remedied by

producing ultra-high purity $LiPF_6$, but this decomposition will still occur to some extent. Nevertheless, $LiPF_6$ still reigns supreme as the best conducting salt for Li-ion batteries.

A few other alternative Li salts have been reported in an effort to replace $LiPF_6$ by trying to overcome some of the drawbacks that $LiPF_6$ poses. Of note are the imides lithium bis(trifluoromethanesulfonyl)imide (LiTFSI) and lithium bis(flurosulfonyl)imide (LiFSI). Their structures are shown in Figure 2.1. LiTFSI was first synthesized in 1984 and soon found interest in the Li-ion battery community[43]. This salt shows a lower mobility than $LiPF_6$, but almost complete dissociation of the ions which gives a good overall conductivity, albeit still lower than $LiPF_6$. LiTFSI is thermally stable, and resistant to hydrolysis unlike $LiPF_6$. However, the major drawback for the use of this salt is that it is extremely corrosive to the Al current collector in full Li-ion cells. The related salt LiFSI has been developed relatively recently[44]. Like LiTFSI, LiFSI exhibits an extremely high degree of dissociation, which suggests that high dielectric solvents may not be required when using this salt. Further, LiFSI also shows resistance to hydrolysis. What sets it apart from its relative LiTFSI is in its conductivity and stability on Al current collectors. While LiTFSI has low ion mobilities, LiFSI exhibits high mobility as well as high dissociation which leads to an ionic conductivity that is higher than that of $LiPF_6$. Further, in extremely pure forms, LiFSI does not corrode the Al current collector at low voltage. Al corrosion only occurs when impurities such as LiCl are present in the salt. Full Li-ion cells containing LiFSI have also been shown to cycle very well compared with "state-of-the-art" electrolytes containing $LiPF_6$[44]. While LiFSI-containing electrolytes may have not replaced $LiPF_6$ in commercial cells as of yet, LiFSI at least

shows that Li salts do exist that can at least compete with $LiPF_6$ in terms of conductivity, and stability.
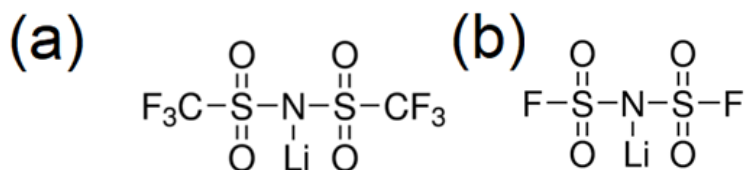
Figure 2.1: Chemical structures of (a) LiTFSI, and (b) LiFSI.

2.1.4   Electrolyte additives

The definition of an "electrolyte additive" is somewhat subjective in nature. In general, an additive is included in an electrolyte mixture in a relatively low proportion (<10% w/w) to improve certain characteristics of the operation of the cell. The purpose of an electrolyte additive can be varied, although generally they are used to improve long term cycling of the cell: they can be added to reduce cell impedance, encourage SEI formation, remove undesirable species such as HF, and prevent over-charge and over-discharge of cells among many other applications. Indeed, in practice often several additives are used in an electrolyte to combine several of these desired effects. Countless different additives for Li electrolytes have been studied over the years, and while a broad discussion of electrolyte additives is well beyond the scope of this thesis, some key additives still deserve mention.

Some of the most successful additives for non-aqueous Li electrolytes can be found in Table 2.4. Notice that the structures of these additives resemble those of EC and PC. The primary functions of the additives used in this thesis are for their SEI forming

properties, much like the cyclic carbonates. Most of these film-forming additives are reduced during the formation cycle of the cell, consuming most of the additive immediately. Vinylene carbonate (VC) is one of the most popular additives used in Li-ion batteries today[7,13]. Its primary function is to form an SEI on the graphite negative electrode, although it has also been shown to form films on the cathode surface as well. 1,3,2-dioxathiolane-2,2-dioxide (DTD) has also exhibits good film-forming properties on the surface of graphite electrodes. One of the major advantages of using this additive is that is has been shown to suppress the co-intercalation of PC into graphite electrodes, thus possibly enabling the use of PC as a solvent in cells containing graphite negative electrodes. Finally, fluoroethylene carbonate (FEC) is also used as an SEI forming additive for the graphite electrode. FEC has been found to form extremely favorable films on graphite. These SEI layers are more dense and thinner than many other additives. FEC has even been found to be a suitable replacement for EC in low-dielectric electrolytes (~95% EMC)[45].

These additives have been shown in many cases to improve capacity retention in Li-ion cells. There are many more effective additives for Li electrolytes, however the three mentioned above are some of the most well-known, and in particular, FEC is used in this thesis.
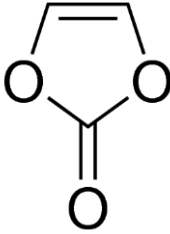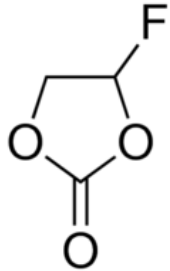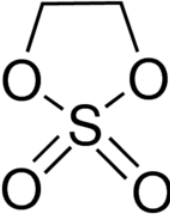
Vinylene carbonate (VC)	
Fluoroethylene carbonate (FEC)	
1,3,2-dioxathiolane-2,2-dioxide (DTD)	

Table 2.4: The names and chemical structures of some common electrolyte additives.

2.2 ELECTROLYTE TRANSPORT PROPERTIES

Robinson and Stokes state, regarding the challenges of describing ion conduction in liquid solutions[46]:

> "The transport of electricity through electrolytes differs fundamentally from metallic conduction in that the carriers are ions, the dimensions and masses of which are much larger than those of the electrons responsible for metallic conduction. The ions of course share in the general Brownian motion of the liquid… In the absence of an external field or a concentration-gradient, the Brownian movement is completely random… The presence of an electric field, as

in conductance, or of a concentration-gradient, as in diffusion, has the effect of biasing the Brownian movement in a particular direction."

There is no exact description of ionic transport in electrolyte solutions due to the complex nature of the interactions between the various ions and solvent molecules in an electrolyte solution. However, there now exist many models of bulk ionic transport that can predict electrolyte transport properties to a high degree of accuracy. In this section, a general picture of ionic transport in electrolytes will be described, and several different models, both empirical and theory-based will be presented.

2.2.1 Ionic conductivity

Ionic conductivity is essentially a measure of the ability of an electrolyte solution to transport (conduct) ions. It is important to note that the quantity of ionic conductivity accounts for *all* ions present in the electrolyte. This means in a Li electrolyte, both the Li^+ and its counter ion (say, PF_6^-) contribute to the conductivity of the solution. Ionic conductivity is an important measure in the screening of electrolyte solutions for Li-ion batteries. In general, ionic conductivity measurements give an indication of an electrolyte's ability to withstand high charge and discharge rates, as well as cycling at low temperatures. As such, conductivity has been reported for countless electrolyte systems for Li-ion batteries[47-58]. A general expression for ionic conductivity, denoted κ, is[6]:

$$\kappa = \sum_i n_i \mu_i z_i e ,$$

(2.1)

where the index i refers to a given ionic species, n_i is the number density of ion i in the solution, μ_i is the mobility of ion i, z_i is the charge on ion i, and e is simply the

elementary charge. The mobility of ionic species i is defined as the ratio of its drift velocity v to the strength of an applied electric field E

$$\mu = \frac{v}{E}.$$

(2.2)

While Equation 2.1 given above is not particularly instructive, some information can be gained from it. The conductivity of the electrolyte depends on the number of free ions in solution. This will become important later in the discussion of iconicity of electrolytes in Chapters 4 and 5. Further, the conductivity also depends on the charge of the ion; it would be expected that an electrolyte solution containing a doubly charged ion, say Ca^{2+}, will be higher than a singly charged ion. However, it will be seen later that this is not necessarily the case because the ionic diameter of the ion also plays an important role in determining ionic conductivity.

As a Li ion and its counter ion transport through an electrolyte solution during charge and discharge, they do not travel through the solution as bare ions. Instead, they are coordinated to (often) several solvent molecules forming a "solvation sheath". This increases the effective diameter of the ion, which will have consequences for its transport. While the exact nature of ion solvation and its structure is complex, some simple approximations can be made to help simplify this analysis. It may be assumed that the solvated ion is spherical and has a drag force during transport that obeys Stokes' Law (low Reynold's number):

$$F_d = 6\pi\eta r v,$$

(2.3)

where η is the viscosity of the medium (in this case, the electrolyte solution), r is the radius of the solvated ion, also known as the Stokes radius, and v is the velocity of the ion. Then, the migrating ion obeys the Stokes-Einstein Equation:

$$D = \frac{k_B T}{6\pi\eta r}. \tag{2.4}$$

Here, D is the diffusion coefficient, k_B is Boltzmann's constant, and T is the temperature of the system. Further, using the Einstein relation which relates the ion mobility to its diffusion constant:

$$D = \frac{\mu k_B T}{ze}. \tag{2.5}$$

An expression can be found that relates mobility to the viscosity of the electrolyte

$$\mu = \frac{ze}{6\pi\eta r}. \tag{2.6}$$

As an aside, it should be noted that most of the ionic transport in a Li electrolyte during the charge and discharge of a cell is due to diffusion rather than migration resulting from an applied electric potential. For example, during charge Li^+ from the positive electrode goes into solution and Li^+ is intercalated into the negative electrode. The resulting concentration gradient drives a flux of Li ions towards the negative electrode, producing an ionic current.

Using Equation 2.6, an expression is obtained for ionic conductivity for ionic species i as a function of viscosity:

$$\kappa_i = \frac{n_i |z_i|^2 e^2}{6\pi\eta r_i} \tag{2.7}$$

$$\kappa_i = \frac{F |z_i|^2 c_i e}{6\pi\eta r_i} \tag{2.8}$$

In Equation 2.8, F is Faraday's constant, and c is the concentration of ion i in mol/cm^3. Finally, adding the contributions of both ions to the solution conductivity:

$$\kappa = \sum_i \frac{F |z_i|^2 c_i e}{6\pi\eta r_i} \tag{2.9}$$

Equation 2.9 states that the ionic conductivity should be inversely proportional to the solution viscosity. There will also be an inverse relationship with the size of the solvated ions, and a proportional relationship with the concentration of ions in solution. The proportionality between ionic conductivity and inverse viscosity (also known as fluidity, ϕ) has been demonstrated for solutions of LiAsF$_6$ in various glyme solvents by Dudley et al.[47].

2.2.2   Salt dissociation in the Stokes' Law conductivity model

The simple model given above uncovers some of the factors that influence ionic conductivity. However, this model can be taken slightly further with a few modifications. Starting with the assumptions that a 1:1 salt is used (e.g. LiPF$_6$), and no higher order charged species such as triple ions are formed in the solution (i.e. the only charge carriers are single ions), the concentration of ions c_i should be the same for both positive and negative ions

$$\kappa = \frac{Fec_\pm}{6\pi\eta} \sum_i \frac{1}{r_i} \tag{2.10}$$

In Equation 2.10, the variable c_i has been re-named $c_\pm$ to reflect that it represents the concentration of positive *or* negative ions in solution, which should be equal since a 1:1 salt is being considered. $c_\pm$ can also be thought of as the total concentration of ionic species in solution (positive and negative) divided by 2. Now, expanding the summation in Equation 2.10,

$$\kappa = \frac{Fec_\pm}{6\pi\eta} \left(\frac{1}{r_+} + \frac{1}{r_-} \right) \tag{2.11}$$

Here, r_+ and r_- represent the Stokes radii (or solvated radii) of the positive and negative ions, respectively. Now, dividing by the concentration of salt added c_0 (not to be confused with $c_\pm$), and defining a new variable that for the combined radii of the ions, Equation 2.11 becomes

$$\Lambda = \frac{Fe}{3\pi\eta R}\frac{c_\pm}{c_0},$$ (2.12)

where $\Lambda = \kappa/c_0$ is the molar conductivity (also called the equivalent conductivity), and $\frac{2}{R} \equiv \left(\frac{1}{r_+} + \frac{1}{r_-}\right)$ is the harmonic mean of the two solvated radii r_+ and r_-. From here, a new variable is defined, $f \equiv c_\pm/c_0$, which is the molar ratio of ionic species (positive or negative) to neutral salt added. The variable f is essentially a simple measure of salt dissociation. With this, and by taking the logarithm of both sides of Equation 2.12, an equation is obtained that resembles the empirical Walden Rule[46]:

$$\log\Lambda = \log\frac{Kf}{R} + \log\frac{1}{\eta}$$ (2.13)

where $K = Fe/3\pi$ is a constant. What is obtained is an equation in terms of the molar conductivity, fraction of ion dissociation, combined solvated radius, and viscosity. Plotting $\log\Lambda$ versus $\log 1/\eta$ (also known as a Walden plot) for a series of salt concentrations or solvent compositions in an electrolyte should provide some information about the ionicity (degree of dissociation) of the system as a function of these parameters. A straight-line plot in this space represents a region of constant ionicity and solvated radius. Using Walden plots as a tool to evaluate ionicity in electrolyte systems was pioneered by Angell. This approach was originally applied to ionic liquid systems[59-65]. Angell's group, as well as others have applied this method in recent years to non-aqueous

electrolyte systems[66,67]. This technique will be applied later in this thesis in Chapters 4 and 5 to several non-aqueous electrolyte systems.

This is not the end of the story for ion transport in electrolytes. Recall from Equation 2.1 that the ionic conductivity κ considers the contributions from *all* ions in an electrolyte solution. However, in an electrolyte for a Li-ion cell, the only ion current that is useful is the current due to Li^+, since anions to not participate in electrochemical reactions during cell operation (hopefully!). Thus, it would be useful to know, instead of the total conductivity of the electrolyte solution, the individual mobility of the Li ion. One way that this is expressed is in the transference number, t_{Li}. In a general sense, the transference number of a species j is the mobility of species j divided by the sum of individual mobilities of the ions present in the solution. This is given as[6]:

$$t_j = \frac{\mu_j}{\sum_i \mu_i} \tag{2.14}$$

This is defined in other works as the fraction of applied current that is carried by a given ionic species[18], however these definitions should be equivalent given that the current density in an applied field is $nze\mu E$, where E is the strength of the electric field.

An accurate measure of t_{Li} combined with ionic conductivity measurements for a given electrolyte would be a better litmus test than conductivity alone for its potential for use in a Li-ion battery, however only conductivity is routinely reported for Li electrolytes. The reason for this lies in the simple fact that transference number is a difficult quantity to measure experimentally, and conductivity is relatively simple. This lack of information on transference numbers has been a known issue for decades[46], and unfortunately there has not been a huge effort in more recent years to gather transference number data, at least for non-aqueous systems. This attitude has started to change,

though, primarily since these transport parameters are required for physics-based models on Li-ion cells[68].

Several other models exist to describe the migration of ions in an electrolyte. Before much of the transport phenomena in electrolytes were better understood, scientists relied on empirical relations to guide their understanding of electrolyte systems. A particularly simple expression for conductivity as a function of salt concentration was found by Kohlrausch[46]

$$\Lambda = \Lambda^0 - A\sqrt{c_0} \tag{2.15}$$

where Λ is the molar conductivity, c_0 is the molar concentration of salt in the electrolyte, A is a parameter to be fit, and Λ^0 is the *limiting molar conductivity*. This quantity represents the molar conductivity of an electrolyte at infinite dilution; that is, it is the molar conductivity of a solution when a given ion experiences no ion-ion interactions and only interacts with the solvent medium. This quantity is determined by extrapolating back to zero concentration in Equation 2.15. Indeed, this expression has primarily been used to determine the limiting conductivity given the conductivity at non-zero salt concentration. It should be noted that this expression is only valid for very small concentrations, $\ll 1$ M. Therefore, this expression is not particularly useful in the study of electrolytes for batteries, which require high nominal salt concentrations. However, it is noted by Robinson and Stokes that a theory-based model of ion conduction in liquids should be able to recover Equation 2.15 in a limiting case[46]. Another important empirical relation for electrolyte transport properties is the Walden rule. This rule states that the limiting molar conductivity is related to the viscosity of the pure solvent by the following relation

$$\Lambda^0 \eta^0 = C \tag{2.16}$$

where C is a constant. For most systems, this expression holds for a variety of solvents for a given salt system. This equation strongly resembles the expression for molar conductivity derived from the Stokes' Law assumptions in Equation 2.12. Equation 2.16 has been used to estimate the limiting conductivities and mobilities of various ions when they cannot be measured directly[18]. As mentioned above, this relation has also been used to qualitatively investigate the ionicity of ionic liquids and non-aqueous electrolytes.

For many years, models of ion conduction in electrolyte solutions were limited to extremely diluted solutions. Below is a brief discussion of models that can describe the behavior of ions in concentrated solutions.

2.2.3   The Debye-Hückel model

The Debye-Hückel(-Osanger) treatment of electrolyte solutions combines an electrostatic description of the solution with a statistical mechanical treatment of the distribution of particles in solution. The starting point for this model is with the Poisson Equation to describe the Coulomb force on a given ion by all the surrounding ions[46]:

$$\nabla^2 \psi = -\frac{\rho}{\epsilon} \tag{2.17}$$

where ψ is the electric potential, ρ is the charge distribution, and ϵ is the dielectric constant of the solvent medium. The impact of the solvent composition on conductivity is only considered by its bulk dielectric constant. Another equation that is central to the Debye-Hückel model is the electroneutrality condition. This states simply that the charge of the solution is neutral overall, so the charges of individual ions must cancel out:

$$\sum_{i=1}^{n} n_i z_i = 0 \tag{2.18}$$

In Equation 2.18, n_i is the number density of species i, and z_i is the charge on species i. Now to solve the above problem, it is first assumed that the system possesses spherical symmetry. Next, a coordinate system is chosen such that the origin corresponds to the center of an ion. The consequence of this choice of coordinate system is that, by the electroneutrality condition, the total charge in the rest of the solution outside the chosen ion is simply the opposite charge of that ion. Mathematically, this consequence is stated as

$$\int_a^\infty 4\pi r^2 \rho \, \mathrm{d}r = -z_i e \tag{2.19}$$

where the subscript i corresponds to the ion chosen as the origin of the coordinate system, and a is the distance of closest approach to this central ion. The exact charge distribution ρ is found by knowing the probability of finding an ion a radial distance r away from the central ion. In the Debye-Hückel derivation, the Boltzmann distribution is used. Others have used different distribution functions for this derivation, but an evaluation of the merits of using different distribution functions is beyond the scope of this discussion.

Making some slight simplifications to the Boltzmann distribution to avoid violating the principle of superposition of fields in electrostatics, the electric potential for this system can be determined. It will not be stated here, but it is a relatively simple function of ϵ, r, z_i, a, n, and temperature T. From here, an expression for conductivity can be found by accounting for the effects of external fields on the ions in solution.

The model of Debye and Hückel accounts for two main phenomena when ions are added to the solvent medium[46]. The first is the *electrophoretic effect*. This effect accounts for the fact that when an ion travels through the liquid, whether due to an external electric

field or diffusion due to concentration gradients, it "drags" solvent molecules along with it. This will in turn impact how other migrating ions will travel through the medium, since the medium itself is no longer stationary, as would be the case in infinite dilution. The second effect described in the Debye-Hückel model is known as the *relaxation effect*. The idea here is that on average, the "ionic atmosphere" around a central ion is symmetric, and thus does not exert any net force on the ion. When the ion moves due to an external force, the atmosphere around the ion becomes asymmetric momentarily. The other ions in the solution will quickly rearrange and become symmetric once again, but not before exerting a small net force on the central ion. Taking these effects into account, the equation obtained for conductivity is identical to the empirical relation given in Equation 2.15 in the limit of very low concentration. Further, the Debye-Hückel model can also describe the conductivity of more concentrated electrolyte solutions. The Debye-Hückel model was the first serious attempt at theoretically describing the conductivity of electrolytes via ion interactions in solution and has proven to be quite accurate for many systems[46].

The Debye-Hückel model still has significant limitations, however. While it can be quite accurate for concentrations higher than the empirical relation discovered by Kohlrausch (Equation 2.15), it still cannot reach concentrations high enough for standard Li-ion battery electrolytes (~1 M) in most cases. For these concentrated solutions, more sophisticated models are required. One of the most popular, and the most relevant to this work is the model known as the Mean Spherical Approximation (MSA). This model has been developed as an extension of the Debye-Hückel model and can successfully model electrolytes at high enough concentrations to be relevant to Li-ion batteries. The main

difference in the MSA over the Debye-Hückel model is that it approximates ions in the solution as hard spheres rather than as point charges[69]. This theory has been well developed over the years by Blum and others[70-72]. The approaches used are similar to the Debye-Hückel model; statistical-mechanical particle distributions are used to compute the electrical potential from Poisson's equation, which is then used in turn to calculate the contributions of the electrophoretic effect and the relaxation effect on conductivity and other transport properties of electrolytes. Further, due to the non-zero size of the ions in the MSA, extended models of the MSA can model even more complex effects such as ion association, which will be described briefly below. This MSA approach to modelling transport phenomena is the basis for the Advanced Electrolyte Model, which is used throughout this thesis. A more formal introduction to the Advanced Electrolyte Model (AEM) is given later in this Chapter.

2.2.4   Ion association

Ion association refers to the phenomenon of free ions in an electrolyte solution colliding and combining to form new species. The most prominent of these new species are ion pairs, neutral (at least for a 1:1 electrolyte) "molecules" that act analogously to molecular dipoles. While ion pairs are the most common, there is also evidence to suggest that higher order ionic structures can be formed, such as triple ions, and ionic aggregates[73].

The formation of ion pairs and other structures in the electrolyte will have obvious consequences for the transport properties of these solutions. If an ion pair is formed, this essentially removes one positive ion and one negative ion from solution, reducing the total number of charge carriers, thus lowering the total ionic conductivity of the solution. Removing ions from the solution will also affect the ionic atmosphere, and

thus impact how conductivity is impacted by the electrophoretic and relaxation effects, mentioned above. Further, ion pairs essentially act as dipoles in the electrolyte. A significant population of ion pairs in solution will affect the dielectric properties of the medium in which the ions travel. As will be seen later in this thesis, this is particularly notable in systems containing low-dielectric solvents.

The phenomenon of ion association can be modeled relatively simply. However, Robinson and Stokes as well as Marcus and Hefter note that defining strict conditions for the formation of an ion pair are almost always subjective in nature[46,73]. This is because an associated ion pair and separated ions that interact with each other electrostatically are hard to differentiate in practice. There are still some general guidelines, however, that can be used to discuss ion association. The first is what is known as "Bjerrum's treatment"[46,73] and gives the value for a critical distance r_c between two ions of opposite charge below which an ion pair will be formed:

$$r_c = \frac{|z_1 z_2| e^2}{2 \epsilon k_B T} \tag{2.20}$$

In Equation 2.20, $z_1 e$ and $z_2 e$ are the charges on ions 1 and 2, respectively, ϵ is the dielectric constant of the medium (the solvent system), k_B is Boltzmann's constant, and T is the temperature of the system. For a 1:1 electrolyte, $|z_1| = |z_2| = 1$, and Equation 2.20 can be simplified somewhat. This critical distance is essentially the distance at which the electrical potential energy between the two ions, $|z_1 z_2| e^2 / \epsilon r$, is equal to twice the thermal energy of the system, $2 k_B T$. At this critical distance, the electrostatic energy between the two ions is large enough that the ion pair will not be disrupted by the thermal motion of particles in the solution. This critical distance postulated by Bjerrum is essentially a rule of thumb for when to consider a pair of ions to be "associated".

Since free ions in the electrolyte solution are solvated by solvent molecules, to go from free single ions (SIs) to associated contact ion pairs (CIPs) is a multi-step process. First, the free ions form solvent-separated ion pairs (SSIPs). In this structure, the ions are "associated" according to the Bjerrum definition, however they are still separated in space by more than one layer of solvating molecules. Next, solvent-shared ion pairs (SShIPs) are formed. These are like the SSIP described above, but with only one molecular layer of solvent between the associated ions. Finally, the ions form a CIP, but still note that the ion pair will still be solvated.

A good illustration of the various intermediate states between free ions and CIPs is shown in Figure 2.2, reproduced from Marcus and Hefter[73]. It should be noted that the pictures in Figure 2.2 may not necessarily reflect reality for a carbonate-based Li electrolyte. Using 1 mol/kg $LiPF_6$ in EC:DMC 30:70 (w/w) as a model system. The molar ratio of solvent molecules to salt is roughly 10:1. However, it is generally understood that low-dielectric solvents such as DMC do not participate in solvation[74]. If it is assumed that only EC is solvated to the Li ion and its counter ion, the ratio of EC to Li salt becomes roughly 3:1. Therefore, the number of solvating molecules pictured in Figure 2.2 is not feasible given the number of solvent molecules available in the Li electrolyte system. This Figure is simply meant to illustrate the various stages involved in the formation of a contact ion pair. The transitions to and from these intermediate structures are represented as equilibrium equations each with their own respective equilibrium constants. However, if one ignores the intermediate transitions and considers a simpler picture of ion association

$$C^+ + A^- \overset{K_A}{\leftrightarrow} C^+A^- \tag{2.21}$$

Then the "association constant" K_A can be calculated as

$$K_A = \frac{1 - \alpha}{\alpha} \qquad (2.22)$$

Where α is the fraction of free ions, and $1 - \alpha$ is the fraction of associated ions. Similar methods can be used to describe the formation of triple ions, quadruple ions, and higher order ionic structures, but this will not be discussed here.
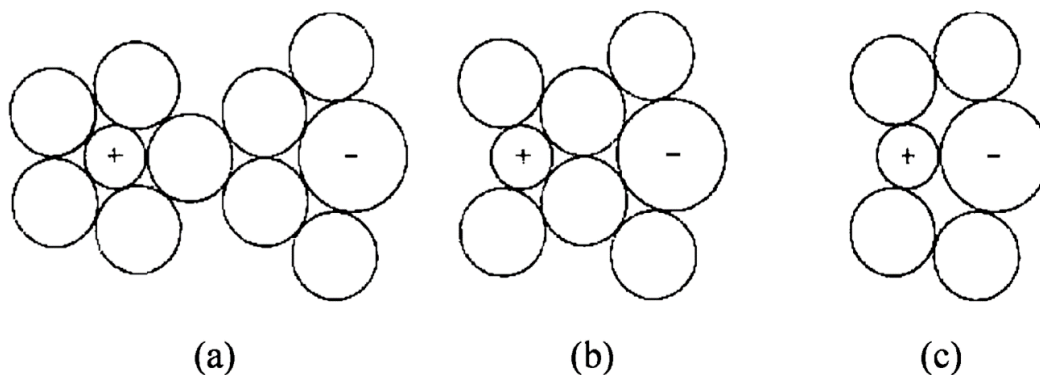
Figure 2.2: A simplified picture illustrating the differences between (a) solvent separated ion pairs (SSIP), (b) solvent-shared ion pairs (SShIP), and (c) contact ion pairs (CIP). Empty spheres represent solvent molecules. Reproduced from Ref. 73.

2.3 THE ADVANCED ELECTROLYTE MODEL (AEM)

The Advanced Electrolyte Model (AEM) is a theoretical model for electrolyte properties based on a statistical mechanics framework developed by Gering[8,10]. It uses a variety of molecular-scale interactions (solvent-solvent, solvent-ion, ion-ion) to calculate several macroscopic transport properties of electrolytes including, but not limited to: conductivity, viscosity, diffusion coefficients, transference numbers, and activity coefficients. The model can also predict microscopic properties of electrolyte systems, such as solvated ion sizes, solvation numbers, solvent residence times, and populations of different species such as single ions (SI), ion pairs (IP), and triple ions (TI). The AEM

can consider both aqueous and non-aqueous systems, many different solvents and Li salts. All electrolyte systems supported by the AEM are governed by the same set of equations. The AEM has previously been validated for several aqueous and non-aqueous systems[8,10]. One of the aims of this thesis will be to validate the AEM for a broader range of electrolyte systems. The AEM is a proprietary and non-freeware software package, however a limited number of peer-reviewed articles have been published regarding how the model calculates electrolyte transport properties[8-10]. Below, a short introduction will be given to how the AEM treats molecular-scale interactions in electrolyte solutions, and how the ionic conductivity and viscosity of the electrolyte are calculated from these interactions.

The AEM is based on an MSA framework, which was introduced above. More specifically, it uses an extension of this theory known as the non-primitive, non-restricted associative form of the mean spherical approximation (NPNRAMSA). This extended model allows for ion association as well as support for non-primitive salts (unequal cation and anion sizes).

2.3.1   Viscosity

The viscosity and conductivity of an electrolyte are intimately related quantities, as has been seen above in the Stokes' Law model of conductivity. The AEM uses its calculation of viscosity in determining conductivity; for this reason, the calculations for viscosity will be discussed first.

The AEM supports calculations for electrolytes containing up to five unique solvents. Therefore, the model must first be able to calculate the salt-free viscosity of

mixed solvents; the influence of ions is considered later. The mixing rule is given by the following equation

$$\eta_{mix}^0 = e^{\left[y_1 \ln \eta_1^0 + y_2 \ln \eta_2^0 + y_1 y_2 a (1+2y_1 b)(1+2y_2 c)\left(\frac{T_r}{T}\right)^5\right]}$$
(2.23)

where η_{mix}^0 is the mixed solvent viscosity at infinite dilution (salt-free), η_1^0 and η_2^0, and y_1 and y_2 are the salt free viscosities and mole fractions of solvents 1 and 2, respectively, $a, b,$ and c are free parameters related to non-ideal solvent mixing, and T is the temperature. Gering notes that this a "semi-empirical" equation, but full theoretical rigour would introduce unnecessary computational complexity and is not required at this stage.

Notice above in Equation 2.23 that there are only terms for two solvents, while the AEM supports up to five. To accommodate more than 2 solvents, an additional mixing rule is used, where the second solvent η_2^0 is approximated as a "pseudo-solvent" which captures solvents 2 through 5

$$\eta_2^0 \approx \eta_{PS}^0 = e^{\left[y_2' \ln \eta_2^0 + y_3' \ln \eta_3^0 + \cdots + y_n' \ln \eta_n^0\right]}$$
(2.24)

Once the salt-free viscosity η_{mix}^0 has been calculated, the various impacts of ions on the solution viscosity can be considered. The different interactions that must be considered when adding charged ions can be organized into two main categories: solvent-ion interactions, and ion-ion interactions. Solvent-ion interactions include ion solvation phenomena, and ion-ion interactions capture various electrostatic interactions between the ions in solution. The latter class of interactions includes ion association, which will be a prominent topic in this thesis, and has been introduced above.

It will be valuable to discuss how ion solvation is handled by the AEM. There are several different "ion sizes" that are considered in the AEM. Figure 2.3 shows an illustration of the various ion sizes that are defined by Gering in Reference 8. Also shown

in Figure 2.3 is the impact of surface charge density on the various solvation diameters. An ion with a high charge density such as Li^+ has a much larger solvation sphere compared to a relatively low-charge density ion like K^+. The simplest ion size is the diameter in the bare ion. This does not consider any solvent-ion effects and is obtained from crystallographic data. The next quantity is the hard sphere (HS) diameter. This is also known as the "collision diameter" and is essentially the largest size where a solvated ion is considered to be a hard sphere regarding collisions between other ions and solvent molecules. The most important solvation quantity in the discussion of electrolyte transport properties is the "effective solvated diameter", which can be thought of as analogous to the Stokes radius of an ion as discussed above. Finally, the "thawed" solvent diameter accounts for solvent molecules outside the primary solvation shell that still interact with the ion.
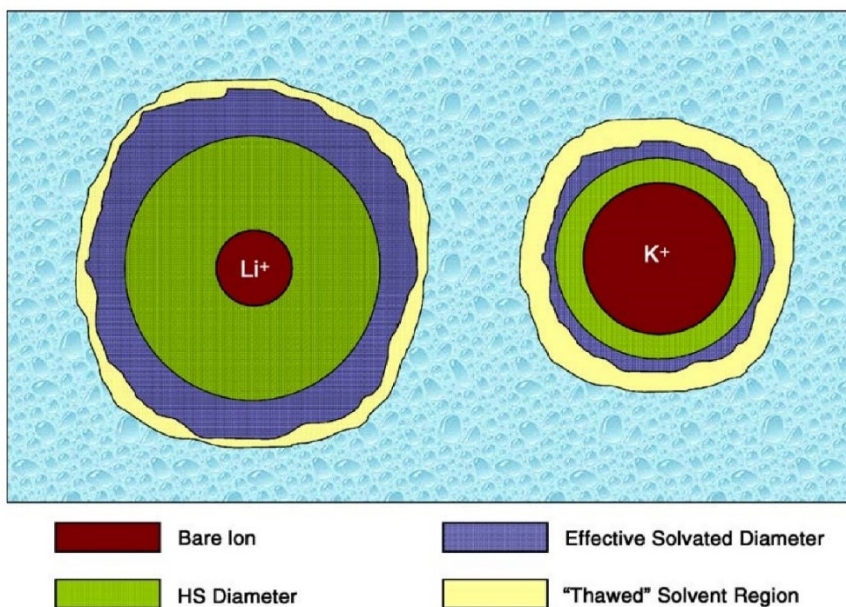
Figure 2.3: Illustration of the various ion diameters considered in the AEM. They are shown for two types of positive ions with different charge densities. Figure reproduced from Reference 8.

In addition to the solvated ion diameters discussed above, the AEM also computes the average solvent residence time, denoted τ_j in Ref. 8. This is the average amount of time that a given solvent molecule stays "solvated" or highly associated to a given ion. This is essentially a measure of the frequency that solvent molecules are replaced in the solvation shell of an ion. The AEM also calculates other solvation quantities such as the solvation number, which is the average number of solvent molecules attached to an ion. For the exemplary system of 1 m LiPF$_6$ in EC:DMC 30:70 (w/w) at room temperature (20°C), the AEM calculates an average solvation number of 3.745 for the Li$^+$ cation, and 1.632 for the PF$_6^-$ anion.

Mathematically, the AEM accounts for these various interactions with four distinct functions. The expression for the viscosity of a concentrated electrolyte solution used by Gering in the AEM is the following

$$\eta = \eta_{mix}^0\left(1 + f_{pos,\eta} - f_{neg,\eta} + f_{coul,\eta}\right)f_{DS} \tag{2.25}$$

$f_{pos,\eta}$ accounts for effects that increase the overall structure of the solution, which thus increase the viscosity. Conversely, $f_{neg,\eta}$ considers structure-breaking effects which correspondingly decreases the solution viscosity. $f_{coul,\eta}$ accounts for electrostatic (coulombic) interactions between ions that contribute to the viscosity. The expression given in Ref. 8 for $f_{coul,\eta}$ gives the net attraction (or repulsion) between the ions in the electrolyte. The expression for solution viscosity in Equation 2.25 is modulated by a factor of f_{DS}. This function considers "dipole stiffening", when the movement of solvent molecules become restricted due to electric fields from added ionic species. As may be expected, this effect becomes more pronounced as the salt concentration is increased. This phenomenon of dipole stiffening leads to an increase in viscosity.

Each of the above corrections to the infinite dilution viscosity on the addition of a solute have fairly involved functional forms that are presented in Ref. 8. However, they will not be presented here, as it would not be particularly instructive. It is sufficient to understand that in the AEM the effect of ions on the solution viscosity is handled by the various effects described above.

2.3.2   Conductivity

The approach that Gering takes to model conductivity is like what is done for viscosity. In addition to the phenomena that were considered to describe viscosity (ion solvation, ion association and other electrostatic effects), Gering also considers viscosity, counter ion (anion) transport, ionic hopping effects, and random motion effects. Again, like above, Gering starts with a simple model to describe ionic conductivity for the case with no ion-ion interactions (infinite dilution), and the above-mentioned effects modulate this basic theory. The starting point is an expression based on the Stokes' Law conductivity described earlier:

$$\lambda_j = \frac{2|z_j|}{\eta^0 \sigma_j^0} \left(\frac{0.82 \times 10^{-8}}{1 \times 10^{-10}} \right) \tag{2.26}$$

where λ_j is the equivalent mobility of ionic species j, η^0 is the viscosity of the solvent, z_j is the charge of ion j, and σ_j^0 is diameter of ion j. The extra factor of $\left(\frac{0.82 \times 10^{-8}}{1 \times 10^{-10}} \right) = 82$ is a unit conversion for the inputs of viscosity and ion size. Like in the model for viscosity, various ionic effects are captured in several different functions, and the expression for mobility when ionic effects are considered becomes an equation of the form:

$$\lambda_j = \{f_{solvent-ion\,j}, f_\alpha, f_{jk}^{Diff}, f_{random}, f_{hop}\} \times \left[82 \frac{2|z_j|}{\eta \sigma_j^{eff}} \right] \tag{2.27}$$

In Equation 2.27, η is the salt concentration-dependent solution viscosity calculated from Equation 2.25, and σ_j^{eff} refers to the effective solvated diameter of ion j (see Figure 2.3). The various ion interaction functions f_i will be discussed briefly below.

The AEM considers not just single ionic species, but also ion pairs (both contact ion pairs and solvent shared ion pairs), and triple ion species (both CAC^+ and ACA^-). Since ion pairs are neutral, they do not contribute directly to ionic conductivity. A net molar conductivity Λ can be computed for each of the single ion species and triple ion species:

$$\Lambda_{SI} = \sum_{j=i}^{n} \lambda_{j,SI} \tag{2.28}$$

$$\Lambda_{TI} = \sum_{j=i}^{n} \lambda_{j,TI} \tag{2.29}$$

where each λ_j is calculated from Equation 2.27. The overall ionic conductivity $\kappa = \Lambda c_0$, where c_0 is the molar concentration of salt added, is

$$\kappa = c_0[\Lambda_{SI} + \Lambda_{TI}] \tag{2.30}$$

Gering presents an explicit functional form for ionic conductance as an expansion of Equation 2.27, however this functional form is rather convoluted and not necessarily instructive. Instead, the individual functions f_i will be discussed.

$f_{solvent-ion}$ accounts for retarding effects between solvent and ion species at the molecular scale. Gering stresses that the interactions considered here are separate from the bulk viscosity of the solution, the influence of which is considered directly from the Stokes' law expression. This factor is also called "dielectric drag" and decreases in

strength as the salt concentration is increased, due to less available solvent molecules per ion. This effect is related to the electrophoretic effect described above. The next factor, f_α is just a measure of the population of ionic species. When single ions are being considered, f_α is the population of single ions. Similarly, when triple ions are being considered, f_α represents the population of triple ions.

f_{jk}^{Diff} considers obstruction of ion transport by counter-ion transport. The idea is that the presence of (solvated) counter-ions in the electrolyte solution creates a volume in the solution that is essentially "blocked", where the ion of interest cannot travel. This will act to decrease the conductivity in a similar way that higher tortuosity impedes ion transport in a porous electrode. Both the population of ions and the effective volume that they occupy will affect the extent that this factor impacts the ionic conductivity.

f_{random} accounts for the random motion of ions. Collisions due to this random motion will have a non-zero impact on ionic conductivity. Clearly this effect will be more pronounced at higher temperatures, where more collisions will occur. The HS diameters of the solvated ions will also impact this random motion. Finally, f_{hop} captures the phenomenon of ion hopping. Gering defines this as the transport of an ion in "its minimally solvated state". Clearly, an ion in this state will have a higher mobility than a solvated ion. f_{hop} simply gives the probability of finding an ion in this non-solvated state. Using all these various contributions, the AEM can calculate conductivity for a vast range of electrolyte systems, at various temperatures and salt concentrations using a model that takes many more effects into account than the simple Stokes' Law conductivity. These calculations for viscosity and conductivity will be validated with experimental measurements for several electrolyte systems in the coming chapters.

CHAPTER 3 EXPERIMENTAL METHODS

The setups for measuring conductivity and viscosity described in this chapter were developed primarily by Dr. Luc Beaulieu. The author of this thesis assisted in the commissioning and initial testing of these systems.

All electrolyte mixing was done in an Ar-filled glove box to avoid contamination from the air. The different solvents, additives, and Li salts used in this thesis are summarized in Table 3.1 In some cases, blends of different solvents were received directly from the supplier. These cases are recorded as separate entries in Table 3.1. For each chemical used, the purity and water content were quoted from the supplier, when available.

Compound	Supplier	Purity (%)	Water content
ethylene carbonate (EC)	BASF	99.95	< 10 ppm
ethyl methyl carbonate (EMC)	BASF	99.92	< 6 ppm
dimethyl carbonate (DMC)	BASF	99.95	< 20 ppm
fluoroethylene carbonate (FEC)	BASF	99.94	
methyl acetate (MA)	BASF	> 99.95	< 20 ppm
ethyl acetate (EA)	BASF	99.99	19.4 ppm
methyl propionate (MP)	BASF	99.9	19.9 ppm
methyl butyrate (MB)	BASF	99.8	18.1 ppm
lithium hexafluorophosphate (LiPF6)	BASF	99.94	14 ppm
EC:EMC:DMC 25:5:70 (v/v)	BASF		19.7 ppm
propionitrile (PN)	Sigma-Aldrich	> 99.7	
isobutyronitrile (iBN)	Sigma-Aldrich	99	
methyl formate (MF)	Sigma-Aldrich	99.8	< 50 ppm
ethyl formate (EF)	Acros Organics	> 98	< 0.1%
propyl formate (PF)	Alfa	97	
isobutylformate (iBF)	Sigma-Aldrich	97	
isobutylacetate (iBA)	Sigma-Aldrich	99	

Table 3.1: The various chemicals used in this thesis, along with the suppliers used and their purity.

3.1 TRANSPORT PROPERTY MEASUREMENTS

3.1.1 Conductivity measurements

The conductivity setup used in this thesis was developed by Luc Beaulieu (Memorial University). Ionic conductivity was measured using four identical commercial conductivity meters (Hach model 3455). These conductivity probes measured conductivity by a 2-electrode measurement. A small AC voltage is applied across the electrodes, causing an ionic current to flow in the solution, which is then converted to a resistance by Ohm's Law. The conductance is then found by taking the reciprocal of the resistance. To convert from conductance to conductivity (also called specific conductance), the measured conductance is multiplied by a *cell constant*, which is a function of both the distance between electrodes and the geometry of the conductivity cell.

Probes were calibrated in air and to a known standard (12.88 mS/cm, Hanna Instruments HI70030C) to determine the cell constant. The determination of the cell constant and the conversion to from measured current to conductivity was done automatically by the controller unit (Hach SC1000 controller). Measurement accuracy quoted by the supplier to be ±2% of the measured conductivity value, which was confirmed in the lab. 14.5 mL of electrolyte was added to a custom-made stainless-steel holder under a fume hood. The probe was then sealed to the holder by an O-ring to eliminate electrolyte-air contact. The seal was maintained by using custom-made stainless-steel clamps. Sealed sensors were then placed in a temperature-controlled bath (VWR Scientific model 1151) filled with ethylene glycol. The temperature of the bath was varied between 0°C and 40°C in increments of either 5°C or 10°C. The temperature

of the bath was verified in this range using an external thermocouple thermometer (Omega HH802U), found to be accurate to ±0.5°C between 0.0°C and 100.0°C. At each step, the electrolyte was allowed to equilibrate with the temperature of the bath for at least 40 minutes. Conductivity measurements were recorded by the system every 5 seconds. Figure 3.1(a) shows an example of the raw conductivity data collected by the system for an electrolyte composed of 1.2 mol/kg $LiPF_6$ in EC:EMC:DMC 25:5:70 (v/v). Once the conductivity settles as the system reaches thermal equilibrium the "final" conductivity measurement is recorded before the temperature is changed, specified by the solid symbols in Figure 3.1(a). Figure 3.1(b) shows these points plotted as a function of temperature.
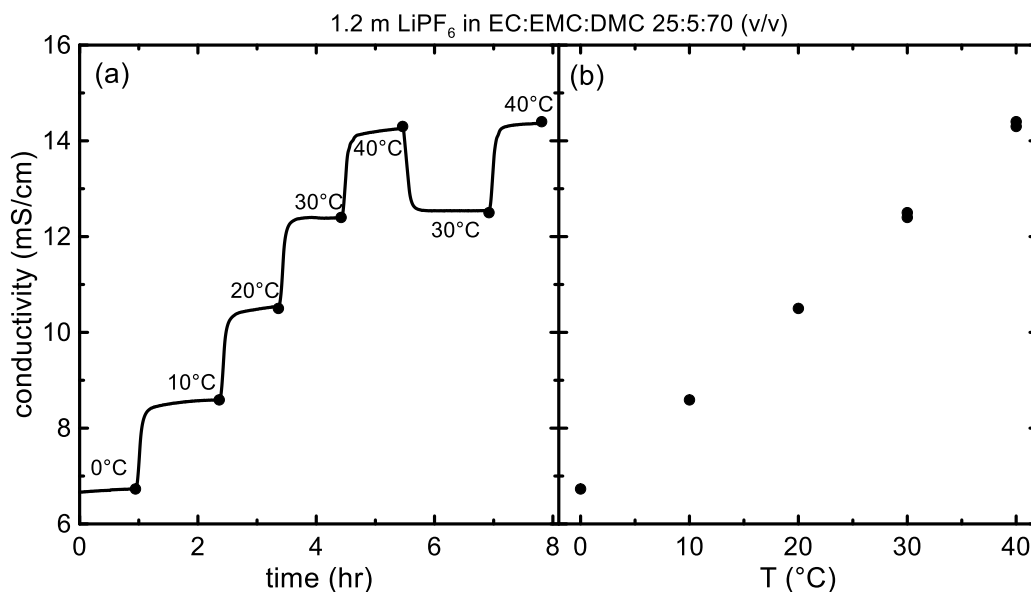
Figure 3.1: (a) Raw data collected by the conductivity probe at different temperatures, labeled below. The solid symbols are the conductivity values recorded after system reached thermal equilibrium. (b) The same points in panel (a) plotted as a function of temperature.

3.1.2   Viscosity

Electrolyte viscosity was measured using an Ostwald viscometer. An Ostwald viscometer is a U-tube type viscometer that consists of a large reservoir bulb, a narrow capillary, and a smaller bulb where the measurement takes place. Figure 3.2 shows the main features of an Ostwald viscometer. To make a measurement of viscosity, the fluid was forced through the capillary and into the measurement bulb. Once the fluid reached the top of the measurement bulb, it was allowed to fall under its own weight back through the bulb. The time taken for the fluid to travel between the top and bottom of the bulb was used to find the viscosity of the solution, given by

$$\eta_s = \eta_{ref} \frac{\rho_s t_s}{\rho_{ref} t_{ref}} \tag{3.1}$$

where η_s, ρ_s, and t_s are the dynamic viscosity, density, and time taken for the fluid to travel through the bulb, respectively, for the sample in question. η_{ref}, ρ_{ref}, and t_{ref} are the viscosity, density, and time to travel the bulb, respectively, for the reference sample. For all measurements in this thesis, deionized water was used as a reference sample.
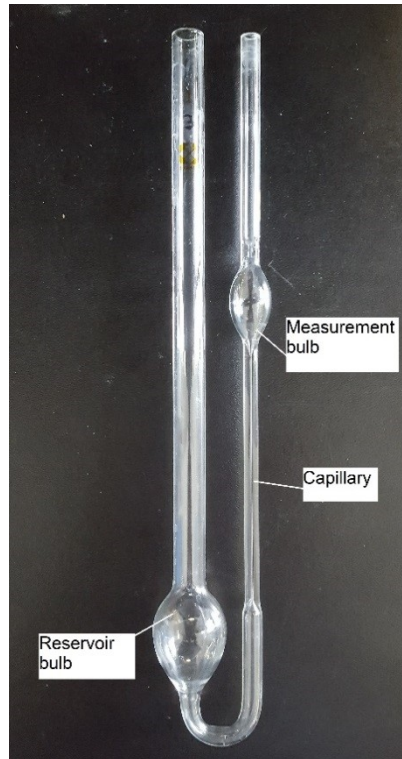
Figure 3.2: A photograph of an Ostwald viscometer used for the viscosity measurements. The key components of the device are labelled.

A computer-controlled system was developed by Beaulieu to automatically measure t_s as a function of temperature (T). Figure 3.3 shows a schematic of the experimental setup. In this setup, the temperature of the electrolyte in the viscometer was controlled by a circulating bath (Thermo Scientific) filled with a water/ethylene glycol mixture (Fisher Bioreagents). The viscometer was placed inside a triple walled glass Dewar where the mixture was circulated to control the temperature of the viscometer. Two different sized viscometers were used in these experiments, with capillary diameters of 0.5 mm and 0.75 mm, respectively (Sibata Scientific Technology, Japan). A platinum four-wire resistive thermal device (RTD, Digi-Key, USA) was attached to the outside of the measurement bulb of the viscometer during measurement, and thermal contact was maintained by adhering the RTD to the glass surface using thermal paste (Wakefield Engineering, Beverly, MA, USA). The RTD was monitored using a Keithley 2000 multimeter, which was then connected to the controlling computer, as illustrated in Figure 3.3.

A webcam positioned in front of the measurement bulb was used to monitor the position of the liquid as it fell through the bulb. Figures 3.4(a), (b), and (c) show snapshots of the liquid meniscus at different positions in the bulb. Figures 3.4(d), (e), and (f) show the images from Figures 3.4(a), (b), and (c), respectively, after the images were processed. When the meniscus reached the bottom of the bulb, marked point "B" in Figure 3.4, the liquid was forced back up through the capillary until it passed point "A". This was done by using a USB relay that triggers a 3-way solenoidal valve connected to a source of compressed air. This process continued for the range of temperatures of interest.
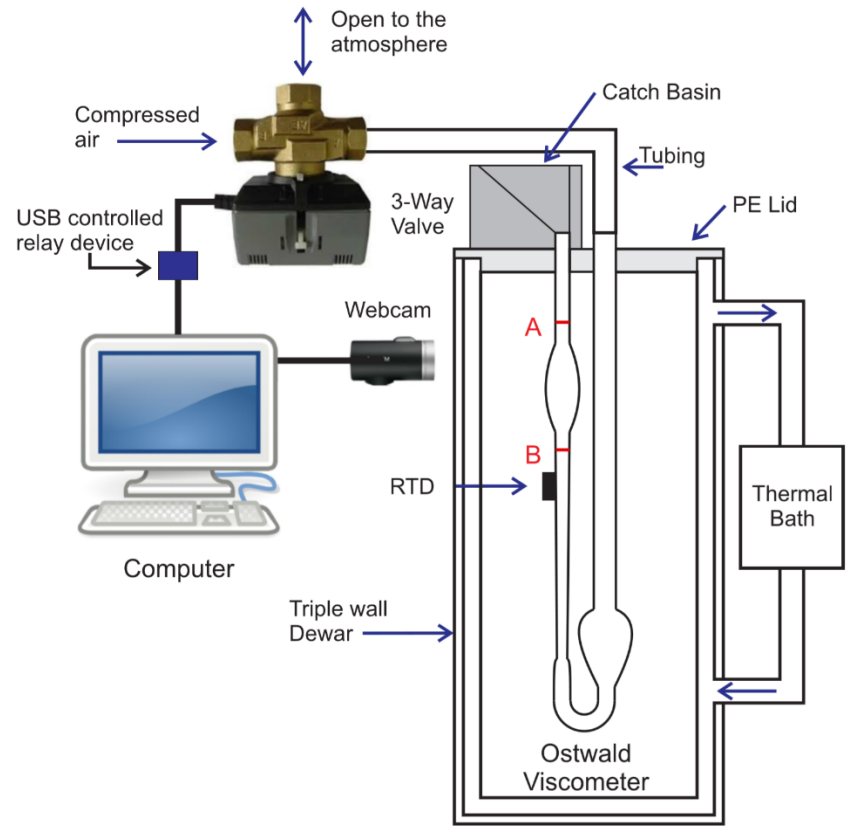
Figure 3.3: A schematic diagram of the viscosity apparatus.
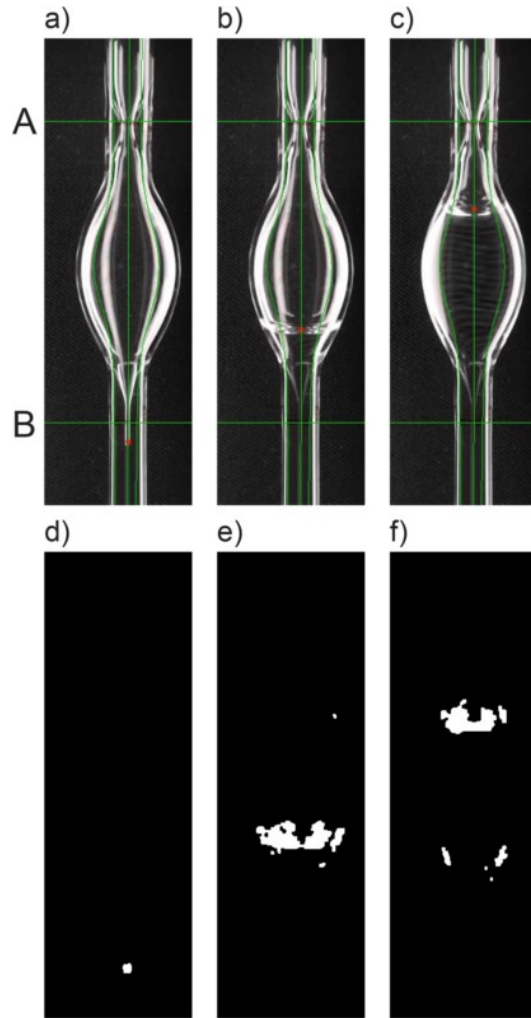
Figure 3.4: (a)-(c) Images of the viscometer's measurement bulb as a fluid travels through it. The lines that bound the convex hull searching procedure as well as the endpoints A and B are superimposed as green lines. The calculated position of the meniscus is given as a red dot. (d)-(f) The final binary images after processing corresponding to the images in (a), (b), and (c), respectively.

To interpret the images of the meniscus taken by the webcam and to time the travel of the liquid through the viscometer bulb, an analysis software was developed using VB.net. This software used packages and procedures typical of computer vision software[75-80]. The goal of the image processing was to isolate an image of the meniscus of the liquid, thus allowing for the position of the liquid in the bulb to be tracked. First, two

images of the viscometer bulb were taken after a pre-set delay. The delay between frames was different depending on the liquid's position: if the liquid was near the middle of the bulb, there was a larger delay between frames, but if the liquid was close to either endpoint of the bulb the frame delay was very short. Additionally, the user was required to adjust the frame delay depending on the viscosity of the electrolyte being tested. For a very viscous solution, the frame delay would have to be increased significantly from the default setting to allow for the meniscus to move enough for the image subtraction process to work correctly. After two adequate frames were taken, the images were converted to grayscale.

Next, a Gaussian blurring algorithm was performed on the grayscale images. This step was optional, however it was useful to remove small signals unrelated to the meniscus in the images. After the Gaussian blurring step, the grayscale images were subtracted from each other. Ideally, the only difference between the two images should be the meniscus, since it is the only feature that moves continuously. However, there were always some impurities in the images, which may include but are not limited to air bubbles or dirt particles in the ethylene glycol, or changes in lighting conditions between frames. To amplify the image of the meniscus and suppress less important features that may have shown up in the difference image, the image was converted to a binary image. A threshold pixel value was chosen, and any pixel with a value less than this threshold was set to 0 (black), and any pixel above the threshold was set to 1 (white). This operation suppressed any non-meniscus features and made the remaining image processing steps easier. From here, dilation and erosion operations were performed on the binary image. A dilation operation adds white pixels to regions of a binary image where

white pixels are found according to a searching algorithm. Effectively, the dilation algorithm increases the size of features in the binary image. This operation can introduce noise to the image, however, so the erosion operation is applied to remove this noise.

After the binary image was created and tweaked by the dilation and erosion, convex hulls and contours were identified in the image. In general, a convex hull is the smallest possible convex polygon that completely encloses a set of 2D points. In the case of the binary image, the set of points were the white pixels in the image. Contours are simply curves that define the boundary of convex hulls. These objects were found in the images using known algorithms[79,80]. Once the convex hulls were found, their positions along the axis of the viscometer were determined. Finally, the average positions of the various convex hulls defined the position of the meniscus.

Some additional constraints are placed on the binary image during the analysis. The shape of the viscometer was modelled by the sum of a straight line and a Gaussian function:

$$y(x) = Ae^{-\frac{(x-x_0)^2}{c^2}} + mx + b \tag{3.2}$$

where A, x_0, c, m, and b are parameters that were determined by the user before the start of the experiment. Two separate Gaussian functions were used to define the top and bottom of the meniscus, respectively. An additional linear function was used to define the centre axis of the viscometer. Figures 3.4(a), (b), and (c) show these lines superimposed over the viscometer along with the endpoints A and B. The red dot in each of Figures 3.4(a), (b), and (c) is the calculated position of the meniscus along the axis, described above. When the convex hulls were found, any convex hull that lay outside of these boundaries was discarded from further analysis. Figures 3.3(d), (e), and (f) show the final

processed binary images after all convex hulls were found. This procedure was repeated for each subsequent frame, tracking the meniscus as it traveled up and down the viscometer bulb. When the liquid passed the lower endpoint of the viscometer bulb (marked "B" in Figure 3.4), the solenoid valve was opened to compressed air, and the electrolyte was pushed back up. When it reached the top (point "A" in Fig. 3.4), the solenoid valve was triggered again, opening the valve to atmospheric pressure, allowing the solution to fall again.

At each frame, the system took a temperature measurement from the RTD in addition to the position measurement. As well, the time elapsed since the fluid passed through point A (Fig. 3.4) was recorded. Figure 3.5(a) shows the position of the meniscus for a sample of deionized water (where point A in Figure 3.4 is taken to be $x = 0$ cm) as a function of time elapsed, as the temperature went from high (40.7°C) to low (6.8°C). For decreasing temperature, the viscosity of the water increases, meaning the time taken to fall through the viscometer bulb increased (see Eq. 3.1), which can be seen clearly in Figure 3.5(a). For a single cycle, the temperatures recorded at each of the data points going from positions A to B were averaged. Figure 3.5(b) shows the time taken to travel the length of the viscometer bulb as a function of this average temperature.

To convert this time value to dynamic viscosity, a modified version of Equation 3.1 was used. The reference sample used for all measurements was this thesis is deionized water. From Equation 3.1, a proportionality factor is defined

$$\alpha = \eta_{\mathrm{ref}}/t_{\mathrm{ref}} \tag{3.3}$$

which is the ratio of the viscosity of water to the time taken for water to travel to point A to point B for a given viscometer at a given temperature. The known viscosity of water

was obtained from an empirical temperature-dependent equation so that α could be determined[81]. From here, Equation 3.1 becomes

$$\eta_s = \alpha \frac{\rho_s t_s}{\rho_{\text{ref}}} \tag{3.4}$$

To find the viscosity of the sample, a known empirical relation for the density of water (ρ_{ref}) was used[82]. This procedure was carried out to calibrate each viscometer separately. Since the data as-collected was a function of average temperature, the data for a viscosity experiment may not fall on "nice" temperature values (e.g. 0°C, 5°C, 10°C, etc.). Figure 3.6 shows a set of viscosity points as-collected for water. To plot viscosity versus different independent variables (e.g. Li salt concentration, solvent compositions), temperature values used must be standardized between different samples. To allow for constant temperature comparisons, viscosity data was interpolated to temperatures between 5 and 50°C, in steps of 5°C. This was achieved using a linear interpolation procedure in MATLAB. If the data did not reach the boundaries of the interpolation routine (i.e. data was not collected down to 5°C or up to 50°C), a linear extrapolation was performed to these temperatures, again using MATLAB. The quality of extrapolated data points could not be confirmed, so this case was avoided if possible. Interpolated data points for the water sample mentioned above are shown superimposed over the non-interpolated data in Figure 3.6. The total uncertainty after the interpolation has been applied is about 2%.
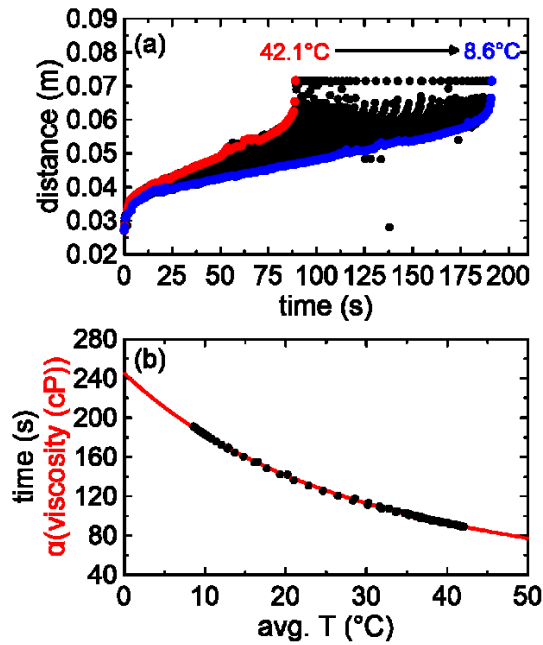
Figure 3.5: (a) Raw data for deionized water as collected from the viscosity setup showing position of the meniscus vs time. (b) Total time (i.e. time taken for the meniscus to travel the full length of the bulb) vs average temperature for the data shown in (a). The solid red line is the empirical relation for viscosity multiplied by the calibration constant determined for the given viscometer used here.
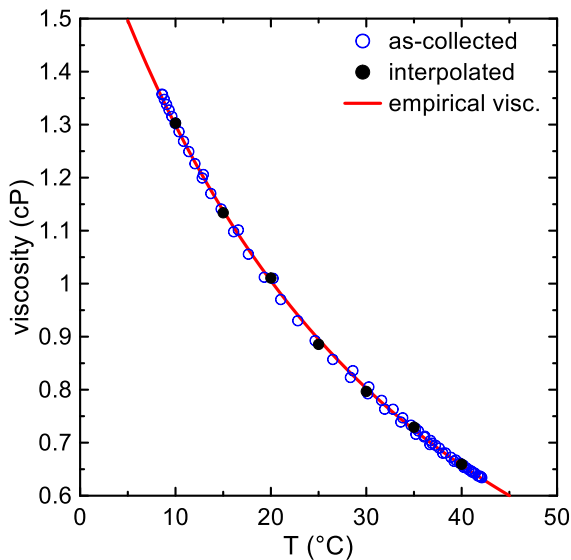
Figure 3.6: Viscosity plotted as a function of temperature for de-ionized water. The open symbols show the viscosity data as-collected. The solid symbols show the interpolated viscosity data, and the red solid line is calculated from the empirical relation for water viscosity.

The volume of liquid used for the viscosity measurement had a small impact on the result of the measurement. Using a volume 50% above the nominal volume led to a deviation of 8.9 ± 0.8 % from the known value for viscosity, while a 50% lower volume gave a 5.3 ± 0.4 % deviation. To eliminate this error, a device was constructed to ensure that a controlled volume of fluid was delivered for every trial. This device is pictured in Figure 3.7. The volume of this device was 11.00 ± 0.03 mL. The exact volume used here is not the significant feature, rather that the same volume of fluid is used for every measurement.

Figure 3.7: A device to deliver a constant volume of fluid to the viscometer. The volume between the two stopcocks is 11.00 ± 0.03 mL.

3.1.3 Electrolyte blends for transport property measurements

In Chapters 4 and 5, results for the viscosity and conductivity of several electrolytes will be presented. Many different solvents are considered in this thesis, which are summarized in Table 4.1. These electrolytes fall into three main classes of solvent blends:

1. (100-x)% [EC:EMC:DMC 25:5:70 (v/v)] + x% A, where A = {MA, EA, MP, MF, EF, PF, iBF, iBA, PN, iBN}, and x = {0, 5, 20, 40, 60} (wt. %) (Chapter 4).

2. EC:EMC:MA and EC:DMC:MA 30:(70-x):x, where x = {0, 10, 20, 30} (wt. %). (Chapter 4).

3. EC:EMC and EC:DMC x:(100-x) (wt. %) (Chapter 5).

For all combinations of solvents described above, the conducting salt used was LiPF$_6$. The benefits of using this salt over other candidates have been discussed in Chapter 2. Concentrations in the range of 0 to 2 mol/kg solvent (molal concentration, denoted m from here onward) have been used for all solvent blends.

3.2 POUCH CELL CYCLING

The cells used for cycling tests were Li[Ni$_{0.4}$Mn$_{0.4}$Co$_{0.2}$]O$_2$ (NMC 442)/graphite and single crystal Li[Ni$_{0.5}$Mn$_{0.3}$Co$_{0.2}$]O$_2$ (NMC 532)/graphite 402035-size wound prismatic pouch cells. These cells were obtained from LiFun Technology (Xinma Industry Zone, Golden Dragon Road, Tianyuan District, Zhuzhou City, Hunan Province, PRC, 412000). Detailed information about electrode materials can be found in Refs. 45 and 83. Pouch cells were obtained without electrolyte and were vacuum sealed for shipment.

Before use in our laboratory, they were cut open and dried at approximately 100°C for 14 hours under vacuum to remove any excess moisture. After drying, cells were moved to an Ar-filled glovebox for filling. Cells were filled with 0.9 g of electrolyte and sealed by a vacuum sealer (MSK-115V, MTI Corp.) to -95.2 kPa gauge for 4 seconds at 165°C. A summary of the different electrolyte formulations used for cell cycling in this thesis are summarized in Table 3.2. Cell types 1, 2, and 3 were cycled between 2.8 and 4.3 V at 20°C ± 1°C. These cells were charged at a rate of 1C (C/x corresponds to a current that will give a full charge in x hours) for 30 cycles, then 1.5C for 30 cycles, then 2C for 30 cycles. Between each step up in charge rate, the cells were cycled at C/5 for three cycles. For all cycles, cell types 1, 2, and 3, cells were discharged at a rate of 0.5C. Cell types 4, 5, 6, and 7 were cycled at 40°C ± 1°C. Cell types 4, 5, and 6 were cycled

between 2.8 and 4.4 V at a charge/discharge rate of C/2.5 in constant current- constant

voltage (CCCV) mode. The cutoff current for CCCV cycling was C/20. Cells of type 7

were cycled between 3.0 and 4.4 V at a rate of C/2 for both charge and discharge cycles.

A cycle at C/20 was done every 50 cycles. The cutoff current for cells of type 7 was also

C/20. All pouch cells were cycled with external clamps to ensure a firm stack pressure of

about 25 kPa even if gas was produced during cycling. For each cell type, two cells were

constructed to ensure reproducibility.

Number	Electrode chemistry	LiPF6 concentration	Solvent blend	Additive(s)
1	NMC 532/graphite	1.2 M	EC:EMC 30:70	2% FEC
2	NMC 532/graphite	1.2 M	EC:EMC 30:70 + 20% MA	2% FEC
3	NMC 532/graphite	1.2 M	EC:EMC 30:70 + 40% MA	2% FEC
4	NMC 442/graphite	1.0 M	EMC	-
5	NMC 442/graphite	1.0 M	EC:EMC 30:70	-
6	NMC 442/graphite	1.0 M	FEC:EMC 5:95	-
7	NMC 532/graphite	1.0 M	FEC:EMC 5:95	-

Table 3.2: Different cell chemistries and electrolyte solutions used for various cell cycling experiments in this thesis.

3.3 DIFFERENTIAL THERMAL ANALYSIS (DTA)

Differential thermal analysis (DTA) was used to do a preliminary investigation of the

phase equilibria of the ternary $EC:DMC:LiPF_6$ system. DTA is related to the method of

differential scanning calorimetry (DSC), a well-known thermal analysis technique. The

major drawback of DSC is that only very small amounts of sample can be used in a scan

(on the order of mg). The Li-ion DTA technique developed by Day et al.[84], on the other

hand, can measure full 402035-sized Li-ion pouch cells without affecting cell lifetime.

This allows thermal analysis techniques to be used non-destructively on full cells at

various stages in their cycle lives.

The general operating principle of the DTA technique is as follows. The setup requires two cells, a working cell and a reference cell. The reference cell is filled with a single solvent with a very low melting point. For all the measurements in this thesis, methyl acetate (MA, melting point -98°C) was used in the reference cell. The working cell contains the electrolyte of interest. In the cases where $LiPF_6$ was added, cells were held at 1.5 V to avoid dissolution of the copper current collector. During measurement, both cells were held in a cryostat and cooled with liquid nitrogen. The cryostat is cooled below the melting point of the working cell, which is typically no lower than -75°C for cells containing high concentrations of dimethyl carbonate (DMC). The cryostat is then held at this minimum temperature for at least 10 minutes to ensure the liquid-solid phase transition is complete in the working cell. The cells are then heated, using resistive tape controlled by a Lakeshore 340 temperature controller, at a set rate though the various phase transitions up to about +25°C.

Since the reference cell remains in its liquid phase through the whole temperature range, its temperature as a function of time should increase at a constant rate. The working cell, however, will have unique temperature features relating to the various phase transitions that occur on heating. The working cell will have an approximately constant temperature during a phase transition due to the enthalpy of fusion. Plotting the difference between the working cell temperature and the reference cell temperature $(T_{sample} - T_{ref})$ against T_{ref} will show distinct peaks during melting events. More information about the apparatus used for the DTA experiments can be found in Ref. 84. Analysis of the DTA data to find various liquidus and solidus transition temperatures followed the procedure outlined by Ding et al.[85]

For the DTA experiments, solvent blends EC:DMC x:(100-x), x = {0, 10, 20, 30} (wt. %) were used, and $LiPF_6$ concentrations 0 m and 1.0 m were considered. On the DTA apparatus, cells were cooled at a rate of 3°C/min to -100°C, and heated at 1°C/min to +25°C. In some cells, an exothermic feature was observed in the DTA trace before the solidus transition. In this case, cells were cooled to -100°C, heated to just beyond the exothermic peak, cooled, then heated to 25°C to remove this feature from the data. Cells were filled with 0.75 mL of solution in an Ar-filled glovebox using the same filling and sealing procedure as described above. Cells did not undergo formation prior to DTA measurements as formation can cause transesterification of linear carbonate species, affecting the composition of solvents in the electrolyte[84].

CHAPTER 4   NEW CO-SOLVENTS FOR CARBONATE-BASED ELECTROLYTE SYSTEMS

Some electrolyte solutions used in this chapter were prepared by Dr. David Hall, Erin Tonita, and Ahmed Eldesoky. Erin Tonita assisted with conductivity and viscosity measurements. Cell cycling data was provided by Dr. Jing Li. The author of this thesis performed all data analysis and interpretation.

4.1   INTRODUCTION

Typical performance metrics of Li-ion batteries such as lifetime and power capabilities depend strongly on the composition of the electrolyte used. The ionic conductivity of the electrolyte is one transport property that helps to determine how fast a cell can be charged or discharged, and has been reported for a vast number of aqueous and non-aqueous electrolyte systems[10,23,47-58]. While it does not give a full picture of ionic transport in an electrolyte (see Chapter 2), conductivity can be measured easily and accurately, giving a rapid evaluation of the electrolyte in question. As such, conductivity is the predominant transport property of electrolytes that is studied in the literature. In addition to conductivity, the dielectric constants and viscosities of the constituent solvents must be considered[50,86]. For a more rigorous analysis of cell performance using physics-based models, other transport properties such as Li-ion transference number, diffusivity, and activity coefficients are required[54,68,87-89].

Traditional solvent blends for Li electrolytes have been made with mixtures of ethylene carbonate (EC), ethyl methyl carbonate (EMC), diethyl carbonate (DEC) and dimethyl carbonate (DMC). EC has a high dielectric constant, which is necessary for the

disassociation of the constituent ions in the lithium salt. Traditionally, EC has also been required in the electrolyte to help form a passivating solid electrolyte interphase (SEI) on the graphite negative electrode[90]. DEC, EMC and DMC have lower viscosities and melting points than EC, and when mixed with EC result in an electrolyte with a good balance between desirable electrochemical properties, high dielectric constant, and low viscosity[6,20-22].
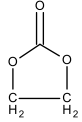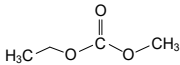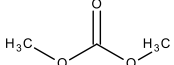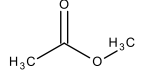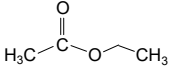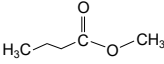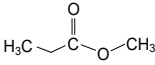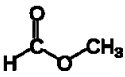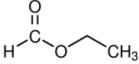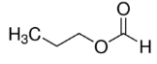
Aliphatic esters have lower melting points and viscosities than "low viscosity" linear carbonates such as EMC or DMC[6,18,30]. Many studies have investigated the impact of esters on the performance of Li-ion cells at low temperature when added as a co-solvent to traditional carbonate-based Li-ion electrolytes. Esters considered in previous studies include: methyl acetate (MA), ethyl acetate (EA), ethyl proprionate (EP), ethyl butyrate (EB), methyl proprionate (MP), methyl butyrate (MB), propyl butyrate (PB), and butyl butyrate (BB)[26,27,30,91-95].

In this chapter, the physical properties of several different electrolyte systems containing esters are measured. Additionally, two low viscosity nitriles, propionitrile (PN), and isobutyronitrile (iBN) are considered. Viscosity was measured for several solvents as a function of temperature and compared to typical "low viscosity" carbonate solvents EMC and DMC using the setup described in Chapter 3. Additionally, conductivities and viscosities were compared for Li electrolytes containing 80% (wt. %) linear carbonate mixture + 20% different co-solvents, again using the experimental setup outlined in Chapter 3. Finding MA to be the most promising ester, a large, systematic study of conductivity and viscosity for electrolytes containing MA was carried out. High rate cycling tests were done with $Li[Ni_{0.5}Mn_{0.3}Co_{0.2}]O_2$ (NMC 532)/artificial graphite

cells containing MA and fluoroethylene carbonate (FEC) in the electrolyte to investigate the rate capability of cells containing MA as a co-solvent. Results from conductivity and viscosity measurements are compared to calculations from the AEM, which has been introduced in Chapter 2.

4.2 VISCOSITY AND CONDUCTIVITY RESULTS

Table 4.1 shows some basic physical properties of the carbonate solvents EC, EMC, DMC, the ester solvents MA, EA, MB, MP, MF, EF, PF, iBF, and iBA, and the nitriles PN and iBN. The properties shown in Table 4.1 include melting point, boiling point, dielectric constant, chemical structure, and viscosity at room temperature (unless otherwise noted). Some of the advantages of adding esters or other co-solvents to a carbonate-based electrolyte should be immediately apparent. The melting points of the solvents considered in this study are lower than that of EC, EMC, and DMC, with the exception of iBA. The dielectric constants of these compounds are higher than the dielectric constants of EMC and DMC, which could marginally aid in salt dissociation in the electrolyte. The nitriles PN and iBN have much higher dielectric constants than both EMC or DMC ($\epsilon_{PN} = 29.7$ and $\epsilon_{iBN} = 24.42$ at room temperature). The viscosities of these compounds at room temperature are also lower than the carbonate solvents. The molecular dissimilarities between carbonate and ester solvents can also contribute to greater randomness and related structure-breaking in solution, thereby further decreasing mixture viscosity[8]. It may be assumed, then, that the addition of esters or nitriles to the electrolyte should then reduce the overall viscosity of the electrolyte.

Name	MP (°C)	BP (°C)	Dielectric constant at 25°C	Viscosity at 25°C (cP)	Structure
Ethylene carbonate (EC)	36.4[17]	248[17]	89.78 (40°C)[17]	1.93 (40°C)[17]	
Ethyl methyl carbonate (EMC)	-53[17]	110[17]	2.958[18]	0.65[18]	
Dimethyl carbonate (DMC)	4.6[18]	90[18]	3.1075[18]	0.59[18]	
Methyl acetate (MA)	-98[18]	57[18]	6.68[18]	0.40[30]	
Ethyl acetate (EA)	-84[35]	77[35]	6.00[ai]	0.46[30]	
Methyl butyrate (MB)	-85.8[35]	102.8[35]	5.48[35]	0.541[35]	
Methyl proprionate (MP)	-87.5[35]	79.8[35]	6.20[35]	0.431[35]	
Methyl formate (MF)	-99[36]	31.7[36]	9.2 (15°C)[36]	0.325[36]	
Ethyl formate (EF)	-79.6[36]	54.4[36]	8.57 (15°C)[36]	0.380[36]	
Propyl formate (PF)	-92.9[36]	80.9[36]	6.92 (30°C)[36]	0.485[36]	

Name	MP (°C)	BP (°C)	Dielectric constant at 25°C	Viscosity at 25°C (cP)	Structure
Isobutyl formate (iBF)	-95.8[36]	98.2[36]	6.41 (20°C)[36]		
Isobutyl acetate (iBA)	-98.8[36]	116.5[36]	5.068 (20°C)[36]	0.676[36]	
Propionitrile (PN)	-92.78[36]	97.14[36]	29.7[36]	0.294[36]	
Isobutyronitrile (iBN)	-71.5[36]	103.9[36]	24.42[36]		

Table 4.1: Melting points, boiling points and dynamic viscosities at 25°C (unless otherwise specified) for several carbonate, ester and nitrile solvents used in this chapter.

Viscosity was measured for a selection of these compounds as a function of temperature. Figure 4.1 shows measured viscosity for MA, EA, MP, MB, and PN, compared to EMC and DMC for temperatures between 0°C and 50°C. Note that while the properties of MF look promising in Table 4.1, it was not considered further because it showed poor performance in cells in lab tests (not shown in this work). The solvents that were considered further either had shown moderate to good performance in cells or had not yet been tested in full Li-ion cells. The viscosities of the esters and PN are all lower than that of EMC and DMC over the temperatures considered. The viscosity of DMC is lower than that of EMC, but it should be noted that its melting point is significantly higher (4.6°C, and -53°C, respectively, Table 4.1). The viscosity of MB is only marginally lower than that of DMC over this temperature range. The viscosity of PN is

comparable to that of EA. MA has the lowest viscosity of all the solvents considered. AEM calculations, shown as solid lines in Figure 4.1, agree well with the experimental viscosity of both the esters and carbonates. AEM calculations for PN agree well at room temperature, however at both high and low temperatures it diverges from experimental values. Uncertainties in the measurements are shown as vertical bars on Figure 4.1 and in subsequent Figures.
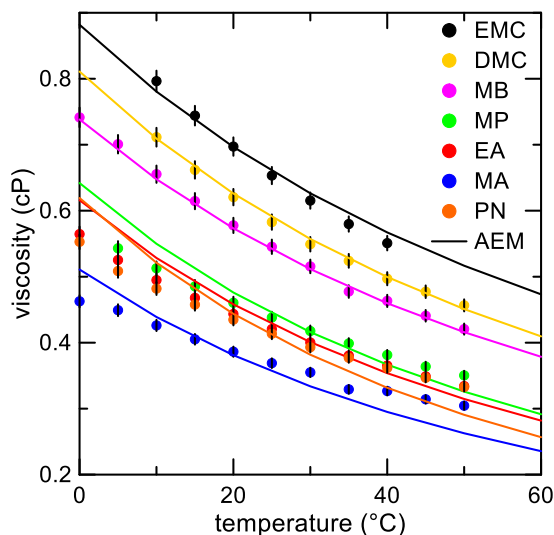
Figure 4.1: Viscosity measured as a function of temperature for pure solvents MA, EA, MP, MB, PN, EMC, and DMC. Solid lines are calculated viscosities from the Advanced Electrolyte Model (AEM).

Figure 4.2 shows (a) ionic conductivity and (b) viscosity for electrolytes composed of 1.2 M LiPF$_6$ (approximately 1.1 m) in (100-x)% [EC:EMC:DMC 25:5:70 (v/v)] + x% MF, with x = {0, 5, 20, 40, 60} (wt. %) for temperatures ranging from 0°C to 50°C. Similarly, Figures 4.3, 4.4, 4.5, 4.6, 4.7, 4.8, 4.9, and 4.10 show conductivity and viscosity for EF, PF, iBF, iBA, MP, MB, PN, and iBN, respectively. The temperature dependence of viscosity and conductivity is as expected; increased temperature leads to higher conductivity and lower viscosity at every weight fraction x of co-solvent added.

Except for iBA, as more co-solvent is added, a decrease in viscosity is observed. In the case of iBA (Figure 4.6), adding low weight fractions decreases the viscosity of the electrolyte, but as > 20% by weight is added to the solution, the viscosity increases at all temperatures. Similar trends are not seen in conductivity. Only the solvents MF, EF, PN, and iBN show increased conductivity as they are added alongside the carbonate solvent blend. Adding PF, iBA, iBF, or MB leads to a decrease in the electrolyte's conductivity, while little change in either direction is seen with MP. This most likely due to the fact that adding these co-solvents to the control blend of EC:EMC:DMC 25:5:70 (v/v) will decrease the overall proportion of EC in the electrolyte. With less EC in the electrolyte, the overall dielectric constant of the solution will be lower, since all the co-solvents studied have much lower dielectric constants than EC (see Table 4.1). This could lead to increased ion association between Li^+ and PF_6^-, thus resulting in a lower conductivity.
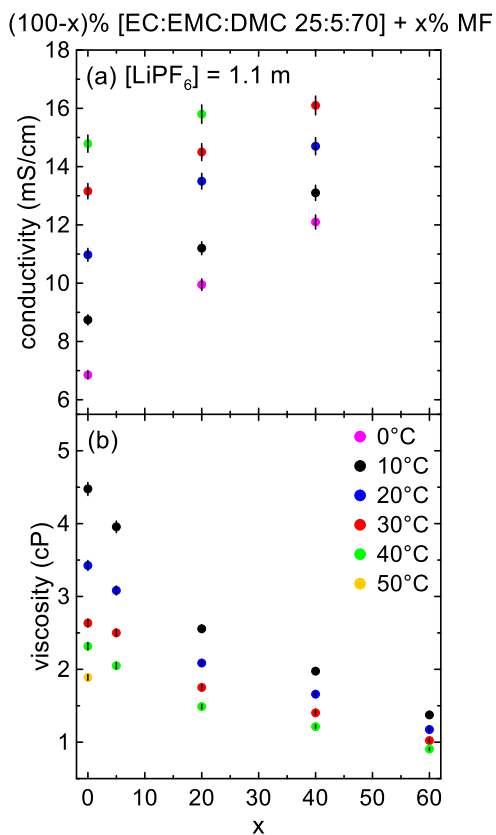
Figure 4.2: (a) Ionic conductivity and (b) viscosity as a function of weight fraction of co-solvent added for an electrolyte consisting of the solvent blend (100-x)% [EC:EMC:DMC 25:5:70 (v/v)] + x% methyl formate (MF) for different temperatures. The concentration of $LiPF_6$ used was 1.1 m.
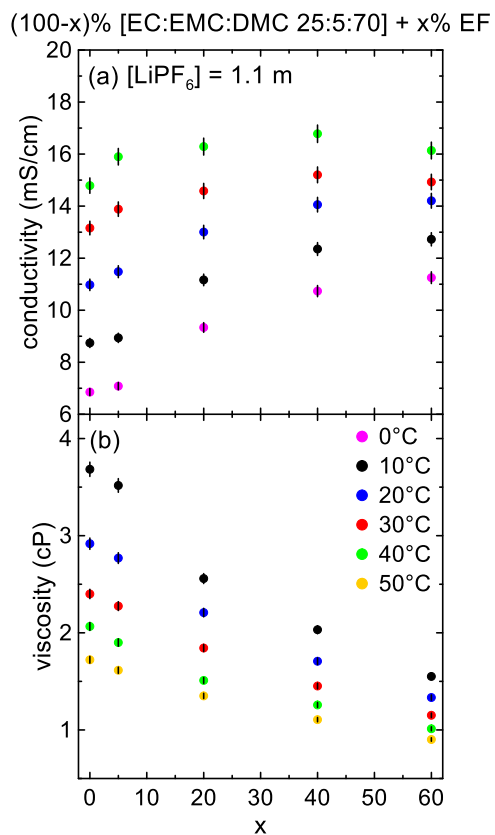
Figure 4.3: (a) Ionic conductivity and (b) viscosity as a function of weight fraction of co-solvent added for an electrolyte consisting of the solvent blend (100-x)% [EC:EMC:DMC 25:5:70 (v/v)] + x% ethyl formate (EF) for different temperatures. The concentration of LiPF$_6$ used was 1.1 m.
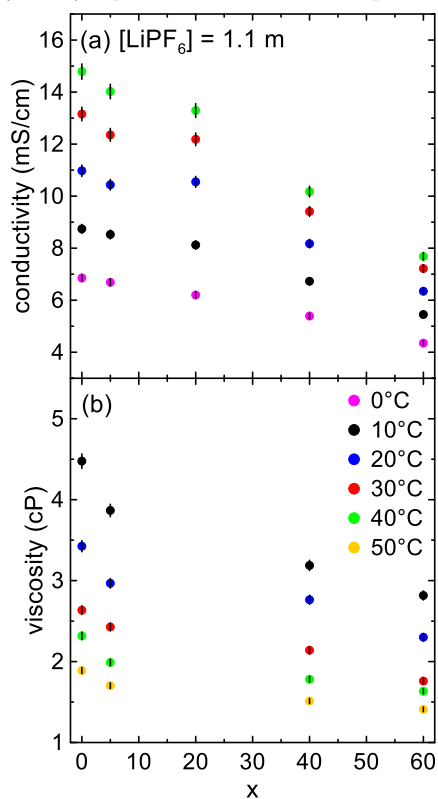
Figure 4.4: (a) Ionic conductivity and (b) viscosity as a function of weight fraction of co-solvent added for an electrolyte consisting of the solvent blend (100-x)% [EC:EMC:DMC 25:5:70 (v/v)] + x% propyl formate (PF) for different temperatures. The concentration of LiPF$_6$ used was 1.1 m.
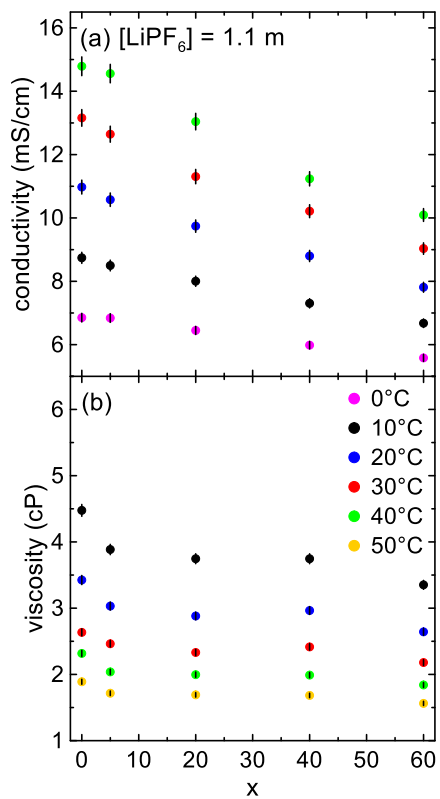
Figure 4.5: (a) Ionic conductivity and (b) viscosity as a function of weight fraction of co-solvent added for an electrolyte consisting of the solvent blend (100-x)% [EC:EMC:DMC 25:5:70 (v/v)] + x% isobutyl formate (iBF) for different temperatures. The concentration of LiPF$_6$ used was 1.1 m.
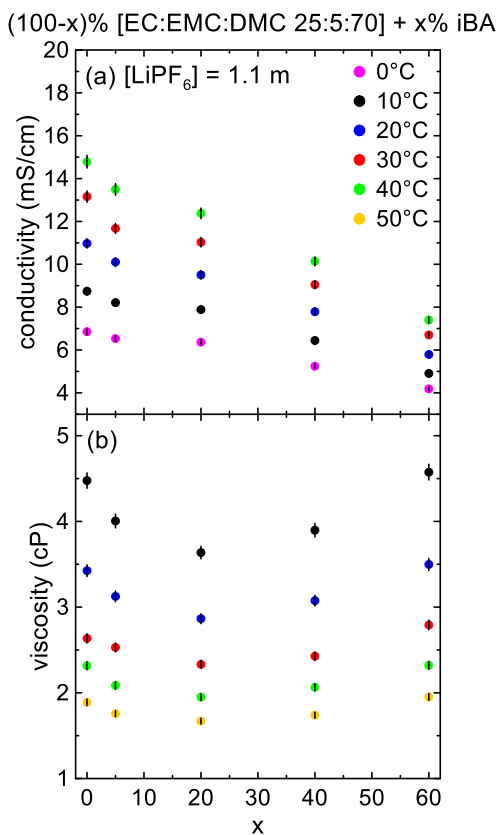
Figure 4.6: (a) Ionic conductivity and (b) viscosity as a function of weight fraction of co-solvent added for an electrolyte consisting of the solvent blend (100-x)% [EC:EMC:DMC 25:5:70 (v/v)] + x% isobutyl acetate (iBA) for different temperatures. The concentration of LiPF$_6$ used was 1.1 m.

(100-x)% [EC:EMC:DMC 25:5:70] + x% MP
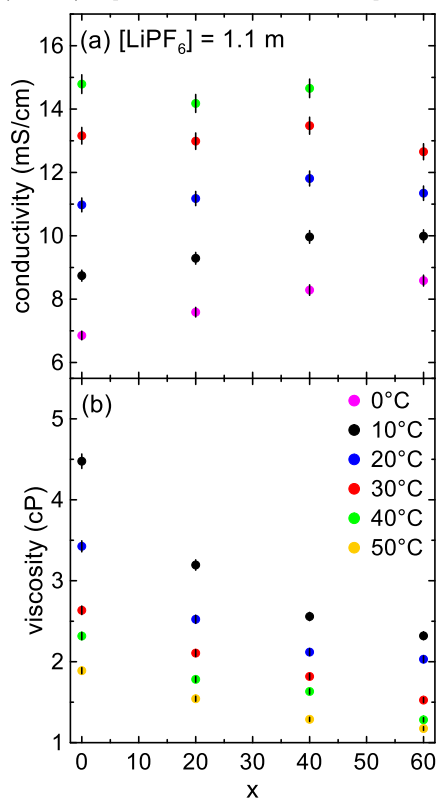
Figure 4.7: (a) Ionic conductivity and (b) viscosity as a function of weight fraction of co-solvent added for an electrolyte consisting of the solvent blend (100-x)% [EC:EMC:DMC 25:5:70 (v/v)] + x% methyl proprionate (MP) for different temperatures. The concentration of LiPF$_6$ used was 1.1 m.

(100-x)% [EC:EMC:DMC 25:5:70] + x% MB
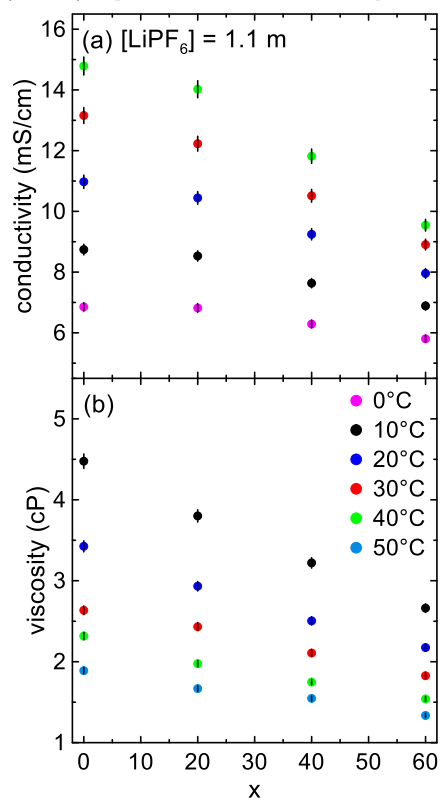
Figure 4.8: (a) Ionic conductivity and (b) viscosity as a function of weight fraction of co-solvent added for an electrolyte consisting of the solvent blend (100-x)% [EC:EMC:DMC 25:5:70 (v/v)] + x% methyl butyrate (MB) for different temperatures. The concentration of $LiPF_6$ used was 1.1 m.
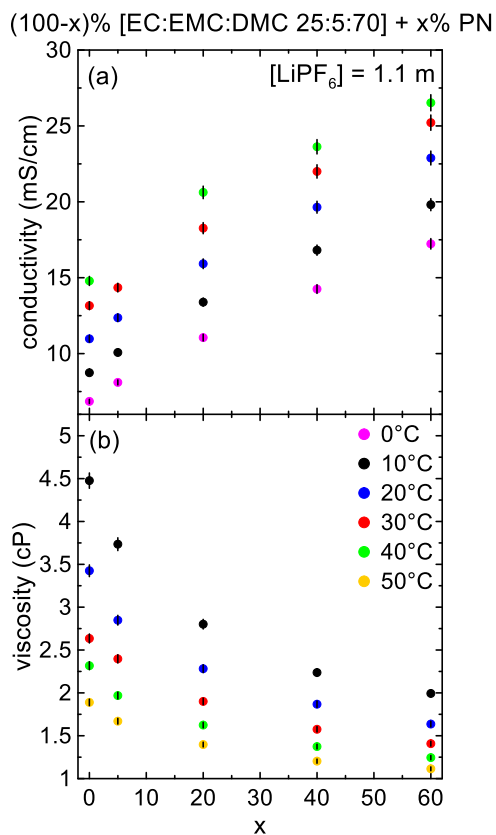
Figure 4.9: (a) Ionic conductivity and (b) viscosity as a function of weight fraction of co-solvent added for an electrolyte consisting of the solvent blend (100-x)% [EC:EMC:DMC 25:5:70 (v/v)] + x% propionitrile (PN) for different temperatures. The concentration of LiPF$_6$ used was 1.1 m.
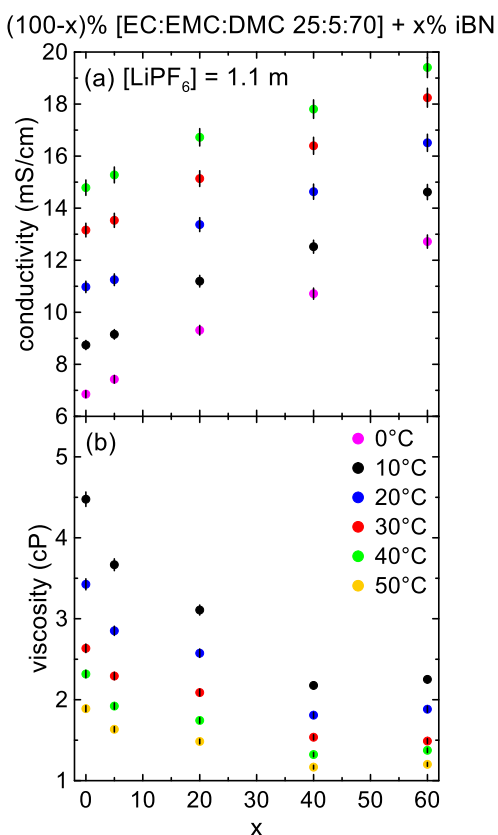
Figure 4.10: (a) Ionic conductivity and (b) viscosity as a function of weight fraction of co-solvent added for an electrolyte consisting of the solvent blend (100-x)% [EC:EMC:DMC 25:5:70 (v/v)] + x% isobutyronitrile (iBN) for different temperatures. The concentration of $LiPF_6$ used was 1.1 m.

Figure 4.11 gives a summary of the impact of the various co-solvents studied above, as well as the esters MA and EA. Figure 4.11 (a) shows conductivity as a function of temperature for electrolytes composed of 1.1m $LiPF_6$ in 80% [EC:EMC:DMC 25:5:70 (v/v)] + 20% A, where A = {PN, MA, iBN, EF, EA, MF, MP, MB, PF, iBF, iBA}. Figure 4.11 (b) shows viscosity as a function of temperature for the same set of electrolytes. A control electrolyte (denoted "ctrl") composed of 1.2m $LiPF_6$ in EC:EMC:DMC 25:5:70 (v/v) is shown in both Figures 4.11(a) and 4.11(b) for comparison.
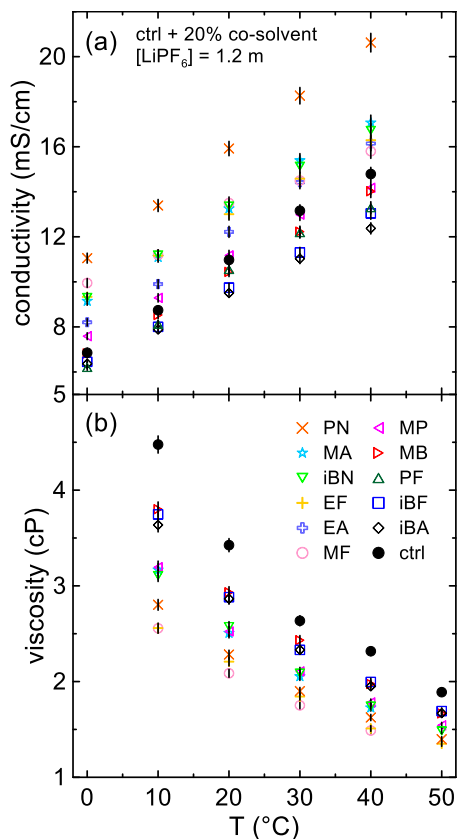
Figure 4.11: (a) Ionic conductivity and (b) viscosity as a function of temperature for electrolytes containing 20% by weight of different co-solvents. In this Figure, ctrl denotes a mixture of EC:EMC:DMC 25:5:70 (v/v).

The trend in the viscosity of electrolytes as a function of the amount of low-viscosity co-solvent added echoes the results presented in Figure 4.1. The base electrolyte has the highest viscosity at all temperatures. Adding 20% by weight of any of the various co-solvents to the electrolyte lowers the viscosity to some degree. The electrolyte containing MF has the lowest viscosity of all electrolytes studied. Adding PN to the electrolyte appears to give the largest boost in conductivity. The co-solvents MA, MF, EF, EA, and iBN show good increases in conductivity compared to the control. The electrolyte containing MP appears to perform only marginally better than the control electrolyte. At elevated temperatures, the conductivity for the electrolyte containing MB

is lower than the ester-free electrolyte. Other studies have also observed a drop in conductivity when adding MB as a co-solvent[92,93]. Adding the co-solvents PF, iBA, or iBN also gives a decrease in conductivity. Over the whole temperature range, the electrolyte containing MA outperforms the other esters studied.

Although the co-solvent PN performed better than MA in terms of conductivity, there has been little work done on the viability of PN-containing electrolytes in full Li-ion cells. One study has considered the viability of using nitrile-containing electrolytes (including PN) in Li-ion cells destined for low-temperature applications[96]. A forthcoming publication will show that PN is not compatible with the Li-ion cell chemistries and baseline electrolytes that are normally used in our studies[97]. On the other hand, esters have already been shown to work alongside carbonate solvents in full cells over many cycles[30,35,38]. Therefore, the remainder of this chapter will focus primarily on MA as a co-solvent.

The impact of MA on electrolyte viscosity and conductivity was studied systematically as a function of MA content, $LiPF_6$ concentration, and temperature. Two different ternary solvent blends were considered: EC:EMC:MA 30:(70-x):x, and EC:DMC:MA 30:(70-x):x, with x = {0, 10, 20, 30}. The fraction of EC in the electrolyte was held constant throughout. Figure 4.12 shows electrolyte viscosity as a function of $LiPF_6$ concentration for electrolytes with solvents a) EC:EMC 30:70, b) EC:EMC:MA 30:60:10, c) EC:EMC:MA 30:50:20, and d) EC:EMC:MA 30:40:30, for temperatures ranging from 10°C to 40°C. It is clear here that viscosity over both temperature and $LiPF_6$ concentration decreases monotonically with the addition of MA, with 30% MA-containing electrolytes having the lowest observed viscosity. The dependence of

viscosity on LiPF$_6$ concentration changes depending on other conditions such as temperature or MA content. In electrolytes at low temperatures without MA, the dependence of viscosity on salt concentration is nearly quadratic. This can become a serious issue in the operation of real Li-ion cells. Such a large increase in viscosity should lead to a corresponding severe drop in conductivity. This may inhibit the performance and/or lifetime of cells under high rates of charge and discharge[6]. This dependence of viscosity on salt concentration is much weaker at higher temperatures, where the increase in viscosity over LiPF$_6$ concentration is only moderate.
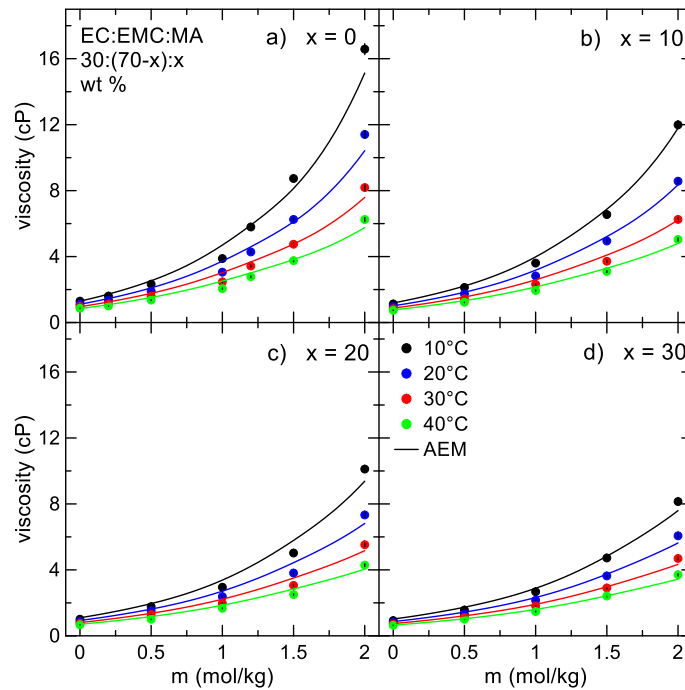
Figure 4.12: Viscosity as a function of LiPF$_6$ concentration for electrolytes with the solvent composition EC:EMC:MA 30:(70-x):x, with a) x=0, b) x=10, c) x=20, and d) x=30 for temperatures between 10°C and 40°C. Solid lines are calculations from the AEM.

Figure 4.13 shows viscosity as a function of temperature for electrolytes of the form EC:DMC:MA 30:(70-x):x, x = {0, 10, 20, 30}, where similar trends are seen. However, the viscosity for this system is lower than electrolytes composed of

EC:EMC:MA. This is to be expected since the viscosity of DMC is slightly lower than that of EMC at all temperatures (Figure 4.1).
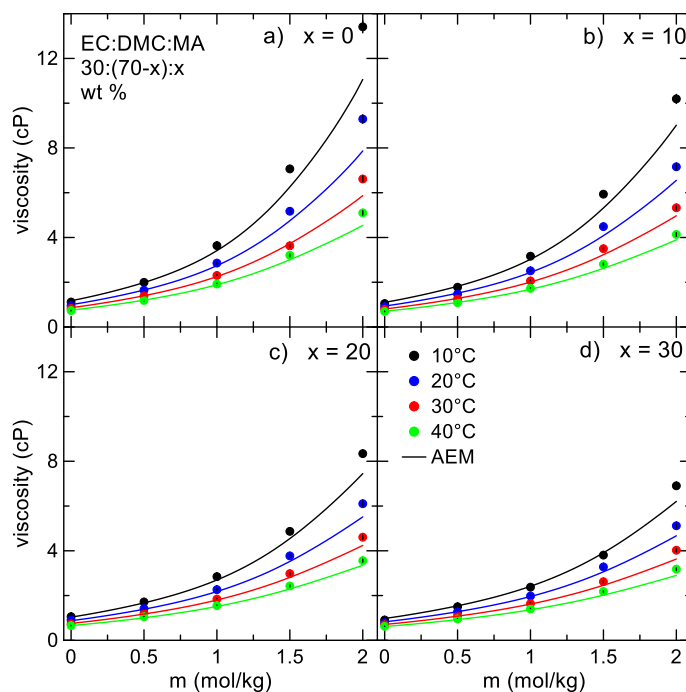
Figure 4.13: Viscosity as a function of LiPF$_6$ concentration for electrolytes with solvent composition EC:DMC:MA 30:(70-x):x, with a) x=0, b) x=10, c) x=20, d) x=30 for temperatures between 10°C and 40°C. Solid lines are predictions from the AEM.

In Figures 4.12 and 4.13, calculations from the AEM are shown as solid lines. AEM calculations agree well with the experimental viscosity data, especially at low concentrations of salt. It correctly captures the dependence of viscosity on temperature, and correctly predicts the impact of adding MA. At very high concentrations of salt (2.0 m) and lower temperatures, the AEM starts to deviate from the experimental data. The average deviation of the AEM viscosity calculations from experiment over all conditions is 5.5%. Average deviation for pure solvents (i.e. 0 m LiPF$_6$) over all temperatures is 4.4%, while the average deviation from experiment for electrolytes with 0.5 m, 1.0 m, 1.5 m, and 2.0 m LiPF$_6$ is 5.7%, 7.6%, 4.9%, and 4.9%, respectively, over all temperatures.

Viscosity measurements are consistently accurate and repeatable. This has been demonstrated for water and other non-aqueous solvents[98]. Due to the relatively low uncertainty in the viscosity measurements (see Chapter 3.1.2), in many cases where there is greater disagreement between experiment and AEM calculations the disagreement is taken to be a limitation of the AEM model. This is better seen in Figure 4.12 at high concentrations of salt in electrolytes without MA (x=0), where the AEM under-estimates the experimental result at the lowest temperature, yet is still within about 8% of the experimental value.

Figure 4.14 shows conductivity as a function of $LiPF_6$ concentration for electrolytes of the form EC:EMC:MA 30:(70-x):x, x = {0, 10, 20, 30}, for temperatures ranging from 0°C to 40°C. AEM calculations are displayed as solid lines. Panels (a) to (d) show increasing MA content in the electrolyte. The maximum conductivity (κ_{max}) increases as MA is added at all temperatures. Additionally, the $LiPF_6$ concentration corresponding to maximum conductivity (c_{max}) increases slightly with increasing MA content. c_{max} has been shown to depend on the dielectric constant of the solvent system[6], but is also profoundly impacted by viscosity. Since MA has a slightly higher dielectric constant than EMC (Table 4.1), replacing EMC with MA in the electrolyte should marginally increase the dielectric constant of the electrolyte, and thereby lessen conductivity-robbing ion association.
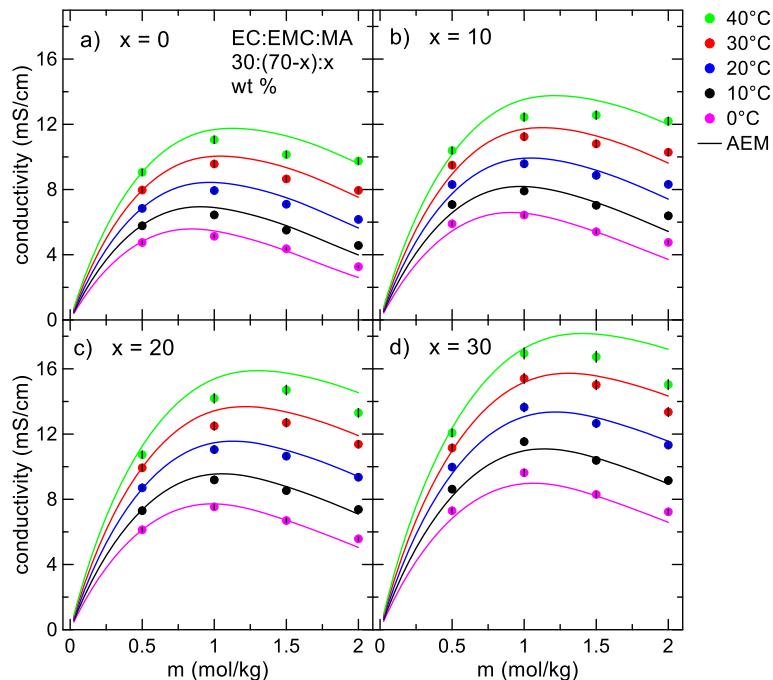
Figure 4.14: Conductivity as a function of LiPF$_6$ concentration for electrolytes with the solvent composition EC:EMC:MA 30:(70-x):x, with $0 \leq x \leq 30$ (wt. %) for temperatures between 0°C and 40°C. Calculations from the AEM are shown as solid lines.

During the operation of a Li-ion cell, especially at high charge rate, local variations in salt concentration arise[68]. As well, over the lifetime of the cell, various reactions between solvent molecules, salt species, and the positive and negative electrodes can also lead to consumption of salt[84]. Therefore, in addition to the importance of the maximum conductivity, an electrolyte chosen for high-rate cycling should maintain a high conductivity over a wide range of salt concentrations. Adding MA as a co-solvent slightly increases the width of the conductivity profile, as seen in Figure 4.14.

Figure 4.15 shows plots of conductivity as a function of LiPF$_6$ concentration for electrolytes with solvents EC:DMC:MA 30:(70-x):x, x = {0, 10, 20, 30} in the temperature range 0°C – 40°C, with corresponding AEM calculations shown as solid

lines. In Figures 4.12 and 4.13, it was found that the viscosities of DMC-containing electrolytes over all conditions were lower than in corresponding EMC-containing electrolytes. Similarly, the conductivities of DMC-containing electrolytes tend to be higher than their EMC-containing counterparts. At 40°C, the AEM predicts the maximum conductivity for an electrolyte with the solvent blend EC:DMC:MA 30:40:30 is around 20 mS/cm, while the maximum conductivity for EC:EMC:MA 30:40:30 is closer to 16 mS/cm at the same temperature. This difference in conductivity will begin to matter more at low temperature, especially at very high charging rates. In Figure 4.15, c_{max} shifts higher when larger proportions of MA are added to the electrolyte, again due to the small increase in dielectric constant and decrease of viscosity on the addition of MA. As well, the width of the conductivity curves is increased, more so than in the EMC-containing electrolytes, which will be desirable in high charge-rate cells as described above.
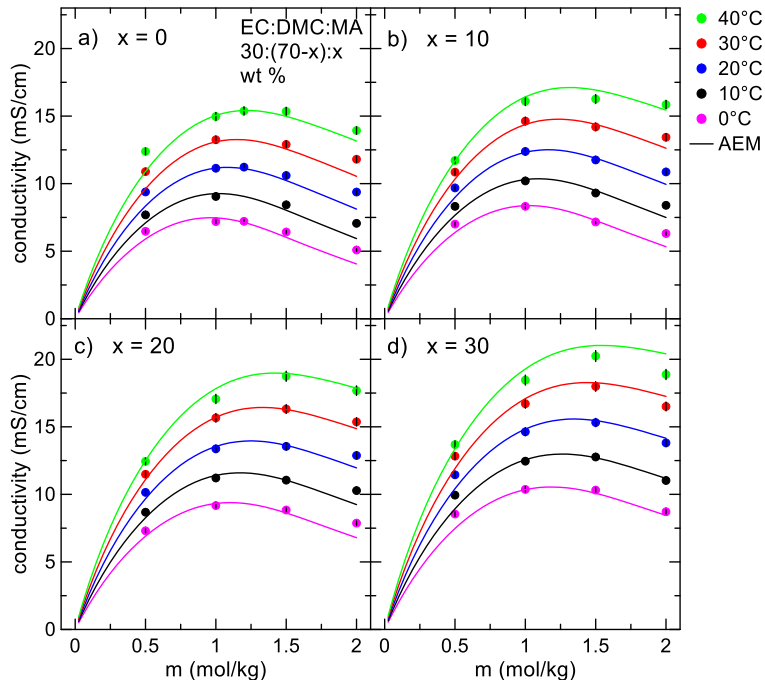
Figure 4.15: Conductivity versus LiPF$_6$ concentration for electrolytes with solvent compositions EC:DMC:MA 30:(70-x):x for $0 \leq x \leq 30$ for a range of temperatures between 0°C and 40°C. Solid lines are calculations from the AEM.

AEM calculations are compared to the experimental conductivity results in Figures 4.14 and 4.15. Again, like the viscosity results in Figures 4.12 and 4.13, the AEM does well in predicting the experimental conductivity values. AEM calculations have an average deviation from experiment of 4.9% over all temperatures and concentrations. The AEM agrees better with conductivity data at lower concentrations of LiPF$_6$. The average deviation from experiment is 4.9% at 0.5 m, 3.2% at 1.0 m, 3.2% at 1.5 m, and 8.3% at 2.0 m LiPF$_6$. Again, as was concluded for the viscosity results (Figures 4.12 and 4.13), disagreements between experiment and model results are due to limitations of the AEM.

Figures 4.16 (a) and (b) show the percentage conductivity increase as a function of MA content, x, in electrolytes with solvent blends EC:EMC:MA and EC:DMC:MA,

respectively, at 20°C for different concentrations of LiPF$_6$. The percentage increase is a relative increase for a given LiPF$_6$ concentration.

Figures 4.16 (c) and (d) show viscosity as a function of MA content for electrolytes of the form EC:EMC:MA and EC:DMC:MA, respectively, again at 20°C for different LiPF$_6$ concentrations. Decreasing viscosity is seen on the addition of MA at all concentrations of LiPF$_6$. As the salt concentration in the electrolyte is increased, a greater absolute decrease in viscosity is seen. Similarly, adding MA impacts conductivity at all salt concentrations, as seen in Figures 4.16 (a) and 4.16 (b). The increase is smaller for lower salt concentrations, but even at 0.5 m, a conductivity boost above 20% is seen for EMC-containing electrolytes when only 20% MA is added to the electrolyte. The increase in conductivity at 2.0 m LiPF$_6$ and 20% MA in Figure 4.16 (a) is over 40%. The magnitude of the increase in conductivity for DMC-containing electrolytes (Fig. 4.16 (b)) is lower than for EMC-containing electrolytes (Fig. 4.16 (a)); at 2.0 mol/kg LiPF$_6$ and 20% MA, the conductivity increase is only about 40%.
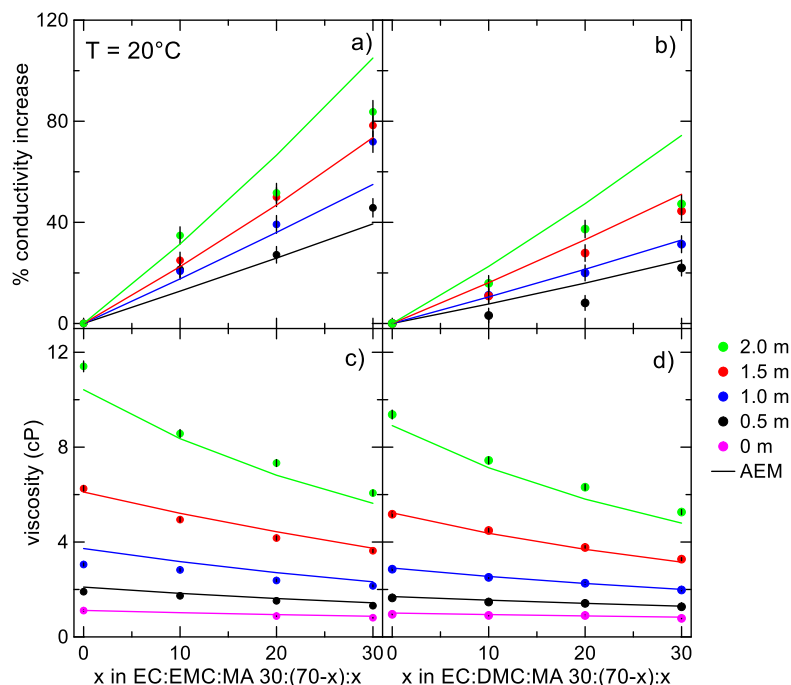
Figure 4.16: Percent change in conductivity at 20°C with increasing MA content for solvent blends EC:EMC:MA 30:(70-x):x and EC:DMC:MA 30:(70-x):x is shown in panels a) and b), respectively. Panels c) and d) show viscosity as a function of MA content for solvent blends EC:EMC:MA 30:(70-x):x and EC:DMC:MA 30:(70-x):x, respectively, also at 20°C. Different concentrations of $LiPF_6$ are shown, ranging from 0 m to 2.0 m.

AEM calculations are shown for all conditions in Figure 4.16. The AEM agrees well with the experimental data for the solvent compositions ranging from 0% to 30% MA content. Some large deviations from experiment are seen at 2.0 m $LiPF_6$ in Figures 4.16 (a) and (b). Looking at panels (c) and (d) in Figure 4.16, AEM predictions for the viscosity of pure solvent blends (0 m) almost exactly match the experimental data. Agreement with experiment drifts a little as $LiPF_6$ concentration is increased, and at 2.0 m $LiPF_6$, the AEM slightly under-estimates the experimental viscosity for all electrolytes.

4.2.1   Stokes' Law conductivity

The expression for conductivity derived by Gering that is used in the AEM is based on an expanded expression of Stokes' Law for ionic conductivity that accounts for key phenomena that influence conductivity: solvent-ion interactions (ion solvation) and solvated ion sizes as f(conc., T), ion-ion interactions (ion association and electrostatic interactions), viscosity, counter-ion transport, ionic random motion effects and ionic hopping[10].   As shown in Chapter 2, if Stokes' Law is obeyed for a solvated ion approximated as a hard sphere, then the ionic conductivity κ can be found to be

$$\kappa = \sum_i \frac{F|z_i^2|ec_i}{6\pi\eta r_i} \tag{4.1}$$

where z_i is the charge on the ion, F is Faraday's constant, e is the elementary charge, and c_i is the molar concentration of ionic species.   If it is assumed that the salt is fully dissociated, the concentration of charged species is equal to the concentration of salt added. Under this simple model, κ should be inversely proportional to η for a given salt concentration if the Stokes' radius is unchanged for different solvent blends. If this is true, Equation 4.1 can be simplified to

$$\kappa = \frac{Kc_0}{\eta} \tag{4.2}$$

where K is a constant. The simple Stokes' Law model has been previously shown to be approximately true by Dudley et al. for electrolytes containing $LiAsF_6$ salt and sulfolane mixed with various glyme solvents[47]. The AEM provides an advantage through direct calculation of ion association, making possible the determination of all populations of single (free) ions, ion pairs as contact (CIP) and solvent-shared (SShIP) species, as well as CAC^+ and ACA^- triple ion species. All non-neutral charged species are accounted for

in conductivity through the AEM[10]. In so doing, the AEM provides a path to diagnosing attributes of Walden-type plots.

Figure 4.17 shows conductivity plotted versus inverse viscosity for the different electrolytes studied. Different solvent mixtures are given by unique closed plotting symbols, and different temperatures are specified by colour. AEM calculations for these electrolytes are also plotted in Figure 4.17, using corresponding open symbols for a given solvent blend. $LiPF_6$ concentrations of 0.5 m, 1.0 m, and 2.0 m are shown. Note that data are grouped according to molal concentration even though Equation 4.2 has a factor of molar concentration. It is assumed for simplicity that for a given molal concentration, the corresponding molar concentrations are approximately equal for the different solvent blends.

For each concentration of salt, linear regressions were performed on the data, with the y-intercept forced to 0. All the electrolytes roughly agree with the Stokes' law model. This shows that for a given concentration, the Stokes radius, which is a simple way of expressing the solvated ionic radius, remains approximately unchanged. The Stokes radius should change with different solvent mixtures. Indeed, there is some spread away from the ideal Stokes behaviour in Figure 4.17. Most notably, some MA-containing electrolytes at 40°C and 0.5 m $LiPF_6$ deviate from the fit. In these cases, solvent-ion interactions become non-negligible and the electrolyte conductivity cannot be solely viscosity driven. As example considerations, the solvated ion sizes may vary with choice of solvent mixture and decrease at greater salt concentration.

The AEM captures these more complicated solvation effects and is outlined in the literature[8,10]. However, Figure 4.17 shows that the Stokes' Law model serves as a good

first approximation for electrolyte conductivity in these systems, meaning that for these MA containing electrolytes the conductivity can be roughly predicted from the viscosity. Predictions from the AEM for these electrolytes in Figure 4.17 show that the expected deviation from the simple Stokes' behaviour is small in most cases.
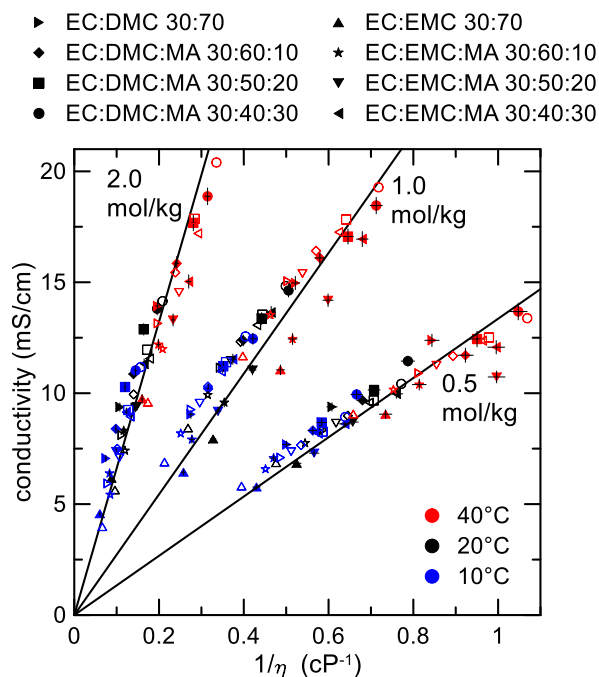
Figure 4.17: Conductivity versus inverse viscosity for several different electrolyte compositions at 10°C, 20°C, and 40°C. LiPF$_6$ concentrations of 0.5 mol/kg, 1.0 mol/kg, and 2.0 mol/kg are shown. Symbol type specifies specific solvent blends. Closed symbols are for experimental data, while corresponding AEM calculations are shown as open symbols. Solid lines correspond to linear fits of each respective concentration. Fits were constrained to pass through the point (0,0) as per Equation 4.2.

4.2.2   Walden analysis

In the simplest Stokes' law approximation, it was assumed that the Li salt is fully dissociated in solution. The high-dielectric solvent, EC, helps dissociate the Li salt, but in the systems studied, EC only makes up 30% of the electrolyte solvent by weight. As was

shown in Chapter 2, a related expression to Stokes' Law conductivity is the empirical Walden rule

$$\Lambda\eta = const. \qquad (4.3)$$

where Λ is the molar conductivity σ/c. A fully dissociated electrolyte should obey the expression

$$\log\Lambda = \log\frac{1}{\eta} \qquad (4.4)$$

obtained for dilute aqueous KCl, which is assumed to be fully dissociated in solution. The validity of the assumptions made for using KCl as an ideal reference have been put into question recently, especially when comparing with ionic liquids[59]. However, the traditional interpretation states that points close to the KCl line are taken to be nearly fully dissociated, while points below the line have a lower degree of dissociation (ionicity)[67]. This analysis should give an indication about the ionicity of the electrolytes studied.

Figure 4.18 shows a Walden plot for the same electrolytes presented in Figure 4.17. LiPF$_6$ concentrations of 0.5 m, 1.0 m, and 2.0 m, and temperatures of 10°C, 20°C, and 40°C are shown. The data roughly follow a linear trend below the ideal KCl line, yet there is greater deviation from the line noted at the lower concentrations. First, this suggests that at each salt concentration there is a modest but relatively consistent amount of ion pairing present in these electrolytes across all solvent compositions. Second, note that solvated ion sizes are also part of the Stokes' Law expression, however they decrease with increasing salt concentration, whereas viscosity increases. This aspect of greater ion solvation activity at lower salt concentration, with commensurate larger Stokes radii, helps explain why the Walden plots of lower-concentration data deviate more from the

ideal KCl line, which is a good baseline considering that both K^+ and Cl^- are minimally solvated[8].

The magnitude of the solvated ionic diameters will be a predominant influence for the departure of the Walden plots from the ideal line. Adding MA does not seem to impact the ionicity of the electrolyte. This may be expected considering that the dielectric constants of EMC, DMC, and MA are on the same order of magnitude (Table 4.1). As well, deviation from the KCl line stays approximately constant across the range of $LiPF_6$ concentrations considered. Gering predicts ion pair population in the EC:EMC 30:70 system to increase from a molar fraction of 0.01 to about 0.08 between 0.5 m and 2.0 m $LiPF_6$. Gering also predicts an increase in triple ion population over the same concentration range, and at 2 m $LiPF_6$ ion pair and triple ion populations are almost equal. Figure 4.18 suggests that the total fraction of ionic species (single ions and triple ions) does not significantly change, even at high salt concentrations. Since the AEM calculates low ion pair populations at concentrations up to 2.0 m, its predictions are consistent with this result. Therefore, the characteristic drop in conductivity seen beyond a critical concentration (Figures 4.14 and 4.15) must be primarily due to an increase in viscosity for these electrolytes rather than significant ion pairing.

Previous work on the conductivity of $LiPF_6$-based carbonate electrolytes has suggested that ion association plays an important role in the decrease in conductivity observed above ~1.5 m $LiPF_6$[56], however it this does not appear to be accurate based on this work. It may still be possible that ion association plays a larger role at concentrations larger than 2.0 m.
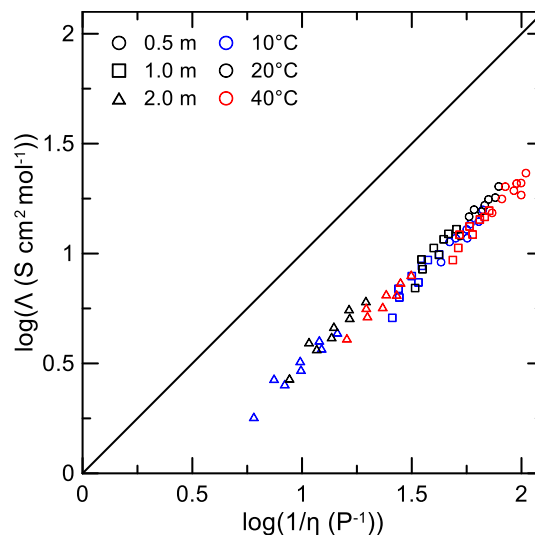
Figure 4.18: Walden plot for the electrolytes considered in Figure 4.17. LiPF$_6$ concentrations of 0.5 m, 1.0 m, and 2.0 m are shown. Temperatures of 10°C, 20°C, and 40°C are shown as different colours. The solid line corresponds to the diluted KCl reference, which is taken to be the region of the plot where the ions are fully dissociated.

4.3 CYCLING RESULTS

Figure 4.19 shows cycling results for cells with electrolytes of the form (100-x)% [EC:EMC 30:70 + 2% FEC] + x% MA, for x = {0, 20, 40} (wt. %). Discharge capacity is plotted as a function of cycle number for single crystal NMC532 /artificial graphite (AG) pouch cells. Cells with 0% MA show minimal fade at 1C rate charge, but at 1.5C charge and 2C charge, dramatic capacity fade is observed due to unwanted lithium plating[99,100]. Cells with 20% MA and 40% MA show virtually no fade at these high charging rates. This shows that the addition of as little as 20% MA to the electrolyte greatly improves the charge rate capability of NMC532/AG cells by eliminating unwanted lithium plating. However, there is some evidence that adding MA sacrifices some long-term lifetime. Li et al. have shown from ultra-high precision charging (UHPC) that MA may make the electrolyte less stable when cycling to high voltages[40]. Long term

cycling at low charging rate (C/3) showed that cells with MA in the electrolyte had slightly larger capacity fade over 800+ cycles than cells without MA[40]. Isothermal microcalorimetry experiments showed an increase in parasitic heat flow with increasing MA content, which suggests shorter lifetimes over the long-term[40]. This in part reaffirms conclusions initially made by Smart[30], which state that short-chain esters may negatively impact the lifetime of cells. However, it is clear from Figure 4.19 that MA-containing electrolytes are far superior at very high charge rates.
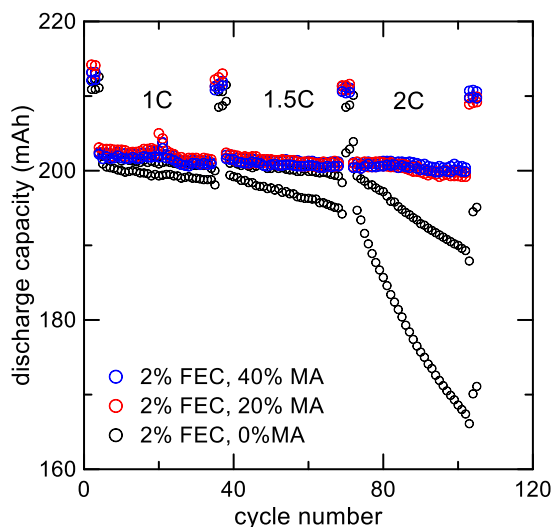
Figure 4.19: Discharge capacity versus cycle number for single crystal Li[Ni$_{0.5}$Mn$_{0.3}$Co$_{0.2}$]O$_2$ (NMC532)/ artificial graphite pouch cells charged at different rates at 20ºC. All cells were discharged at a rate of 0.5C. All cells contain 2% by weight fluoroethylene carbonate (FEC) in the electrolyte. Cells containing 0%, 20% and 40% MA by weight in the electrolyte are shown. Two identical cells were made for each unique electrolyte.

4.4 CONCLUSION

In this chapter, the transport properties of Li electrolytes containing different co-solvents were measured. Many candidate co-solvents were considered, falling into two classes:

esters and nitriles. Of these co-solvents, MA, EA, MF, EF, PN, and iBN showed increased conductivity as well as decreased viscosity when they were added to a control electrolyte composed of traditional carbonate solvents. Except for iBA, all co-solvents studied lead to a decreased viscosity when added to the control electrolyte. Of the esters, MA performed the best in initial tests, so its impact on electrolyte transport properties was studied systematically. Ionic conductivity and viscosity were then measured as a function of temperature for a wide range of electrolytes containing different concentrations of $LiPF_6$ and MA. Two electrolyte systems were tested, EC:linear carbonate:MA 30:(70-x):x, with linear carbonate = {EMC, DMC} and x = {0, 10, 20, 30} (wt. %), with $LiPF_6$ concentrations ranging from 0 m to 2 m. Results from these measurements showed that adding MA gave a significant increase in conductivity over a wide range of salt concentrations. Decreases in viscosity were observed across all $LiPF_6$ concentrations when MA was added.

The Advanced Electrolyte Model (AEM) was successfully able to predict properties of electrolytes containing MA over a range of different conditions. Deviations between AEM predictions and experimental data were minor (averages of about 5% for both viscosity and conductivity), and while they did increase in selected extreme cases they stayed within modest boundaries. The experimental data can roughly be described using a simple expression derived from Stokes' law, suggesting that the Stokes' radii remain relatively unchanged over the different solvent compositions. A Walden analysis of the different electrolytes suggests that neither MA content nor $LiPF_6$ significantly impact the ionicity of the electrolyte in the ranges studied.

Cycling data for single NMC 532/artificial graphite cells shows that adding as little as 20% MA by weight to the electrolyte can dramatically improve capacity retention at high charge rates by eliminating unwanted lithium plating. Very little capacity fade is seen at charging rates as high as 2C. MA looks to be a promising co-solvent for high power Li-ion cells.

CHAPTER 5 TRANSPORT PROPERTIES OF LOW-EC ELECTROLYTES

Electrolyte solution preparation and transport property measurements in this chapter were done by the author with the assistance of Erin Tonita. Cells for DTA measurements were prepared by the author, and DTA measurements were carried out by Michael Bauer. Cell cycling data was provided by Lin Ma and Dr. Jing Li. All data analysis and interpretation was done by the author of this thesis.

5.1 INTRODUCTION

Typical non-aqueous Li-ion battery electrolytes composed of ethylene carbonate (EC), ethyl methyl carbonate (EMC), and/or dimethyl carbonate (DMC) may not be suitable in high voltage cells because oxidation of EC at the positive electrode at high voltage can cause significant gas generation and impedance growth[28]. Due to the high dielectric constant of EC, which is crucial for dissociating Li salts in solution, it has traditionally been considered an indispensable component of non-aqueous liquid electrolytes for Li-ion cells[6]. Recently, there has been increasing interest in using alternative electrolyte systems that do not contain EC for high-voltage cycling[28,45,101-104]. Electrolytes composed primarily of linear carbonates (e.g. EMC) or esters such as ethyl acetate (EA) or methyl propionate (MP) plus ~5% by weight of "enabling" additives such as fluoroethylene carbonate (FEC) are promising electrolyte systems for cells operating at high voltage[19,28,33,34,45,105,106]. Additionally, electrolytes containing comparatively low concentrations of EC (< 30% by weight) have been shown to be promising for low-temperature applications[23,107].

There have been other novel approaches to designing electrolytes for high voltage operation that will not be discussed and considered in this Chapter. For example, Wang et al. recently showed that electrolytes containing high (> 3 M) concentrations of lithium bis(fluorosulfonyl) imide (LiFSI) in trimethyl phosphate (TMP) can function well in Li-ion cells[108]. Yamada et al. showed that highly concentrated electrolytes containing acetonitrile as the sole solvent could also function well in Li-ion cells[109]. Petibon et al. showed that ethyl acetate could function as the primary solvent in lithium ion cells when high concentrations of LiFSI were used[34]. There have also been several other studies showing that highly concentrated electrolytes can render uncommon solvents effective in electrolytes for lithium-ion cells. However, this approach suffers from the high cost of the salts required.

With the current interest in EC-free electrolytes, it is important to evaluate the transport properties of these low-EC and EC-free electrolytes. In this Chapter, viscosity and ionic conductivity are measured for $LiPF_6$-based electrolytes containing the binary solvent mixtures EC:EMC and EC:DMC, for a range of EC compositions. Calculations from the AEM are used to further understand the transport properties of these electrolytes. A partial phase diagram for the EC:DMC:$LiPF_6$ system is constructed using differential thermal analysis (DTA). Li[$Ni_{0.4}Mn_{0.4}Co_{0.2}$]O_2 (NMC442)/graphite pouch cells and single crystal Li[$Ni_{0.5}Mn_{0.3}Co_{0.2}$]O_2 (NMC532)/graphite pouch cells are cycled up to 4.4 V to test the effectiveness of EC-free electrolytes in high-voltage cells.

5.1.1   Adapting the AEM for low dielectric systems

In Chapter 4, the AEM was validated for electrolytes containing the solvents EC, EMC, DMC, and the ester methyl acetate (MA)[8,10,110]. The systems that have been validated

106

contained considerable amounts of EC (25-30% by weight). Modeling the properties of low permittivity electrolytes is especially difficult in the chemical physics framework of the AEM. This is touched on below, but a detailed explanation of the modeling challenges is beyond the scope of this work. AEM version 2.17.5 was used for all calculations in this chapter.

To support the emphasis on EC-lean and EC-free electrolytes, the AEM theory was adapted to consider low permittivity conditions of linear carbonates and other classes of solvents by Gering. Classical theory of ion association is not capable of correct interpretation of such extreme conditions because it views an electrolyte system as a continuum with a static dielectric "constant." However, the AEM does not assert a dielectric constant for the chosen solvents, but rather determines how the ionic fields and ion pair dipoles influence the solvent permittivity (within a colligative context) in behavior broadly referred to as "dielectric depression"[111]. In short, solvent permittivity decreases in the presence of free ions due to field effects on solvent dipoles and other aspects of molecular entropy. For most systems of modest to high permittivity (say, dielectric constant of 20 or higher), the dielectric depression is readily seen as salt concentration is increased. For example, Figure 5.1 shows AEM calculations for the solution permittivity as a function of $LiPF_6$ concentration for electrolytes of the form EC:DMC x:(100-x) (wt. %). For the solvent blend EC:DMC 30:70, dielectric depression occurs more or less continuously for $LiPF_6$ concentrations between 0 and 1 mol/kg. However, for low-permittivity systems (i.e. DMC), the occurrence of dielectric depression is minor as salt is added, whereafter further salt addition causes permittivity to increase well past the pure solvent value, enabling greater dissociation of salt into free

ions. This is due to the presence of ion pairs, which function as dipoles and thereby add to the solution permittivity.

The AEM calculations that support simultaneous equilibrium-state determination of free ions, ion pairs (contact ion pairs (CIP), solvent shared ion pairs (SShIP), solvent separated ion pairs (SSIP)), triple ions (TI), solvent permittivity and solution permittivity are very complex and require several levels of iteration that must converge in concert.
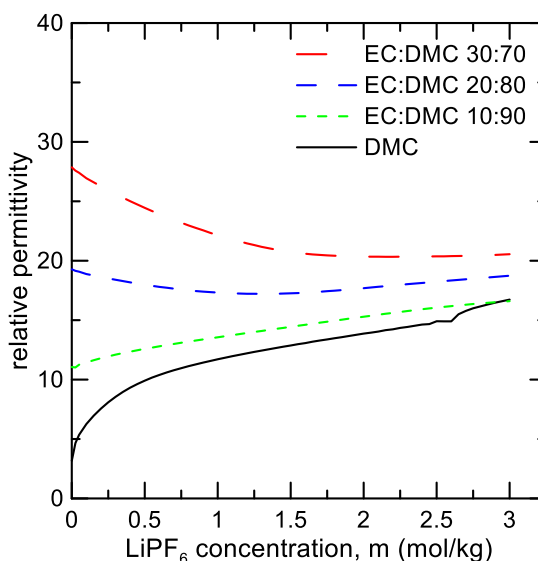
Figure 5.1: Relative solution permittivity as a function of $LiPF_6$ concentration as calculated by the AEM. Solvent blends based on DMC containing up to 30% EC by weight are shown.

5.2   CONDUCTIVITY AND VISCOSITY RESULTS

As was seen in Table 4.1, the melting point, dielectric constant, and viscosity of EC are all much higher than those of EMC and DMC. EMC and DMC have very similar chemical structures, and correspondingly their physical properties are similar except for the melting point of DMC which is comparatively high. Figure 5.2 shows viscosity measured as a function of temperature for EMC and DMC without any salt added. The

viscosity of EC shown at 40°C comes from Ref. 17. Calculations from the AEM for all three solvents are shown as solid lines. Note that the AEM calculations for the viscosity of EC extend beyond its freezing point (36.4°C). EMC and DMC have comparable viscosities over a wide range of temperatures. AEM calculations have excellent agreement with measured values.
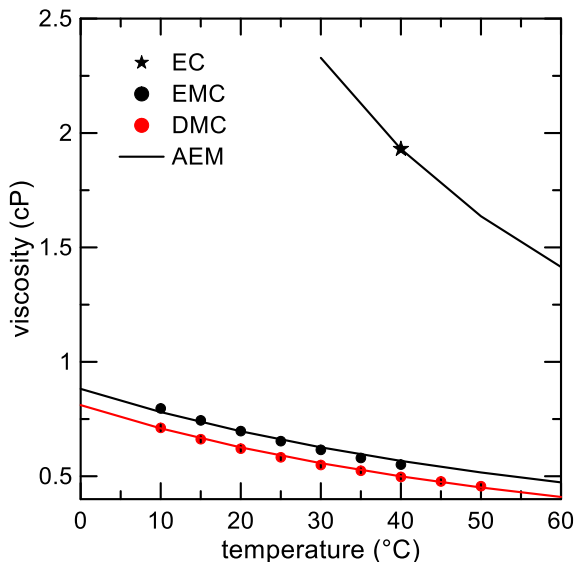
Figure 5.2: Viscosity as a function of temperature for carbonate solvents EC, EMC, and DMC. Data for EC is from Ref. 85. Calculations from the AEM are shown as solid lines.

A series of electrolytes with solvent blends based on either EMC or DMC have been made with increasing EC content to investigate the influence of EC on electrolyte properties. The solvent compositions of these electrolyte systems are: EC:EMC x:(100-x) and EC:DMC x:(100-x) with x = {0, 10, 20, 30} (wt. %) for both systems. Concentrations of LiPF$_6$ between 0 m and 2.0 m were considered. Figure 5.3 shows viscosity as a function of LiPF$_6$ concentration for electrolytes containing solvent blends (a) x = 0, (b) x = 10, (c) x = 20, and (d) x = 30 for temperatures between 10°C and 40°C. As may be expected from the high viscosity of EC shown in Figure 5.2, adding EC

increases the viscosity of the resulting electrolyte at all temperatures. This effect is most striking at high LiPF$_6$ concentrations. At 2.0 m LiPF$_6$, the viscosities of electrolytes with 30% EC (Fig. 5.3(d)) are double that of the corresponding EC-free electrolytes (Fig 5.3(a)). Similar effects are seen at other concentrations of LiPF$_6$.
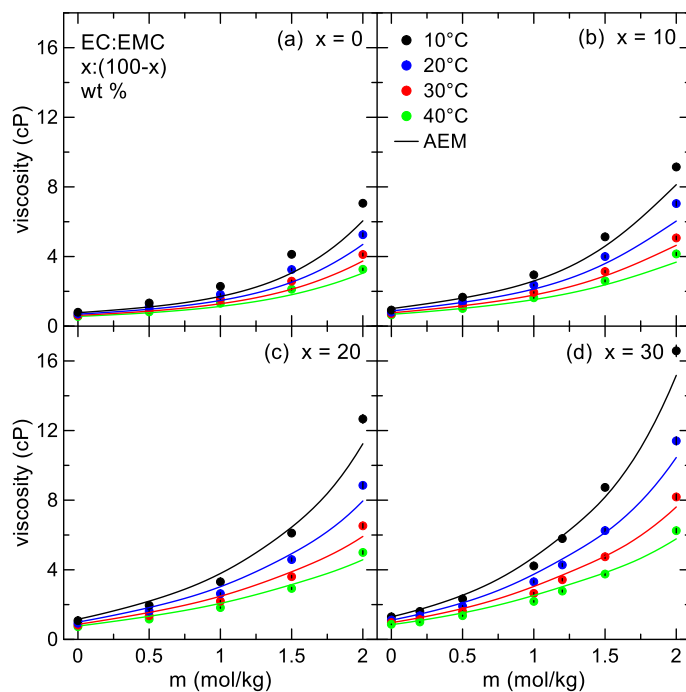
Figure 5.3: Viscosity as a function of LiPF$_6$ concentration for electrolytes with solvent blends (a) EMC, (b) EC:EMC 10:90, (c) EC:EMC 20:80, and (d) EC:EMC 30:70 (wt. %). Temperatures between 10°C and 40°C are shown. Calculations from the AEM are displayed over the experimental data as solid lines for comparison.

Similar trends are observed for electrolytes with solvents of the form EC:DMC x:(100-x). Figure 5.4 shows viscosity as a function of LiPF$_6$ concentration for electrolytes containing solvent blends with (a) x = 0, (b) x = 10, (c) x = 20, and (d) x = 30 for temperatures between 10°C and 40°C. Notice that over both temperature and salt concentration, the viscosities of these electrolytes are universally lower than the corresponding electrolytes containing EMC shown in Figure 5.3. Since DMC has a lower viscosity than EMC at all temperatures considered (as seen in Figure 5.2), this is to be

expected. As in the EC:EMC case shown in Figure 5.3, adding EC to DMC-based electrolytes significantly increases the viscosity. At the most extreme conditions of 10°C and 2.0 m LiPF$_6$, viscosity increases by 145% between 0% EC and 30% EC in DMC-based electrolytes. At more moderate conditions such as 1.0 m LiPF$_6$ and 20°C the increase in viscosity is still 69% over the same range of EC.
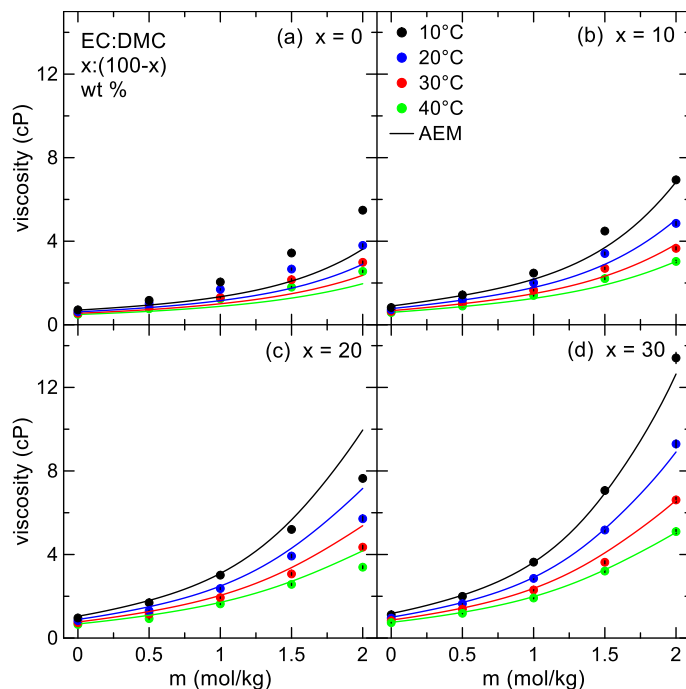
Figure 5.4: Viscosity as a function of LiPF$_6$ concentration for electrolytes with solvent blends (a) DMC, (b) EC:DMC 10:90, (c) EC:DMC 20:80, and (d) EC:DMC 30:70 (wt. %) for temperatures between 10°C to 40°C. Calculations from the AEM are shown as solid lines.

Viscosity calculations from the AEM for the EC:EMC-based and EC:DMC-based electrolytes are shown as solid lines in Figures 5.3 and 5.4, respectively. Generally, the agreement of AEM calculations with experiment is quite good; the average deviation from experiment over all solvent compositions, salt concentrations, and temperatures is 10.2%. As seen previously in different electrolyte systems[110], the AEM's viscosity predictions can deviate further from experiment at high concentrations of LiPF$_6$, where

the deviation may vary somewhat for a given system[8]. Here, the deviations of the AEM calculations from experimental measurements for the EC:EMC and EC:DMC systems shown in Figures 5.3 and 5.4 are 4.6%, 9.0%, 12.7%, 12.6%, and 12.3% for $LiPF_6$ concentrations of 0 m, 0.5 m, 1.0 m, 1.5 m, and 2.0 m, respectively.

One system that deserves particular attention is the case where DMC is the sole solvent. In this case, the agreement with the AEM is worse than that of EC:DMC systems for all concentrations of $LiPF_6$, apart from the salt-free case. For these DMC-only electrolytes, average deviations of the AEM from experimental viscosity measurements are 0.8%, 17.9 %, 29.5%, 33.4%, and 25.4% for 0 m, 0.5 m, 1.0 m, 1.5 m, and 2.0 m, respectively, over all temperatures. This larger deviation at non-zero salt concentrations appears to stem from an issue with how the AEM interprets the structure-making interactions between solvated ion associated members formed within mixtures of DMC and $LiPF_6$, which would have significant amounts of ion pair and triple ion species. Presumably this artifact is also present in the other DMC-containing electrolytes, however it becomes much less pronounced due to the increased presence of free ions enabled by the higher permittivity of EC. If the pure DMC electrolytes were removed from the evaluation of the AEM, the average deviation over all parameters becomes only 8.7%. Further efforts are underway to better understand the solvated state of ion associated species and incorporate those improved insights within AEM.

Figure 5.5 shows ionic conductivity as a function of $LiPF_6$ concentration for electrolytes with solvent compositions EC:EMC x:(100-x) (wt. %) for (a) x = 0, (b) x = 10, (c) x = 20, and (d) x = 30. Experimental data taken at temperatures between 0°C and 40°C are shown as closed circles with the color of each temperature indicated in panel

(b). The inset in panel (a) shows conductivity as a function of *molar* concentration of LiPF$_6$ for a lower concentration range. This data is reproduced from Ref. 104. Calculations from the AEM are shown as solid lines in all panels. As EC is added, the maximum conductivity (denoted κ_{max}) increases. As well, the LiPF$_6$ concentration at maximum conductivity (denoted c_{max}) decreases going from the EC-free electrolyte to 30% EC.
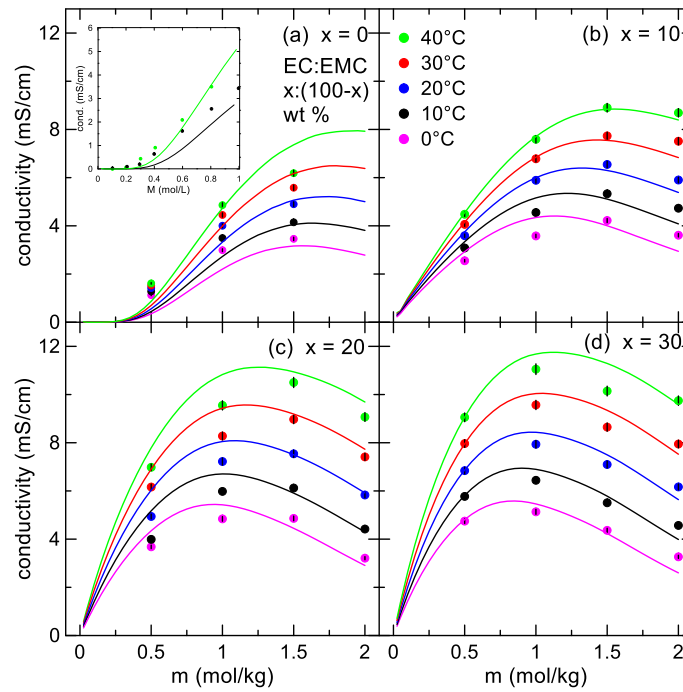
Figure 5.5: Ionic conductivity as a function of molal concentration of LiPF$_6$ for solvent combinations (a) EMC, (b) EC:EMC 10:90, (c) EC:EMC 20:80, and (d) EC:EMC 30:70 (wt. %). Temperatures between 0°C and 40°C are shown, and calculations from the AEM are given as solid lines. The inset Figure in panel (a) shows conductivity as a function of molar concentration of LiPF$_6$ between 0 and 1.0 mol/L for electrolytes containing EMC as the sole solvent. This data is obtained from Ref. 104. AEM calculations are given as solid lines.

The reason for this change in c_{max} as a function of EC content comes from the change in dielectric constant as a result of adding or removing EC. Recalling Figure 5.1, the impact of adding LiPF$_6$ on the overall dielectric constant of the solution depends on

its base EC content. Low-EC solutions see an increase in dielectric constant when salt is added, while 30% EC solutions experience so-called "dielectric depression" on the addition of salt. This will influence the value of c_{max}. For the EC-free electrolytes, a large amount of LiPF$_6$ must be added before the dielectric constant of the electrolyte is high enough for significant ion dissociation to occur. As a result, the conductivity maximum occurs at a higher salt concentration. Conversely, for high-EC electrolytes, the dielectric constant is reduced with added LiPF$_6$. This lower permittivity will lead to a slightly larger ion pair population, thus reducing the number of free single ions. This, combined with increasing viscosity, causes c_{max} to be lower when EC is present. At 20°C, κ_{max} (according to AEM calculations) for the electrolyte with EMC as the sole solvent is 5.2 mS/cm and occurs at approximately 1.75 m LiPF$_6$. For the electrolyte with the solvent blend EC:EMC 30:70 at the same temperature, κ_{max} is considerably higher, around 11.8 mS/cm, and occurs at a much lower LiPF$_6$ concentration of 1.1 m.

The temperature of the electrolyte also impacts c_{max}. The solubility of the solution and the viscosity are both temperature dependent. As temperature increases, for example, the viscosity will decrease, and the solubility will increase. This allows for more Li salt to be added to the solution before the increasing viscosity overpowers the addition of more charge carriers. The impact of temperature on c_{max} is much less dramatic than the amount of EC added. Similar trends in c_{max} and κ_{max} are seen at higher compositions of EC in Ding et al.[56].

Figure 5.6 shows ionic conductivity as a function of LiPF$_6$ concentration for temperatures between 0°C and 40°C for electrolytes composed of the solvent blend EC:DMC x:(100-x) for (a) x=0, (b) x=10, (c) x=20, and (d) x=30. The conductivities of

DMC-containing electrolytes are universally higher than the corresponding EMC-containing electrolytes in Figure 5.5. Again, this must be due to the slightly lower viscosity of DMC compared to EMC. Similar trends in conductivity are seen between the two classes of electrolytes. As EC is added, κ_{max} increases and c_{max} decreases for the DMC-containing electrolytes. Comparing to Figure 5.5, κ_{max} at 20°C for the electrolyte containing DMC as the sole solvent is about 9.0 mS/cm and occurs at 2.0 m LiPF$_6$. For the EC:DMC 30:70 electrolyte, κ_{max} at 20°C is 11.8 mS/cm at a concentration of 1.1 m. For EMC-containing electrolytes (Figure 5.5), the conductivity almost doubles between 0% EC and 30% EC, while in the DMC case the conductivity only increases by about 30%.
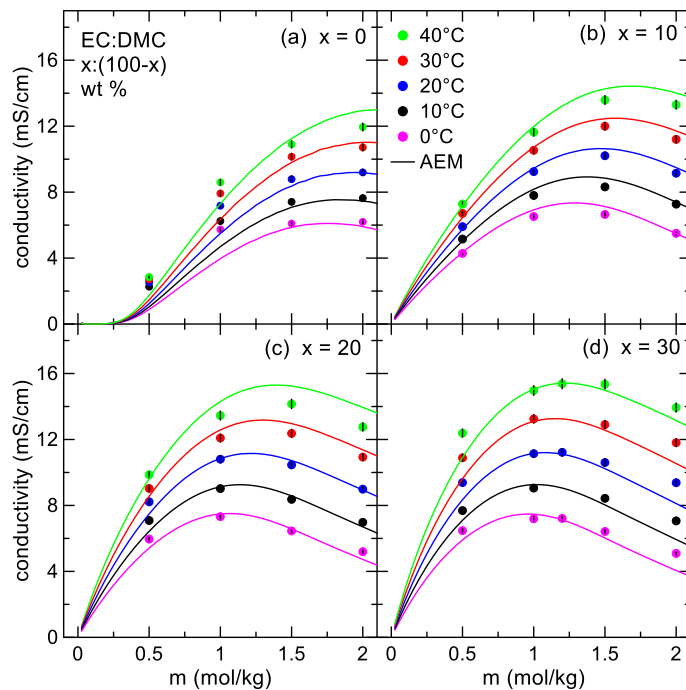
Figure 5.6: Ionic conductivity as a function of LiPF$_6$ concentration for electrolytes containing solvent mixtures (a) DMC, (b) EC:DMC 10:90, (c) EC:DMC 20:80, and (d) EC:DMC 30:70 (wt. %) for temperatures between 0°C and 40°C. Calculations from the AEM are shown as solid lines.

Electrolytes containing only linear carbonate solvents EMC or DMC (Figures 5.5 (a) and 5.6 (a)) show extremely low conductivities when $[LiPF_6] \leq 0.5$ m. The electrolytes containing EC do not show this behaviour. The non-linear increase in conductivity can be seen more closely in the inset in Figure 5.5 (a). This has been shown to be due to the low dielectric constants of EMC and DMC (see Table 4.1). $LiPF_6$ cannot dissociate into its constituent ions readily in the low dielectric environment of EMC or DMC, and instead it exists as neutral ion pairs (IP) that do not contribute to the conductivity of the solution[103,104,112,113]. At higher concentrations of salt, the presence of ion pair dipoles causes an increase in permittivity of the solution enough to promote the existence of charged single ions (SI) and triple ions (TI), and as a result the conductivity increases[113]. Higher concentrations of Li salt have also been shown to lead to lower impedance growth and altered compositions of the SEI layer on both the cathode and the anode for cells with electrolytes composed of EC:EMC 30:70 and different additives[114]. For cells containing only EMC in the electrolyte, a slight increase in cell impedance is seen when salt concentration is increased[104]. Additionally, the increased cost of using higher salt concentrations must be considered in potential industrial applications. When EC is present in the electrolyte, the Li salt can dissociate at lower concentrations. This has long been known, but with the increased interest in EC-free electrolytes, it is important to revisit the problems of low dielectric solvents such as EMC and DMC and ensure that they are addressed in any commercial EC-free electrolytes.

The modest decrease in viscosity that is seen from removing EC in Figures 5.3 and 5.4 does not make up for the conductivity "lost" by removing the high-dielectric solvent. For applications where high conductivity is necessary such as for high power

cells, it may be necessary to operate cells with EC-free electrolytes at higher concentrations of salt, up to 1.5 m or even 2.0 m. Additionally, even when extremely high conductivity is not necessary, a higher salt concentration will ensure that a catastrophic drop in conductivity will not occur from either salt consumption or concentration gradients that form during cycling.

Conductivity calculations from the AEM are shown in Figures 5.5 and 5.6 as solid lines. The AEM can capture the trends in conductivity for low-EC and EC-free electrolytes. The average disagreement between AEM and experiment over all temperatures, salt concentrations, and solvent compositions is 11.1%. Unlike with the viscosity results, the AEM's conductivity calculations do not deviate further from experiment at high $LiPF_6$ concentration. The average deviations from experiment at 0.5 m, 1.0 m, 1.5 m, and 2.0 m are 18.5%, 9.1%, 4.8%, and 9.3%, respectively. In most cases the locations of the conductivity maxima are well predicted. The largest deviation from experiment is seen for the case of 0.5 m $LiPF_6$ in DMC, so a big contribution to the overall disagreement comes from situations with low salt content and low permittivity solvent systems. For low permittivity systems under conditions of low salt concentration there is a profound change in the permittivity landscape as the salt concentration is increased, and subtle changes in solution permittivity can make a relatively large change in free ion populations (starting from practically zero) and in the small values of conductivity. These trends are captured by the AEM, which can further be used to diagnose behavior of ion association in low-permittivity electrolytes.

5.2.1 Walden plots

In Chapter 2, it was shown that a simple expression for conductivity can be derived assuming that the drag force on migrating ions in the electrolyte obeys Stokes' Law[47,59,110]. The resulting expression for ionic conductivity is found in Equation 2.9. By making some slight modifications to Equation 2.9, an expression is obtained that resembles the empirical Walden Rule

$$\log \Lambda = \log \frac{Kf}{R} + \log \frac{1}{\eta} \qquad (5.1)$$

In Equation 5.1, K is a constant, f is the molar ratio of free ions in solution to the amount of salt added, and R is the harmonic mean of the Stokes radii of the individual ions in solution r_+ and r_- (assuming a 1:1 salt). The full derivation for Equation 5.1 is found in Chapter 2. Walden plots have been used extensively to evaluate the ionicity (i.e. the degree of dissociation) of ionic liquids[59-65]. Less frequently, Walden analysis has been applied to non-aqueous organic solvent-salt electrolytes[66,67]. Figure 5.7 shows $\log \Lambda$ versus $\log 1/\eta$ for electrolytes previously presented in Figures 5.3-5.6. LiPF$_6$ concentrations of 0.5 m, 1.0 m, and 2.0 m are shown, all at 20°C. Solid lines are drawn between data points of related solvent composition for a given LiPF$_6$ concentration. Different symbol types specify unique solvent compositions. The dashed line is a linear fit to the points that have solvent blends containing 30% EC by weight (open and closed rhombi symbols).
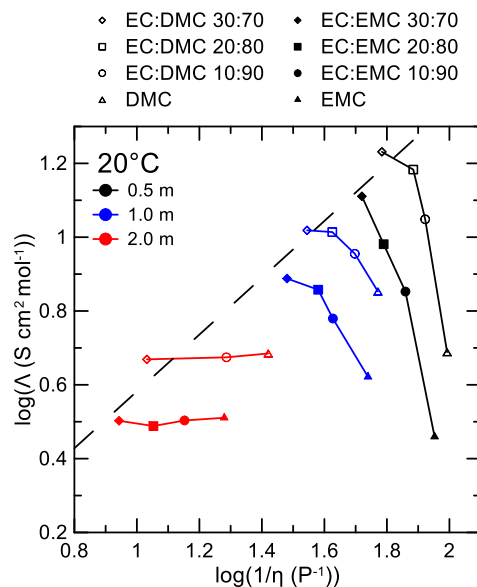
Figure 5.7: Walden plot for the different electrolyte systems considered in this work for different concentrations of $LiPF_6$. All data shown are at 20°C. Solid lines are used to connect electrolytes of related composition. Different solvent mixtures are specified by plotting symbol. The dashed line is a linear fit to all points with 30% EC by weight in the solvent mixture.

In Chapter 4 it was shown that electrolytes with solvent systems composed of 30% EC and different ratios of EMC, DMC, and MA had roughly the same ionicity and Stokes radius independent of $LiPF_6$ concentration and temperature[110]. Therefore, the dashed line in Figure 5.7 specifies a region in the Walden plot of constant ionicity and Stokes radius. Deviations from this line are indicative of a variation of one or both quantities. As EC is removed from the electrolyte, the points move further away from the line of constant ionicity. This move is most dramatic at lower concentrations of $LiPF_6$ (0.5 m), where the molar conductivity drops by almost an order of magnitude between the 30% EC and EC-free electrolytes. Referring to Equation 5.1, this drop represents a quantity of conductivity that is "lost" by changing the ratio of solvents involved. Under circumstances where the ionicity and Stokes radius of the electrolyte are stable over

different solvent compositions, a decrease in viscosity (or increase in fluidity ϕ, where $\phi \equiv \eta^{-1}$) should correspond to an increase in molar conductivity. However, as has been discussed regarding Figures 5.5 and 5.6, replacing EC with low-dielectric solvents leads to significantly more ion pairing, which in turn dramatically lowers the conductivity due to the resulting lower populations of ionic species, even though the viscosity is decreased (Figures 5.3 and 5.4). Electrolytes with low dielectric constants fall well below the expected conductivity due to the increase in ion association, and possibly also a change in Stokes' radius. The Walden plot explicitly illustrates how the composition of EC in the electrolyte impacts the resultant ionic conductivity and can act as a guide to explain the lower conductivity in low-EC electrolytes.

Figure 5.8 shows Walden plots using data calculated from the AEM for (a) EC:EMC-based and (b) EC:DMC-based electrolytes. The "ideal" KCl line (see Chapter 4) with a slope of 1 and a y-intercept of 0 is shown in both (a) and (b) as a solid line for reference. Traditionally, this line has been used in Walden plots to specify a region on the plot where the salt is fully dissociated[61,62,65,67]. For electrolytes containing high concentrations of EC in the solvent blend (>20% by wt.), the Walden rule is obeyed. These electrolytes have a slope of approximately 1 for a range of $LiPF_6$ concentrations between 0 and 3 m. As the fraction of EC in the electrolyte is decreased, the data from the AEM begin to deviate from the Walden rule at low concentrations of salt. As well, for all concentrations of $LiPF_6$, as the fraction of EC is lowered, the data start to shift downwards, suggesting an overall lower iconicity in electrolytes with lower EC contents. For electrolytes containing solely EMC or DMC (x = 0), the conductivity is extremely low at very low concentrations of salt (again, refer to Figs. 5.5(a) and 5.6(a)), which

corresponds to a sharp deviation from ideal Walden behaviour. As discussed above, this deviation can be attributed to a high degree of ion pairing at low LiPF$_6$ concentrations in low-dielectric solvents. As more LiPF$_6$ is added, the relative solution permittivity of the electrolyte increases sufficiently for more salt species to dissociate (Figure 5.1), and the Walden rule is again obeyed. These observations from the AEM agree with what has been seen experimentally in Figure 5.7.
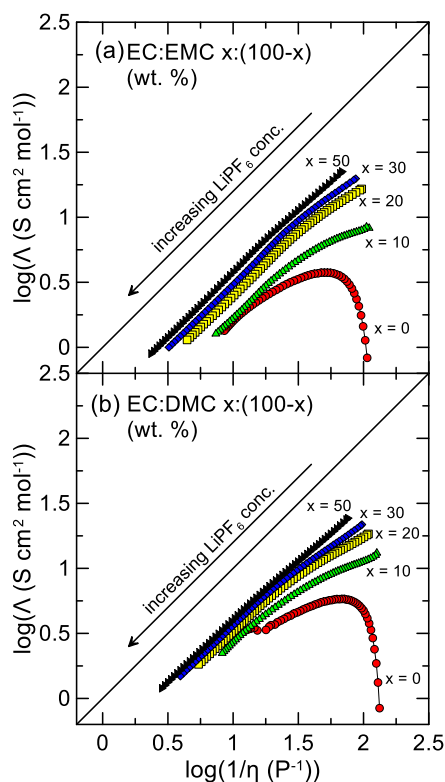
Figure 5.8: Walden plots for (a) EC:EMC:LiPF$_6$ electrolytes, and (b) EC:DMC:LiPF$_6$ electrolytes as calculated by the AEM at 20°C. The solid line represents the "ideal" KCl line.

From Equation 5.1, the drop in molar conductivity as EC is removed can be attributed either to a lower ionicity or an increased solvated ion size, or both. Without further information about the system, it is not possible to distinguish between a change in Stokes radius or a change in the degree of dissociation, according to Equation 5.1. As

seen in Figures 5.5 and 5.6, and discussed above, low-EC electrolytes will experience a significant amount of ion pairing, especially at low concentrations of $LiPF_6$. However, it remains to be seen how much of an impact the solvated ion sizes will have on the resultant conductivity of these electrolytes.

The AEM provides calculations of solvated diameters for both the cations and anions in the electrolyte solution. Figure 5.9 shows the solvated diameters of Li^+ and PF_6^- as a function of EC concentration in an electrolyte containing the solvents EC and DMC, as calculated by the AEM. $LiPF_6$ concentrations of 0.5 m, 1.0 m and 2.0 m are shown. The solvated diameters of both ions decrease as more salt is added. This is due to increased competition for solvent molecules when more salt is present. However, for a given concentration of $LiPF_6$ the solvated diameters are relatively unchanged as a function of EC content. This observation is explained as follows: if the molecular volumes of different solvents are about the same and they have the same core moieties (e.g., carbonates), then the effective solvated diameter around lithium will be similar, but also may differ due to difference in solvation structure. The high surface charge density of the small lithium ion helps drive this general outcome. Lastly, it would be expected that the placement of data on a Walden plot will depend somewhat on the solvated ion sizes from Equation 5.1.

Although the solvated diameters in Fig. 5.9 do not show significant change over EC content and modest decrease over salt concentration, it is the extent of ion solvation past the bare ion baseline that partially contributes to the *offset* of the data from the ideal KCl line. Note that for aqueous KCl the constituent K^+ and Cl^- are sparingly solvated such that their effective transport diameters are close to the bare ion values.
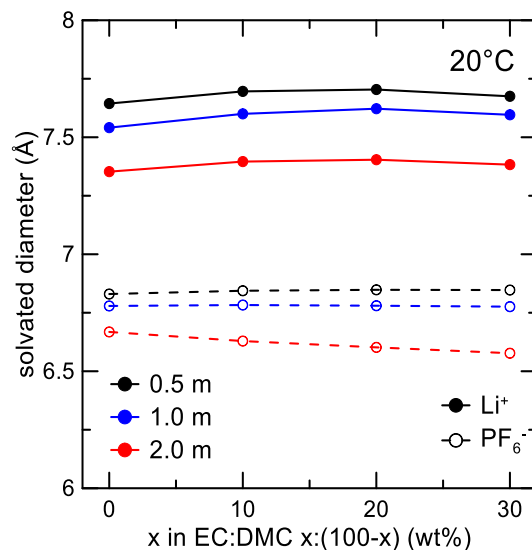
Figure 5.9: Solvated ion diameters of Li^+ and PF_6^- as a function of EC content (wt. %) in an EC:DMC-based electrolyte as calculated by the AEM. Results are shown at 20°C for $LiPF_6$ concentrations of 0.5 m, 1.0 m, and 2.0 m.

Figure 5.10 shows AEM results for single ion (SI), ion pair (IP), and triple ion (TI) populations at 20°C for (a) 0.5 m $LiPF_6$, (b) 1.0 m $LiPF_6$, and (c) 2.0 m $LiPF_6$ as a function of the EC content (wt. %) in an electrolyte with a solvent mixture of EC and DMC. The SI populations presented here are the sum of individual Li^+ and PF_6^- populations. Overall, the number of triple ions is very low, making up no more than 2% of the total population of salt over all conditions considered. The AEM predicts a large percentage of ion pairs for electrolytes with low concentrations of EC. In the most extreme case, at 0.5 m $LiPF_6$ and 0% EC, the mole fraction of ion pairs in the electrolyte is 0.90. The population of ion pairs becomes insignificant as EC is added. AEM calculations in Figures 5.9 and 5.10 suggest that ion association is the primary reason for the drop in conductivity observed in low-EC electrolytes, and seen clearly in Figures 5.7 and 5.8. The change in the Stokes radii of the ions in solution has little or no impact on the conductivity as a function of EC content.
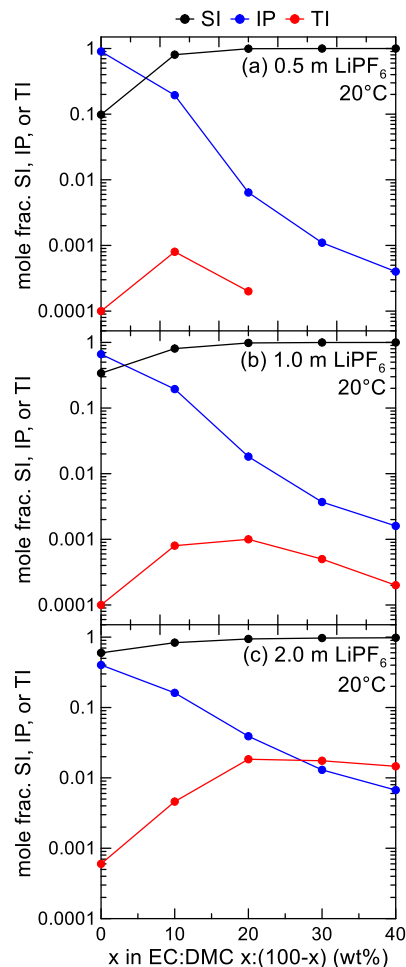
Figure 5.10: AEM calculations for single ion (SI), ion pair (IP), and triple ion (TI) populations at 20°C (given as a mole fraction) as a function of EC content in electrolytes containing EC and DMC. The SI populations shown are the sum of individual Li^+ and PF_6^- populations. $LiPF_6$ concentrations of (a) 0.5 m, (b) 1.0 m, and (c) 2.0 m are shown.

5.3   EC:DMC:LiPF₆ PHASE DIAGRAM

Considerable progress has been made toward understanding the phase diagrams of electrolytes consisting of Li salts such as LiFSI, Li bis(trifluoromethylsulfone)imide (LiTFSI), Li bis(perfluoroethanesulfonyl)imide (LiBETI), Li perchlorate (LiClO₄), Li tetrafluoroborate (LiBF₄), Li difluoro(oxalato)borate (LiDFOB), and Li bis(perfluoroethanesulfonyl)imide (LiBETI). These salts have been studied in solvents

124

such as acetonitrile (AN) and dimethoxyethane (glyme or DME)[115-119]. However, the liquid-solid equilibria of $LiPF_6$ in carbonate solvents have not been considered in such detail. Recently, Xiong et al. determined the phase diagram of the $DMC:LiPF_6$ system using differential thermal analysis (DTA)[120].

Here, DTA was used to investigate the phase behaviour of the ternary $EC:DMC:LiPF_6$ system. The phase equilibria of the salt-free system have been well-studied by Ding et al.[17,24,85,121,122], and Ding et al. showed results for $LiPF_6$-containing solutions for a single composition of $EC:EMC$[85]. Okumura and Horiba demonstrated melting point depression when $LiPF_6$ is added to the single solvent systems EC, EMC, and DMC, but two-solvent systems such as EC:DMC were not considered[123]. Figure 5.11 shows the raw DTA traces for EC:DMC solutions with (a) 0 m, and (b) 1.0 m $LiPF_6$ added. Converted to a weight percent, the 1.0 m electrolytes in panel (b) correspond to 15.2% $LiPF_6$. The curves in Figure 5.11(a) are typical of a binary eutectic system. The pure DMC curve shows a single peak corresponding to the melting point of DMC. As EC is added, a second feature emerges. For the EC:DMC 10:90 and 20:80 samples, solid DMC exists alongside liquid between the solidus and liquidus peaks. The composition EC:DMC 30:70 is close to the eutectic point of the system, so only a single feature is observed. The ternary system in Figure 5.11(b) is much less simple. For solvent compositions away from the binary eutectic point (i.e. EC:DMC 10:90 and EC:DMC 20:80), a third feature emerges between the solidus and liquidus peaks. These three features are labeled for the EC:DMC 20:80 + 1 m $LiPF_6$ DTA curve in Figure 5.11(b). It is unclear at this time what this third feature represents.
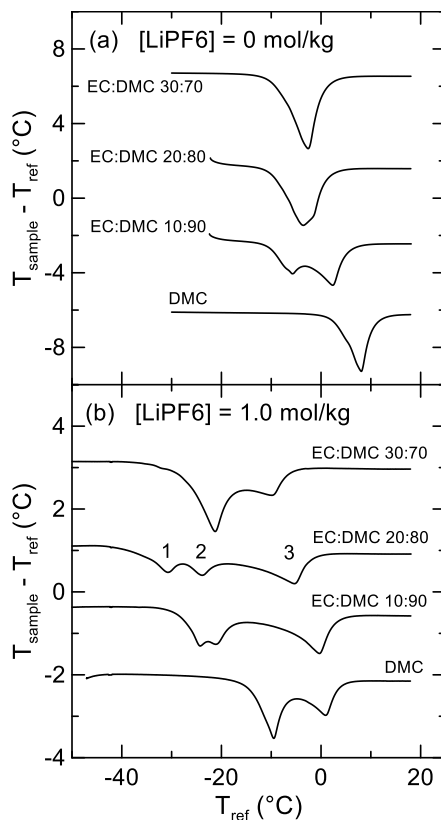
Figure 5.11: Differential thermal analysis (DTA) traces for electrolytes containing solvent mixtures EC:DMC x:(100-x) (wt. %) with $LiPF_6$ concentrations (a) 0 m and (b) 1.0 m. The DTA traces are shifted on the y-axis for clarity. For the three-component system in panel (b), three distinct features are identified and are labelled for the EC:DMC 20:80 case.

Figure 5.12 shows partial phase diagrams for the ternary $EC:DMC:LiPF_6$ system for (a) 0 m $LiPF_6$, and (b) 1.0 m $LiPF_6$, plotted as a function of the weight percent of EC in the solution. In Figure 5.12(a), results from Ref. 85 are also given for comparison. The three sections of the phase diagram in Figure 5.12(b) correspond to the three features of the DTA trace as labelled in Figure 5.11(b). The phase diagram for the salt free system in Figure 5.12(a) agrees well with the results of Ding et al. The solidus line occurs slightly lower in the phase diagram determined here, but the melting point of pure DMC and the EC:DMC eutectic point as determined here agree quite well with the data from Ref. 85.

126

In both the salt-free and 1.0 m $LiPF_6$ cases, the addition of EC depresses the liquidus point of the system. In both cases the liquidus point drops by nearly 10°C between solvent compositions with 0% EC and 30% EC. The addition of $LiPF_6$ to the system further depresses the liquidus line in the phase diagram at compositions with low-EC content. This agrees with the results of Okumura and Horiba for single solvent systems[123]. For solutions close to the binary eutectic for the EC:DMC system (~30% EC), the difference in the liquidus point between Figure 5.12(a) and 5.12(b) is minimal.

It should be of interest to obtain phase diagrams for a wider range of $LiPF_6$ concentrations. During operation of a Li-ion cell, high currents can cause gradients in the Li salt concentration in the cell, which will lead to local variations in the phase behaviour of the electrolyte. The high melting point of DMC is particularly worrying. For all combinations studied here, the liquidus line of the phase diagram is above -10°C. Even for the salt-containing solutions, solid precipitates will exist at temperatures below this point.

Today, many commercial cells use electrolyte formulations with high concentrations of DMC. Commercial cells opened in this lab have been found to have electrolytes with solvent compositions containing up to 80% DMC. Ambient temperatures of -10°C or below are common in the winter months in many locations around the world. Operation of Li-ion batteries in EVs or other larger-scale applications may become difficult in these climates when high-DMC cells are used. One solution may be to add a ternary or even quaternary solvent to the electrolyte. It has been shown in previous studies that electrolytes containing ternary or quaternary mixtures of carbonates can operate well at low temperature[23-27]. It will be important to consider the relatively

high melting points of high-DMC content electrolytes in the future development of Li-ion cells, especially for automotive or grid-scale energy storage applications.
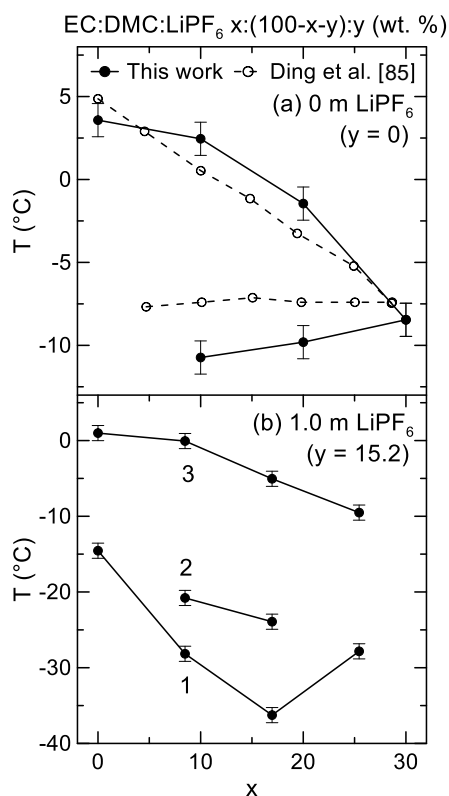
Figure 5.12: Phase diagrams for the EC:DMC:LiPF$_6$ system for (a) 0 m LiPF$_6$, and (b) 1.0 m LiPF$_6$. Results for the salt-free system are compared to differential scanning calorimetry (DSC) results obtained from Ref. 85. In panel (b) the three parts of the phase diagram reflect the three distinct features identified in Figure 5.11.

5.4   CYCLING DATA

Ma et al. found that adding up to 5% of an enabling compound to EC-free electrolytes significantly improves high voltage cycling of Li-ion cells[45]. These enabling compounds form passivating solid electrolyte interphase (SEI) layers on the surface of the graphite negative electrode. Since EC has good SEI-forming properties as well, its suitability as an enabler was tested in a previous work[28]. However, it was found that it did not perform nearly as well as other enabler candidates[28,45]. One of the best enablers for EC-free

electrolytes was fluoroethylene carbonate (FEC). Figures 5.13(a) and (b) show normalized capacity as a function of cycle number for cells with the electrode formulations NMC442/graphite, and single crystal NMC532/graphite, respectively. Figures 5.13(c) and (d) show voltage hysteresis versus cycle number for NMC442/graphite, and NMC532/graphite cells, respectively. The NMC442 cells were charged/discharged at a rate of C/2.5, and the NMC532 cells were charged and discharged at C/2. Three different solvent formulations were considered: EC:EMC 30:70 (wt. %), FEC:EMC 5:95 (wt. %), and pure EMC. Each electrolyte contained 1 M LiPF$_6$. No additional electrolyte additives were used in these cells. Two cells were made for each electrolyte composition to test for reproducibility. Figures 5.13(b) and (d) only show NMC532 cells with the FEC:EMC 5:95 electrolyte. The cycles with higher normalized capacity and lower voltage hysteresis correspond to C/20 cycles, as labeled in Figure 5.13, which occurred once every 50 cycles. In Figure 5.13(a), the capacity fade is comparable for cells with electrolytes containing EC:EMC 30:70 and 100% EMC. For these cells, about 10% of their original capacity is lost after less than 100 cycles. This is reproducible for the pair cells of each type. The cells containing the electrolyte with FEC:EMC 5:95 perform much better at high voltage. Very little capacity fade is seen after over 500 cycles. In Figure 5.13(c), cells containing solvents EC:EMC 30:70 and 100% EMC show much higher impedance growth than the cells with FEC:EMC 5:95. For the NMC532 cells, almost 85% of the original capacity is retained after 3000 cycles, as seen in Figure 5.13(b). The impedance growth in these cells after 3000 cycles is comparable to the NMC442 cells after just 500 cycles. EC-free electrolytes can cycle extremely well at high voltage, and the addition of FEC or other film-forming enablers is

crucial for long-term operation of cells with EC-free electrolytes. The impact of FEC on the transport properties of EC-free electrolytes was not studied in this thesis. However, Reference 120 gives a good evaluation of the conductivity of FEC:EMC 5:95 and FEC:EMC 10:90 electrolytes. Due to the high dielectric constant of FEC, it gives a boost to the ionic conductivity much like EC, but without the adverse effects on cycling performance at high voltage.
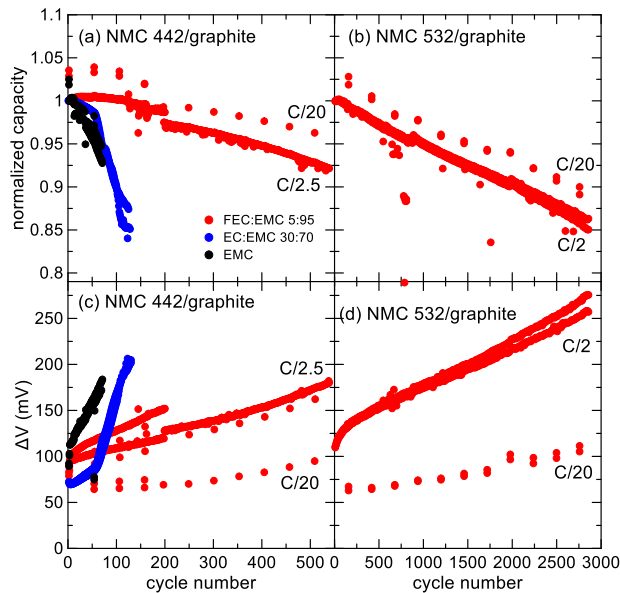
Figure 5.13: Normalized capacity versus cycle number for (a) Li[Ni$_{0.4}$Mn$_{0.4}$Co$_{0.2}$]O$_2$ (NMC442)/graphite pouch cells, and (b) single crystal Li[Ni$_{0.5}$Mn$_{0.3}$Co$_{0.2}$]O$_2$ (NMC532)/graphite cells, and voltage hysteresis versus cycle number for (c) NMC442/graphite cells and (d) NMC532/graphite cells. The NMC442 cells were cycled between 2.8 and 4.4 V at a rate of C/2.5 for both charge and discharge. The NMC 532 cells were cycled between 4 and 4.4 V at a rate of C/2. Both types of cells had a cycle at C/20 every 50 cycles. Different electrolyte solvent compositions are shown. For all cells the electrolyte contains 1.0 M LiPF$_6$. Two identical cells were made for each unique electrolyte. In panels (b) and (d), only every 10th cycle is displayed.

5.5 CONCLUSION

In this chapter, the transport properties of low-EC and EC-free carbonate-based Li electrolytes were considered. Ionic conductivity and viscosity were measured for electrolytes containing solvent blends of the form EC:EMC x:(100-x) and EC:DMC x:(100-x) (wt. %) for x = {0, 10, 20, 30}. Due to the profound effect of solution permittivity on the resulting transport properties of the electrolytes, the EC content had a huge impact on the resulting conductivity, while the viscosity behaved as expected. Extremely low values for conductivity were observed at low $LiPF_6$ concentrations for electrolytes containing EMC or DMC as the sole solvent. This was attributed to a large amount of ion pair formation. As well, low-EC electrolytes had lower maximum conductivities, with the maximum occurring at higher $LiPF_6$ concentrations. Calculations from the Advanced Electrolyte Model (AEM) agree well with experimental data, with challenging cases noted in viscosity predictions for electrolytes with DMC or EMC as the sole solvent. Walden plots prove to be useful tools to describe the lower conductivity due to ion pairing in low-dielectric electrolytes. AEM results confirmed that the contribution of solvated ion size to the change in conductivity in low-EC electrolytes is minimal.

A phase diagram for the ternary $EC:DMC:LiPF_6$ system was constructed for a limited range of values. The liquidus transition for high DMC systems containing salt is lower than the corresponding salt-free system, but it is still high enough to cause concern for low temperature applications.

Cycling data for NMC442/graphite and single crystal NMC532/graphite cells charged to 4.4 V showed that cells containing EC-free electrolytes can cycle well at high voltage, with very little capacity fade after many cycles. The best performing electrolyte

investigated here contained 5% of the film-forming enabler fluoroethylene carbonate (FEC). NMC442 Cells containing EMC:FEC 95:5 showed less capacity fade and lower impedance growth over ~500 cycles than cells containing EC and cells without the enabler. NMC532 cells retained 85% of their original capacity after 3000 cycles, with comparable impedance growth to the NMC442 cells.

CHAPTER 6   CONCLUSION

The goal of this thesis was to study the transport properties of several non-traditional non-aqueous electrolytes for Li-ion batteries. Chapter 4 focused on alternative ester or nitrile co-solvents to improve the conductivity of well-known carbonate-based electrolytes. The impact of different solvents was studied using temperature-dependent conductivity and viscosity measurements. Initial tests of the different co-solvents found that almost all solvents considered had lower viscosities than either EMC or DMC, which themselves are meant to be "low-viscosity" co-solvents to enable operation of Li-ion cells with EC. This trend in viscosity was reflected in full Li electrolytes, in which electrolytes containing 20% w/w of a given co-solvent were added to a control electrolyte with a solvent blend made up of EC:EMC:DMC 25:5:70 (v/v). Electrolytes containing either ester or nitrile co-solvents had lower viscosities over all temperatures than the control electrolyte.

This trend was not reflected in conductivity, however. Only the co-solvents propionitrile (PN), methyl acetate (MA), isobutyronitrile (iBN), ethyl formate (EF), ethyl acetate (EA), and methyl formate (MF) improved the conductivity over the control electrolyte. While few cycling results have been published for electrolytes containing nitriles, there are several works that show cycling of Li-ion cells containing esters[30,35,37-30]. Therefore, the ester that gave the greatest gain in conductivity, MA, was chosen for further systematic study.

To study the impact of MA on the transport properties of Li electrolytes, solutions with solvent blends EC:EMC:MA and EC:DMC:MA x:(70-x):x, with x = {0, 10, 20, 30} (wt. %) were prepared with salt concentrations ranging from 0 to 2.0 mol/kg (m). From

here, ionic conductivity and viscosity were measured for this set of electrolytes. It was found that viscosity increased with salt concentration and decreased with temperature, as expected. Also expected based on the viscosities of the pure solvents was that the viscosity of the electrolyte would decrease with the addition of MA, which was indeed observed in practice. In both EC:EMC:MA and EC:DMC:MA-based electrolytes, solutions with 30% MA had the lowest viscosity. This decrease in viscosity led to a corresponding increase in conductivity. Electrolytes containing MA had higher conductivities than their ester-free counterparts. This trend was observed over all parameters, including temperature and salt concentration. Modifying the solvent composition by replacing EMC or DMC with MA also slightly shifted the concentration at maximum conductivity, c_{max}, most likely due to the slightly higher dielectric constant of MA compared to EMC and DMC.

The measured transport property data were analyzed according to the simple Stokes' Law model of conductivity introduced in Chapter 2. For all concentrations, temperatures, and solvent compositions, plots of κ vs $1/\eta$ showed good agreement with the expected linear trend. This suggests that the increase in conductivity observed on the addition of MA is primarily due to the decrease in viscosity rather than other factors such as increased salt dissociation or smaller solvated ion sizes (Stokes radii). Further, by plotting $\log \Lambda$ vs $\log 1/\eta$ (also called a Walden plot), it was suggested that the degree of salt dissociation and solvated ion sizes stay relatively constant over solvent composition, temperature, and $LiPF_6$ concentration, at least for this class of electrolytes. This provided more evidence that the increase in conductivity is primarily driven by the reduction in viscosity in these systems.

Finally, high rate cycling data for $Li[Ni_{0.5}Mn_{0.3}Co_{0.2}]O_2$ (NMC532)/graphite cells was presented, comparing electrolytes with different fractions of MA. Cells that did not contain MA experienced catastrophic capacity loss at high charge rate (~1.5 C and above). Meanwhile, cells containing as little as 20% MA showed almost no capacity fade at charge rates as high as 2 C. This showed that the decreased viscosity in MA-containing carbonate-based Li electrolytes translates to greatly improved performance under high charge rate in full Li-ion cells.

In Chapter 5, the transport properties of organic carbonate electrolytes containing low proportions of EC were considered. A similar procedure to that in Chapter 4 was followed: viscosity and ionic conductivity were measured for electrolytes with solvent compositions of the form EC:EMC and EC:DMC x:(100-x), with x = {0, 10, 20, 30} (wt. %), for $LiPF_6$ concentrations ranging from 0 to 2.0 m. As EC was removed from the electrolyte, the viscosity of the solution was reduced due to the extremely high viscosity of EC, as expected. However, this decrease in viscosity did not lead to a corresponding increase in conductivity as was seen in Chapter 4. Instead, with decreasing EC content in the electrolyte, the maximum conductivity κ_{max} decreased, and c_{max} increased rather dramatically. The decrease in κ_{max} was attributed to a significantly higher degree of ion association in low-EC and EC-free electrolytes, based on previous studies of conductivity in low-dielectric systems[104,112,113]. The larger c_{max} for low-EC electrolytes was due to the changes to the permittivity environment of the solution as salt was added; in the low dielectric solvent, adding salt increased the overall dielectric constant of the electrolyte, allowing more salt to be dissociated at higher concentrations of $LiPF_6$.

Like in Chapter 4, Walden plots were used to assess the degree of salt dissociation of the electrolytes studied in Chapter 5. Using Equation 2.13 developed in Chapter 2, the relative positions of points in the $\log \Lambda$ vs $\log 1/\eta$ space were interpreted in terms of degree of dissociation and Stokes radii of ions in solution. Electrolytes with low concentrations of EC showed large deviations away from the points considered to have constant ionicity. This indicated a combination of increased ion association and increased Stokes radii. To deconvolute these two effects, calculations from the AEM were used to help interpret the findings of the Walden analysis. AEM calculations showed the solvated radii of both Li^+ and PF_6^- were unchanged as a function of EC content in the electrolyte. This led to the conclusion that the position of low-EC electrolytes on the Walden plot was primarily due to high association rather than changes in solvated ion sizes.

Next, a simple preliminary phase diagram for the ternary system $EC:DMC:LiPF_6$ was constructed using differential thermal analysis (DTA). Solvent compositions EC:DMC x:(100-x), with x = {0, 10, 20, 30} (wt. %), were considered, with $LiPF_6$ concentrations of 0 and 1 m, corresponding to 0% and 15.2% by weight, respectively. The salt-free binary solvent system EC:DMC is already well-understood thanks to the work of Ding et al.[17,85,121], and the salt-free compositions tested here agree well with this previous work. Adding salt to the system depresses the liquidus transition temperature considerably for low-EC compositions. There is also a very large depression of the solidus transition for all solvent compositions. In addition, a third peak in the DTA trace was identified for electrolytes with 1 m $LiPF_6$, and x = 10 or x = 20. Without further information, or a more detailed phase diagram, the exact physical meaning of these additional features could not be elucidated. This phase diagram showed that the liquidus

transition for salt-containing systems with high DMC is quite high, and well within the range of colder climates (such as Canada) where electric vehicles and grid storage systems hope to operate, which was a potentially worrying finding.

Long term cycling data was presented for cells charged to high voltage (4.4 V). Two different cell chemistries were considered: $Li[Ni_{0.4}Mn_{0.4}Co_{0.2}]O_2$ (NMC442)/graphite cells and single crystal NMC532/graphite cells. These cells were charged and discharged at moderate rates (C/2.5 for NMC442 cells, C/2 for NMC532 cells). NMC442 cells that had EC in the electrolyte showed rapid capacity fade, reaching ~85% of their original capacity after only 100 cycles. These cells also showed large impedance growth during cycling. Cells with EMC as the sole solvent showed similar behaviour. However, in cells with electrolytes composed of 95% EMC and 5% of an enabling compound - in this case FEC - very little capacity fade was seen after many cycles. The NMC532 cells reached 85% of their original capacity just shy of 3000 cycles. This showed that it is both possible and practical to use EC-free electrolytes in high voltage Li-ion cells. However, for high rate applications, the decrease in conductivity from higher ion association as EC is removed must be taken into consideration for electrolytes of this type.

For the electrolyte transport properties presented in Chapters 4 and 5, corresponding calculations from the Advanced Electrolyte Model (AEM) were shown. For the MA-containing electrolytes shown in Chapter 4, with the exception of high $LiPF_6$ cases that had relatively high deviation from experiment (~8%), the AEM's agreement with experiment is good over all parameters ($LiPF_6$ concentration, temperature, solvent

composition). The overall deviation from experiment for viscosity over all conditions was 5.5%, and similarly the deviation for conductivity was 4.9%.

For the EC-free electrolytes presented in Chapter 5, the AEM's deviation from experiment was slightly higher. For conductivity, the average deviation over all conditions was 11.1%, with considerably higher deviation found at low salt concentrations (18.5% at 0.5 m). For the viscosity measurements, the average deviation of the AEM calculations was 10.2%. When DMC was used as the sole solvent, the AEM's calculations for viscosity showed poor agreement with experiment (25.4% deviation at 2.0 m $LiPF_6$, for example), with the exception of the salt-free system.

While earlier versions of the AEM were able to correctly predict the conductivity and viscosity of the MA-containing electrolytes, most likely due to the overall high permittivity of these solutions, problems were encountered for low-EC electrolytes. In fact, previous versions of the model could not run low-EC electrolytes without crashing. By providing Gering (the developer of the AEM) with high-quality transport data for low-EC electrolytes, the model has been improved and can now support this class of electrolytes. The AEM in its current form showed good agreement with the various electrolyte systems studied in this thesis.

6.1 FUTURE WORK

Due to the immense popularity and longevity of the $LiPF_6$ salt in Li-ion battery electrolytes, the transport properties of electrolytes containing this salt have been thoroughly studied over the years[23,48-58]. Due to the superiority of $LiPF_6$ in commercial

Li-ion cells, it was the main salt considered in this thesis. Comparatively, there is much less peer-reviewed work for electrolyte systems with different conducting salts.

It was mentioned in Chapter 2 that the salt Li bis(fluorosulfonyl)imide (LiFSI) may be able to compete with LiPF$_6$ due to the high mobilities of the ions, high degree of dissociation, thermal stability, and ability to passivate Al unlike its relative Li bis(trifluoromethanesulfonyl)imide (LiTFSI). However, because this salt was developed relatively recently, and it has not seen any widespread adoption yet, transport data for this salt is limited, especially mixed with organic solvents. Conductivity measurements have been presented for "stock" solvent blends such as EC:DMC, and for a few other non-carbonate solvents[124-129]. It would be of interest to map out the transport properties (conductivity, viscosity, etc.) for a wide range of solvent systems and salt concentrations for the LiFSI salt in a similar manner to what was done in this thesis for LiPF$_6$.

Transport data for alternative Li salts would be useful for several purposes. First, from a more fundamental perspective, these measurements shed some light on the association behaviour of the salt. For example, if the LiFSI salt is indeed nearly fully dissociated, plots of κ vs $1/\eta$ should give a straight line for a given salt concentration based on the Stokes' Law derivation for conductivity that was carried out in Chapter 2. Further, researchers concerned with modeling the charge-discharge behaviour of Li-ion cells require this transport data for accurate simulations. For LiPF$_6$ electrolytes this data is readily available. As mentioned above, for other salts such as LiFSI this data is only available for a limited set of solvent systems and salt concentrations. Measuring the transport properties of electrolytes with different salts would be valuable for these physics-based models. This data could also be used to further validate theoretical models

of electrolyte properties such as the AEM. In this thesis, the AEM was validated for a wide range of $LiPF_6$-based electrolytes, but the AEM supports calculations for a number of other Li salts, including LiFSI and LiTFSI. Along this vein, work is ongoing to validate the AEM against a large array of data from the work of Dudley et al.[47], where the primary salt considered was $LiAsF_6$.

Constructing Walden plots from transport property measurements has proven to be an effective way to qualitatively evaluate the degree of salt dissociation in an electrolyte. This technique was originally used to determine the ionicity of ionic liquids[59-65], but has received limited use for non-aqueous electrolytes in recent years[66,67]. Given the simplicity of this analysis technique and the ease in which conductivity and viscosity can be measured for Li electrolytes, Walden analysis should be employed more widely in the screening of potential new electrolyte solutions. For example, for a given solvent composition, creating a Walden plot for various Li salts should show decisively a ranking of the various Li salts' degree of dissociation. This sort of comparison has been done for a limited number of salts in sulfolane by Lee et al.[67]. However, this could be expanded to a wide array of Li salts in various solvents to create a qualitative "rule of thumb" for choosing an electrolyte system for a given application.

Understanding the phase behaviour of Li electrolytes is key for considering performance of batteries in real-life scenarios, such as in electric vehicles or grid-level storage applications. In cold climates, it must be ensured that the liquidus transition of the electrolyte is not reached, or else discharge capacity and rate capability may be compromised. Phase diagrams for various carbonate solvent blends used in Li-ion cells have been constructed by Ding et al. in several works[17,24,85,121,122]. However, very rarely

140

has the phase behaviour of these systems been tested for full electrolytes (i.e. with salt added). In Chapter 5, a preliminary phase diagram was presented for the EC:DMC:LiPF$_6$ system using the DTA technique developed by Day et al.[84]. However, in this study only one concentration of LiPF$_6$ was considered. To gain a complete understanding of the phase diagram for salt-containing systems, many more LiPF$_6$ concentrations must be measured. The physical origin of the additional features that emerged in the 1 m LiPF$_6$ electrolytes (see Figure 5.11) could not be understood given the limited amount of data. Work is currently underway to construct a complete phase diagram for the EC:DMC:LiPF$_6$ system for solvent compositions EC:DMC x:(100-x) for $0 \leq x \leq 50$ (wt. %) and LiPF$_6$ concentrations between 0 and 2 m. The results of this study will be the subject of a forthcoming publication. This will be the first work to fully characterize the phase diagram of a ternary carbonate:carbonate:LiPF$_6$ system in the literature.

Since ionic conductivity in an electrolyte solution is a combination of the mobilities of *all* ions present in an electrolyte (See Equation 2.1), it is not an ideal metric for evaluating an electrolyte solution since only the transport of Li$^+$ is relevant in Li-ion batteries. Another useful metric is the Li$^+$ transference number that was defined in Chapter 2:

$$t_{Li} = \frac{\mu_{Li}}{\sum_i \mu_i} \tag{6.1}$$

where μ_{Li} is the mobility of Li$^+$, and the denominator in Equation 6.1 is the sum of the mobilities of all ions present in solution. The underlying assumption made in comparing conductivity values for different electrolytes is that when the conductivity is increased, at least some of this increase in the overall conductivity comes from the Li$^+$ contribution. While this is often a fair assumption, it may not always be the case if the transference

numbers change significantly from one system to another. The reason that conductivity is often reported instead of transference number or mobility is that the conductivity measurement is much easier to do. As a result, transference numbers are vastly under-reported in the literature for non-aqueous electrolytes.

In addition to providing a more honest picture of Li transport in electrolytes, transport properties of electrolytes beyond conductivity and viscosity (such as transference numbers) are of particular interest for researchers developing physics-based models of Li-ion batteries (or other types of batteries). For these simulations, simple conductivity and viscosity values are not sufficient to completely describe ion transport in electrolytes. These models require advanced properties such as transference numbers, diffusion coefficients, and activity coefficients[54,68,87-89]. The first modern attempt to determine these transport properties for Li electrolytes was done by Valøen and Reimers[54] in 2006. Since then, little advancement has been made in this area, even though the need for these measurements has been expressed in the literature[68].

Very recently, work by Landesfeind et al. and Ehrl et al. has attempted to bring attention to the severe lack of transport parameter data in the literature and develop new methods to obtain these properties[89,130,131]. However, even in these works the data is only presented as a proof-of-concept for their methods. More work must be done to catalog transference number data as well as diffusivity and other transport parameters for a broad range of electrolyte systems. The AEM is also capable of providing calculations for transference number, diffusivity, etc. It would be convenient to use calculations directly from the AEM as inputs for Li-ion simulation software. However, it is first necessary that these values be verified experimentally before they may be trusted.

APPENDIX

A.1 Permissions

Work contained in this thesis contained work published in peer-reviewed journals that were either authored or co-authored by the author of this thesis. The copyright release for AIP journals (Rev. Sci. Instrum.) is given below. Publications in the Journal of the Electrochemical Society are Open Access and are as such covered under a Creative Commons license. Reproductions of Figures from peer-reviewed publications not authored by the author of this thesis is used under the Fair Dealing provisions of the Copyright Act (Section 29).

AIP Publishing

LICENSE TO PUBLISH AGREEMENT FOR JOURNALS

This License to Publish must be signed, either electronically within the Peer X-Press manuscript submission system, or as a PDF to be uploaded into Peer X-Press as an alternate form, before the manuscript can be published. If you have questions about how to submit the form, please contact the journal's editorial office. For questions regarding the copyright terms and conditions of this License, please contact AIP Publishing LLC's Office of Rights and Permissions, 1305 Walt Whitman Road, Suite 300, Melville, NY 11747-4300 USA; Phone 516-576-2268; Email: rights@aip.org.

Article Title ("Work"):

(Please indicate the final title of the Work. Any substantive changes made to the title after acceptance of the Work may require the completion of a new agreement.)

All Author(s):

(Please list **all** the authors' names in order as they will appear in the Work. All listed authors must be fully deserving of authorship and no such authors should be omitted. For large groups of authors, attach a separate list to this form.)

Journal:

Manuscript ID#

All Copyright Owner(s), if not Author(s):

(Please list **all** copyright owner(s) by name. In the case of a Work Made for Hire, the employer(s) or commissioning party(ies) are the copyright owner(s). For large groups of copyright owners, attach a separate list to this form.)

Copyright Ownership and Grant of Rights

For the purposes of this License, the "Work" consists of all content within the article itself and made available as part of the article, including but not limited to the abstract, tables, figures, graphs, images, and multimedia files, as well as any subsequent errata. The Work refers to the content contained in both the Accepted Manuscript (AM) and the Version of Record (VOR). "Supplementary Material" consists of material that is associated with the article but linked to or accessed separately (available electronically only), including but not limited to data sets and any associated files.

This Agreement is an Exclusive License to Publish not a Transfer of Copyright. Copyright to the Work remains with the Author(s) or, in the case of a Work Made for Hire, with the Author(s)' employer(s). AIP Publishing LLC shall own and have the right to register in its name the copyright to the journal issue or any other collective work in which the Work is included. Any rights granted under this License are contingent upon acceptance of the Work for publication by AIP Publishing. If for any reason and at its own discretion AIP Publishing decides not to publish the Work, this License is considered void.

Each Copyright Owner hereby grants to AIP Publishing LLC the following irrevocable rights for the full term of United States and foreign copyrights (including any extensions):

1. The exclusive right and license to publish, reproduce, distribute, transmit, display, store, translate, edit, adapt, and create derivative works from the Work (in whole or in part) throughout the world in all formats and media whether now known or later developed, and the nonexclusive right and license to do the same with the Supplementary Material.
2. The right for AIP Publishing to freely transfer and/or sublicense any or all of the exclusive rights listed in #1 above. Sublicensing includes the right to authorize requests for reuse of the Work by third parties.
3. The right for AIP Publishing to take whatever steps it considers necessary to protect and enforce, at its own expense, the exclusive rights granted herein against third parties.

Author Rights and Permitted Uses

Subject to the rights herein granted to AIP Publishing, each Copyright Owner retains ownership of copyright and all other proprietary rights such as patent rights in the Work.

Each Copyright Owner retains the following nonexclusive rights to use the Work, without obtaining permission from AIP Publishing, in keeping with professional publication ethics, and provided clear credit is given to its first publication in an AIP Publishing journal. Any reuse must include a full credit line acknowledging AIP Publishing's publication and a link to the VOR on AIP Publishing's site.

Each Copyright Owner may:

1. Reprint portions of the Work (excerpts, figures, tables) in future works created by the Author, in keeping with professional publication ethics.
2. Post the Accepted Manuscript (AM) to their personal web page or their employer's web page immediately after acceptance by AIP Publishing.
3. Deposit the AM in an institutional or funder-designated repository immediately after acceptance by AIP Publishing.

4. Use the AM for posting within scientific collaboration networks (SCNs). For a detailed description of our policy on posting to SCNs, please see our Web Posting Guidelines (https://publishing.aip.org/authors/web-posting-guidelines).
5. Reprint the Version of Record (VOR) in print collections written by the Author, or in the Author's thesis or dissertation. It is understood and agreed that the thesis or dissertation may be made available electronically on the university's site or in its repository and that copies may be offered for sale on demand.
6. Reproduce copies of the VOR for courses taught by the Author or offered at the institution where the Author is employed, provided no fee is charged for access to the Work.
7. Use the VOR for internal training and noncommercial business purposes by the Author's employer.
8. Use the VOR in oral presentations made by the Author, such as at conferences, meetings, seminars, etc., provided those receiving copies are informed that they may not further copy or distribute the Work.
9. Distribute the VOR to colleagues for noncommercial scholarly use, provided those receiving copies are informed that they may not further copy or distribute the Work.
10. Post the VOR to their personal web page or their employer's web page 12 months after publication by AIP Publishing.
11. Deposit the VOR in an institutional or funder-designated repository 12 months after publication by AIP Publishing.
12. Update a prior posting with the VOR on a noncommercial server such as arXiv, 12 months after publication by AIP Publishing.

Author Warranties

Each Author and Copyright Owner represents and warrants to AIP Publishing the following:

1. The Work is the original independent creation of each Author and does not infringe any copyright or violate any other right of any third party.
2. The Work has not been previously published and is not being considered for publication elsewhere in any form, except as a preprint on a noncommercial server such as arXiv, or in a thesis or dissertation.
3. Written permission has been obtained for any material used from other sources, and copies of the permission grants have been supplied to AIP Publishing to be included in the manuscript file.
4. All third-party material for which permission has been obtained has been properly credited within the manuscript.
5. In the event that an Author is subject to university open access policies or other institutional restrictions that conflict with any of the rights or provisions of this License, such Author has obtained the necessary waiver from his or her university or institution.

This License must be signed by the Author(s) and, in the case of a Work Made for Hire, also by the Copyright Owners. One Author/Copyright Owner may sign on behalf of all the contributors/owners only if they all have authorized the signing, approved of the License, and agreed to be bound by it. The signing Author and, in the case of a Work Made for Hire, the signing Copyright Owner warrants that he/she/it has full authority to enter into this License and to make the grants this License contains.

1. The Author must please sign here (*except if an Author is a U.S. Government employee, then please sign under #3 below*):

Author Signature   Print Name   Date

2. The Copyright Owner (if different from the Author) must please sign here:

Name of Copyright Owner   Authorized Signature and Title   Date

3. If an Author is a U.S. Government employee, such Author must please sign below. The signing Author certifies that the Work was written as part of his/her official duties and is therefore not eligible for copyright protection in the United States.

Name of U.S. Government Institution (e.g., Naval Research Laboratory, NIST)

Author Signature   Print Name   Date

PLEASE NOTE: NATIONAL LABORATORIES THAT ARE SPONSORED BY U.S. GOVERNMENT AGENCIES BUT ARE INDEPENDENTLY RUN ARE NOT CONSIDERED GOVERNMENT INSTITUTIONS. (For example, Argonne, Brookhaven, Lawrence Livermore, Sandia, and others.) Authors at these types of institutions should sign under #1 or #2 above.

If the Work was authored under a U.S. Government contract, and the U.S. Government wishes to retain for itself and others acting on its behalf, a paid-up, nonexclusive, irrevocable, worldwide license in the Work to reproduce, prepare derivative works from, distribute copies to the public, perform publicly, and display publicly, by or on behalf of the Government, please check the box below and add the relevant Contract numbers.

☐ Contract #(s) _____ [1.16.1]

REFERENCES

[1] G. E. Blomgren, J. Electrochem. Soc. **164**, A5019 (2017).

[2] R. Schmid and C. Pillot, AIP Conference Proceedings **1597**, 3 (2014).

[3] M. S. Whittingham, Chem. Rev. **104**, 4271 (2004).

[4] M. N. Obrovac and V. L. Chevrier, Chem. Rev. **114**, 11444 (2014).

[5] J. R. Dahn, and G. M. Ehrlich, *Lithium-Ion Batteries*, Linden's Handbook of Batteries, 4th ed., Ch. 26, McGraw-Hill Education (2011).

[6] K. Xu, Chem. Rev. **104**, 4303 (2004).

[7] K. Xu, Chem. Rev. **114**, 11503 (2014).

[8] K. L. Gering, Electrochim. Acta **51**, 3125 (2006).

[9] K. L. Gering, L. L. Lee, L. H. Landis, and J. L. Savidge, Fluid Phase Equilibria **48**, 111 (1989).

[10] K. L. Gering, Electrochim. Acta **225**, 175 (2017).

[11] T. Zheng, J. N. Reimers, and J. R. Dahn, Phys. Rev. B **51**, 734 (1995).

[12] C. P. Grey and J. M. Tarascon, Nat. Mater. **16**, 45 (2017).

[13] S. S. Zhang, J. Power Sources **162**, 1379 (2006).

[14] M. Winter, Z. Phys. Chem. **223**, 1395 (2009).

[15] S. J. An, J. Li, C. Daniel, D. Mohanty, S. Nagpure, and D. L. Wood III, Carbon **105**, 52 (2016).

[16] G. V. Zhuang, K. Xu, H. Yang, T. R. Jow, and P. N. Ross, Jr., J. Phys. Chem. B **109**, 17567 (2005).

[17] M. S. Ding, K. Xu, S. Zhang, and T. R. Jow, J. Electrochem. Soc **148**, A299 (2001).

[18] J. Barthel and H. J. Gores, Handbook of Battery Materials. J. O. Besenhard, Ed. Wiley-VCH, New York, 1998, p. 457 – 491.

[19] R. Petibon, J. Xia, L. Ma, M. K. G. Bauer, K. J. Nelson, and J. R. Dahn, J. Electrochem. Soc. **163**, A2571 (2016).

[20] Y. Matsuda and H. Satake, J. Electrochem. Soc. **127**, 877 (1980).

[21] T. Saito, H. Ikeda, Y. Matsuda, and H. Tamura, J. Appl. Electrochem. **6**, 85 (1976).

[22] Y. Matsuda, M. Morita, and K. Kosaka, J. Electrochem. Soc. **130**, 101 (1983).

[23] L. F. Xiao, Y. L. Cao, X. P. Ai, and H. X. Yang, Electrochim. Acta **49**, 4857 (2004).

[24] M. S. Ding, J. Electrochem. Soc. **151**, A731 (2004).

[25] M. C. Smart, B. V. Ratnakumar, L. D. Whitcanack, K. B. Chin, S. Surampudi, H. Croft, D. Tice, and R. Staniewicz, J. Power Sources **119-121**, 349 (2003).

[26] D. Yaakov, Y. Gofer, D. Aurbach, and I. C. Halalay, J. Electrochem. Soc. **157**, A1383 (2010).

[27] M. C. Smart, B. V. Ratnakumar, S. Surampudi, Y. Wang, X. Zhang, S. G. Greenbaum, A. Hightower, C. C. Ahn, and B. Fultz, J. Electrochem. Soc. **146**, 3963 (1999).

[28] J. Xia, R. Petibon, D. Xiong, L. Ma, and J. R. Dahn, J. Power Sources **328**, 124 (2016).

[29] K. Hayashi, Y. Nemoto, S. Tobishima, and Y. Sakurai, Key Eng. Mater. **169-170**, 221 (1999).

[30] M. C. Smart, B. V. Ratnakumar, and S. Surampudi, J. Electrochem. Soc. **149**, A361 (2002).

[31] A. Jänes and E. Lust, Electrochem. Comm. **7**, 510 (2005).

[32] A. Jänes and E. Lust, J. Electroanal. Chem. **588**, 285 (2006).

[33] R. Petibon, J. Harlow, D. B. Le, and J. R. Dahn, Electrochim. Acta **154**, 227 (2015).

[34] R. Petibon, C. P. Aiken, L. Ma, D. Xiong, and J. R. Dahn, Electrochim. Acta **154**, 287 (2015).

[35] M. C. Smart, B. V. Ratnakumar, K. B. Chin, and L. D. Whitcanack, J. Electrochem. Soc. **157**, A1361 (2010).

[36] D. R. Lide, ed., *CRC Handbook of Chemistry and Physics, Internet Version*, CRC Press, Boca Raton, FL (2005).

[37] X. Ma, J. Li, S. L. Glazier, L. Ma, K. L. Gering, and J. R. Dahn, Electrochim. Acta **270**, 215 (2018).

[38] X. Ma, R. S. Arumugam, L. Ma, E. Logan, E. Tonita, J. Xia, R. Petibon, S. Kohn, J. R. Dahn, J. Electrochem. Soc. **164**, A3556 (2017).

[39] S. L. Glazier, J. Li, X. Ma, L. D. Ellis, J. P. Allen, K. L. Gering, and J. R. Dahn, J. Electrochem. Soc. **165**, A867 (2018).

[40] J. Li, H. Li, X. Ma, W. Stone, S. Glazier, E. Logan, E. M. Tonita, K. L. Gering, and J. R. Dahn, J. Electrochem. Soc. **165** (5), A1027 (2018).

[41] G. H. Newman, R. W. Francis, L. H. Gaines, and B. M. L. Rao, J. Electrochem. Soc. **127**, 2025 (1980).

[42] M. Ue and S. Mori, J. Electrochem. Soc. **142**, 2577 (1995).

[43] M. B. Armand and F. E. K. C. E. Moursli, US patent 4542081 (1985).

[44] H.-B. Han, S.-S. Zhou, D.-J. Zhang, S.- W. Feng, L.-F. Li, K. Liu, W.-F. Feng, J. Nie, H. Li, X.-J. Huang, M. Armand, and Z.-B. Zhou, J. Power Sources **196**, 3623 (2011).

[45] L. Ma, S. L. Glazier, R. Petibon, J. Xia, J. M. Peters, Q. Liu, J. Allen, R. N. C. Doig, and J. R. Dahn, J. Electrochem. Soc. **164**, A5008 (2017).

[46] R. A. Robinson, and R. H. Stokes, Electrolyte Solutions, 2nd revised ed., p.73-431, Dover Publications (1959).

[47] J. T. Dudley, D. P. Wilkinson, G. Thomas, R. LeVae, S. Woo, H. Blom, C. Horvath, M. W. Juzkow, B. Denis, P. Juric, P. Aghakian, and J. R. Dahn, J. Power Sources **35**, 59 (1991).

[48] A. Nyman, M. Behm, and G. Lindbergh, Electrochim. Acta **53**, 6356 (2008).

[49] M. S. Ding, J. Chem. Eng. Data. **48**, 519 (2003).

[50] M. S. Ding and T. R. Jow, J. Electrochem. Soc. **150**, A620 (2003).

[51] M. S. Ding and T. R. Jow, J. Electrochem. Soc. **151**, A2007 (2004).

[52] M. S. Ding, J. Chem. Eng. Data. **49**, 1102 (2004).

[53] M. Dahbi, F. Ghamouss, F. Tran-Van, D. Lemordant, and M. Anouti, J. Power Sources **196**, 9743 (2011).

[54] L. O. Valøen and J. N. Reimers, J. Electrochem. Soc. **152**, A882 (2005).

[55] H. G. Schweiger, M. Multerer, M. Schweizer-Berberich, and H. J. Gores, J. Electrochem. Soc. **152**, A577 (2005).

[56] M. S. Ding, K. Xu, S. S. Zhang, K. Amine, G. L. Henriksen, and T. R. Jow, J. Electrochem. Soc. **148**, A1196 (2001).

[57] T. R. Jow, M. S. Ding, K. Xu, S. S. Zhang, J. L. Allen, K. Amine, and G. L. Henriksen, J. Power Sources **119-121**, 343 (2003).

[58] C. H. Yim, J. Tam, H. Soboleski, and Y. Abu-Lebdeh, J. Electrochem. Soc. **164**, A1002 (2017).

[59] C. Schreiner, S. Zugmann, R. Hartl, and H. J. Gores, J. Chem. Eng. Data. **55**, 1784 (2010).

[60] K. Ueno, H. Tokuda, and M. Watanabe, Phys. Chem. Chem. Phys. **12**, 1649 (2010).

[61] M. Yoshizawa, W. Xu, and C. A. Angell, J. Am. Chem. Soc. **125**, 15411 (2003).

[62] W. Xu, E. I. Cooper, and C. A. Angell, J. Phys. Chem. B **107**, 6170 (2003).

[63] K. Ueno, J. Murai, K. Ikeda, S. Tsuzuki, M. Tsuchiya, R. Tatara, T. Mandai, Y. Umebayashi, K. Dokko, and M. Watanabe, J. Phys. Chem. C **120**, 15792 (2016).

[64] D. R. MacFarlane, M. Forsyth, E. I. Izgorodina, A. P. Abbott, G. Annat, and K. Fraser, Phys. Chem. Chem. Phys. **11**, 4962 (2009).

[65] W. Xu and C. A. Angell, Science **302**, 422 (2003).

[66] A. Hofmann, M. Migeot, E. Thißen, M. Schulz, R. Heinzmann, S. Indris, T. Bergfeldt, B. Lei, C. Ziebert, and T. Hanemann, ChemSusChem **8**, 1892 (2015).

[67] S. Lee, K. Ueno, and C. A. Angell, J. Phys. Chem. C **116**, 23915 (2012).

[68] S. Stewart, and J. Newman, J. Electrochem. Soc. **155**, A458 (2008).

[69] B. Maribo-Mogensen, G. M. Kontogeorgis, and K. Thomsen, Ind. Eng. Chem. Res. **51**, 5353 (2012).

[70] O. Bernard, W. Kunz, P. Turq, and L. Blum, J. Phys. Chem. **96**, 3833 (1992).

[71] P. Turq, L. Blum, O. Bernard, and W. Kunz, J. Phys. Chem. **99**, 822 (1995).

[72] E. Waisman, and J. L. Lebowitz, J. Chem. Phys. **52**, 4307 (1970).

[73] Y. Marcus, and G. Hefter, Chem. Rev. **106**, 4585 (2006).

[74] Y. Matsuda, T. Fukushima, H. Hashimoto, and R. Arakawa, J. Electrochem. Soc. **149**, A1045 (2002).

[75] A. Rosenfeld, and A. Kak, *Digital Picture Processing*, Academic Press (1982).

[76] P. Meer, D. Mintz, A. Rosenfeld, and D. Y. Kim, Int. J. Comput. Vision **6**, 59 (1991).

[77] R. J. Schalkoff, *Digital Image Processing and Computer Vision*, John Wiley and Sons, Australia (1989).

[78] L. G. Shapiro, and G. C. Stockman, *Computer Vision*, Prentice Hall (2001).

[79] I. Culjak, D. Abram, T. Pribanic, H. Dzapo, and M. Cifrek, Proceedings of the 35th International Convention MIPRO, 2142 (2012).

[80] G. Bradski, and A. Kaehler, *Learning OpenCV*, O'Reilly Media, Sebastopol (2008).

[81] J. Kestin, M. Sokolov, and W. A. Wakeham, J. Phys. Chem. Ref. Data **7**, 941 (1978).

[82] S. C. McCutcheon, J. L. Martin, T. O. Barnwell, and D. R. Maidment, *Handbook of Hydrology*, Ch. 11.3 McGraw-Hill, New York (1993).

[83] J. Li, A. R. Cameron, H. Li, S. Glazier, D. Xiong, M. Chatzidakis, J. Allen, G. A. Botton, and J. R. Dahn, J. Electrochem. Soc. **164**, A1534 (2017).

[84] R. P. Day, J. Xia, R. Petibon, J. Rucska, H. Wang, A. T. B. Wright, and J. R. Dahn, J. Electrochem. Soc. **162**, A2577 (2015).

[85] M. S. Ding, K. Xu, and T. R. Jow, J. Electrochem. Soc. **147**, 1688 (2000).

[86] J. Barthel, M. Utz, K. Groß, and H. J. Gores, J. Solution Chem. **24**, 1109 (1995).

[87] S. Zugmann, M. Fleischmann, M. Amereller, R. M. Gschwind, H. D. Wiemhöfer, and H. J. Gores, Electrochim. Acta **56**, 3926 (2011).

[88] S. K. Rahimian, S. Rayman, and R. E. White, J. Power Sources **224**, 180 (2013).

[89] J. Landesfeind, A. Ehrl, M. Graf, W. A. Wall, and H. A. Gasteiger, J. Electrochem. Soc. **163**, A1254 (2016).

[90] D. Aurbach, Y. Ein-Eli, B. Markovsky, and A. Zaban, J. Electrochem. Soc. **142**, 2882 (1995).

[91] M. C. Smart, B. V. Ratnakumar, L. D. Whitcanack, K. A. Smith, S. Santee, R. Gitzendanner, and V. Yevoli, ECS Trans. **11**, 99 (2008).

[92] L. Zhou, M. Xu, and B. L. Lucht, J. Appl. Electrochem. **43**, 497 (2013).

[93] S. Herreyre, O. Huchet, S. Barusseau, F. Perton, J. M. Bodet, and Ph. Biensan, J. Power Sources **97-98**, 576 (2001).

[94] S. V. Sazhin, M. Y. Khimchenko, Y. N. Tritenichenko, and H. S. Lim, J. Power Sources **87**, 112 (2000).

[95] M. C. Smart, B. L. Lucht, S. Dalavi, F. C. Krause, and B. V. Ratnakumar, J. Electrochem. Soc. **159**, A739 (2012).

[96] Y.-G. Cho, Y.-S. Kim, D.-G. Sung, M.-S. Seo, and H. K. Song, Energy Environ. Sci. **7**, 1737 (2014).

[97] D. S. Hall et al., *in preparation* (2018).

[98] L.Y. Beaulieu, E. R. Logan, K. L. Gering, and J. R. Dahn, Rev. Sci. Instrum. **88**, 095101 (2017).

[99] Q. Q. Liu, D. J. Xiong, R. Petibon, C. Y. Du, and J. R. Dahn, J. Electrochem. Soc **163**, A3010 (2016).

[100] Q. Q. Liu, R. Petibon, C. Y. Du, and J. R. Dahn, J. Electrochem. Soc. **164**, A1173 (2017).

[101] S. L. Glazier, R. Petibon, J. Xia, and J. R. Dahn, J. Electrochem. Soc. **164**, A567 (2017).

[102] E. Markevich, G. Salitra, and D. Aurbach, ACS Energy Lett. **2**, 1337 (2017).

[103] J. Self, B. M. Wood, N. N. Rajput, and K. A. Persson, J. Phys. Chem. C **122**, 1990 (2018).

[104] D. J. Xiong, T. Hynes, and J. R. Dahn, J. Electrochem. Soc. **164**, A2089 (2017).

[105] A. J. Gmitter, I. Piltz, and G. G. Amatucci, J. Electrochem. Soc. **159**, A370 (2012).

[106] J. Xia, S. L. Glazier, R. Petibon, and J. R. Dahn, J. Electrochem. Soc. **164**, A1239 (2017).

[107] M. C. Smart, J. F. Whitacre, B. V. Ratnakumar, and K. Amine, J. Power Sources **168**, 501 (2007).

[108] J. Wang, Y. Yamada, K. Sodeyama, E. Watanabe, K. Takada, Y. Tateyama, and A. Yamada, Nature Energy **3**, 22 (2018).

[109] Y. Yamada, K. Furukawa, K. Sodeyama, K. Kikuchi, M. Yaegashi, Y. Tateyama, and A. Yamada, J. Am. Chem. Soc. **136**, 5039 (2014).

[110] E. R. Logan, E. M. Tonita, K. L. Gering, J. Li, X. Ma, L. Y. Beaulieu, and J. R. Dahn, J. Electrochem. Soc. **165**, A21 (2018).

[111] J.M.G. Barthel, H. Krienke, and W. Kunz, *Physical Chemistry of Electrolyte Soutions, Modern Aspects*, Steinkopff-Springer, Darmstadt, 1998.

[112] M. Delsignore, H. Farber, and S. Petrucci, J. Phys. Chem. **89**, 4968 (1985).

[113] L. Doucey, M. Revault, A. Lautié, A. Chaussé, and R. Messina, Electrochim. Acta **44**, 2371 (1999).

[114] R. Petibon, L. Madec, D. W. Abarbanel, and J. R. Dahn, J. Power Sources **300**, 419 (2015).

[115] D. Brouillette, D. E. Irish, N. J. Taylor, G. Perron, M. Odziemkowski, and J. E. Desnoyers, Phys. Chem. Chem. Phys. **4**, 6063 (2002).

[116] D. M. Seo, O. Borodin, S.-D. Han, Q. Ly, P. D. Boyle, and W. A. Henderson, J. Electrochem. Soc **159**, A553 (2012).

[117] S.-D. Han, O. Borodin, J. L. Allen, D. M. Seo, D. W. McOwen, S.-H. Yun, and W. A. Henderson, J. Electrochem. Soc **160**, A2100 (2013).

[118] S.-D. Han, O. Borodin, D. M. Seo, Z.-B. Zhou, and W. A. Henderson, J. Electrochem. Soc **161**, A2042 (2014).

[119] W. A. Henderson, F. McKenna, M. A. Kahn, N. R. Brooks, V. G. Young, Jr., and R. French, Chem. Mater. **17**, 2284 (2005).

[120] D. J. Xiong, M. Bauer, L. D. Ellis, T. Hynes, S. Hyatt, D. S. Hall, and J. R. Dahn, J. Electrochem. Soc. **165**, A126 (2018).

[121] M. S. Ding, J. Electrochem. Soc. **149**, A1063 (2002).

[122] M. S. Ding and T. R. Jow, ECS Trans. **16**, 183 (2009).

[123] T. Okumura and T. Horiba, J. Power Sources **301**, 138 (2016).

[124] L. Zhang, L. Chai, L. Zhang, M. Shen, X. Zhang, V. S. Battaglia, T. Stephenson, and H. Zheng, Electrochim. Acta **127**, 39 (2014).

[125] L. Li, S. Zhou, H. Han, H. Li, J. Nie, M. Armand, Z. Zhou, and X. Huang, J. Electrochem. Soc. **158**, A74 (2011).

[126] T. Takekawa, K. Kamiguchi, H. Imai, and M. Hatano, ECS Trans. **64**, 11 (2015).

[127] X. Shangguan, G. Jia, F. Li, Q. Wang, and B. Bai, J. Electrochem. Soc. **163**, A2797 (2016).

[128] S. Uchida and M. Ishikawa, J. Power Sources **359**, 480 (2017).

[129] D. Shanmukaraj, S. Lois, S. Fantini, F. Malbosc, and M. Armand, Chem. Mater. **30**, 246 (2018).

[130] A. Ehrl, J. Landesfeind, W. A. Wall, and H. A. Gasteiger, J. Electrochem. Soc. **164**, A826 (2017).

[131] A. Ehrl, J. Landesfeind, W. A. Wall, and H. A. Gasteiger, J. Electrochem. Soc. **164**, A2716 (2017).